57

FINAL REPORT

ON

PROJECT MIROS-PHASE I

(15 JULY 1964 - 15 JANUARY 1965)

CONTRACT NO. NAS 5-9716

GPO PRICE $

CFSTI PRICE(S) $

Hard copy (HC) # 4,00

Microfiche (MF) 1,00

ff 653 July 65

Prepared by

NORTH AMERICAN AVIATION, INCORPORATED

SPACE & INFORMATION SYSTEMS DIVISION

ELECTRO-OPTICAL LABORATORY

TORRANCE, CALIFORNIA

for

GODDARD SPACE FLIGHT CENTER

GREENBELT, MARYLAND

FINAL REPORT

ON

PROJECT MIROS-PHASE I

(15 JULY 1964 - 15 JANUARY 1965)

CONTRACT NO. NAS 5-9716

Prepared by

NORTH AMERICAN AVIATION, INCORPORATED

SPACE & INFORMATION SYSTEMS DIVISION

ELECTRO-OPTICAL LABORATORY

TORRANCE, CALIFORNIA

for

GODDARD SPACE FLIGHT CENTER

GREENBELT, MARYLAND

SID 65-117

ACCESSION NO. 00540-65

SUMMARY

This report presents the results of Phase I of the MIROS program, Contract No. NAS 5-9716, conducted by North American Aviation, Inc., (NAA), for NASA Goddard Space Flight Center, Greenbelt, Maryland. The work reported on herein was performed at the Electro-Optical Laboratory of NAA's Space and Information Systems Division, located in Torrance, California, during the time period July 15, 1964, to January 15, 1965.

The Modulation Inducing Retrodirective Optical System (MIROS) concept, originated at the NASA Goddard Space Flight Center, is based on introducing information-carrying modulation into a light beam by varying the optical properties of a retrodirective reflector. With this approach, a receiving station directs an unmodulated beam of light at the MIROS transmitting station and receives the retroreflected light. By detecting the modulation resulting from the action of the MIROS reflector, the receiving station acquires the desired information.

The MIROS concept offers a number of unique advantages for space communications. For example, the power requirements of the MIROS retromodulator are only a small fraction of that needed by the laser light source. (In most MIROS communication link applications the laser can be located on the ground or on a larger spacecraft where adequate power is available.) Moreover, the effective area of the retrodirective reflector is insensitive to incidence angle of the laser beam over a wide angular range. Thus, by use of a MIROS communication link, critical requirements on attitude stabilization

and pointing accuracy at the transmitting station can be avoided. Additionally, MIROS retroreflectors can be light-weight, rugged, radiation-resistant, and long lived.

These properties allow the MIROS concept to be considered for a number of applications which may prove to be of value to NASA; the following are examples.

An earth-orbiting MIROS may be useful as a communication satellite. In this application, lasers located at two widely separated ground stations would be pointed simultaneously at the satellite. Modulation applied to the beam at one ground station (the transmitter) would be detected on board the satellite by an optical receiver. The detected signal would be applied to the MIROS retroreflector, causing its reflective properties to vary as a function of the modulating signal. The retroreflected radiation from the second incident beam would thus be modulated. By detecting this modulation at the second ground station (the receiver), information would be transferred from one ground station to the other.

A lunar-orbiting MIROS could be used similarly as a communications satellite for providing over-the-horizon communications between moon-based teams.

A MIROS package carried by a small excursion module or by an individual astronaut may be used to communicate with a larger space station. The small size and weight, low power consumption, and ease of pointing the MIROS package would make its use advantageous aboard a small module or by an individual; the tracking laser required for effecting the communication link would be provided in the larger vehicle.

A MIROS package planted on the moon could be used for telemetering information from scientific measurements. For this application, measurements (e.g., temperature, pressure, seismic phenomena, and meteoric impacts) might be obtained with no electrical power required at the telemeter transmitter. This could be accomplished, for example, by mechanically coupling the sensing transducer directly to the MIROS modulator element.

A MIROS retromodulator may prove to be extremely valuable as a transmitter aboard manned spacecraft during the reentry communications "black out".

The objective of the Phase I effort reported on herein was to perform the preliminary design of a MIROS package. (The final design and fabrication are to be performed in a subsequent phase.) In accordance with the contract requirements, the MIROS package to be designed contains the following components:

An optical retromodulator

A driver amplifier for the retromodulator

A signal converter for matching the characteristics of the electronic signals from various information sources to the input requirements of the retromodulator driver amplifier.

An optical receiver comprising collecting optics, spectral filter, photosensor, a low-noise automatic gain controlled amplifier, and a high voltage power supply (for the photosensor)

The latter three components are straightforward (state-of-the-art); the retromodulator (the key component) required developmental effort.

For implementing the retromodulator several approaches are possible. One general approach is to use telescope optics with a suitably curved mirror at the focal plane (this constitutes a retrodirective optical system). By incorporating a means at the mirror surface to modulate the retrodirected light, either through the use of interference phenomena (e.g., by means of a Fabry-Perot interferometer incorporating piezoelectric modulating elements), or simply by defocusing the retrodirected light by mechanical movement of the mirror surface, the telescope optics can be made into a retromodulator. Another approach is to incorporate a means of modulation into an optical corner reflector; this has the advantage of providing a much wider usable incidence angle.

The latter approach, i.e., modulatable corner reflector, was pursued by NAA. The retromodulator design originally proposed and further developed under the Phase I effort, briefly, is as follows: The required 100 square-centimeter effective area is obtained by providing an array of several corner reflectors. Each corner reflector is constructed of three separate quartz plates bonded together by optical contacting. Two of the inside surfaces of the corner reflector are made reflective by applying an aluminum coating; the modulator elements are located on the third surface of the corner reflector. The modulator elements are circular quartz discs, approximately 2 cm in diameter, having aluminum coated plastic (mylar) membranes stretched across their top surfaces. The discs have shallow depressions beneath the mylar membranes; the membranes are thus supported around the edges as a drum head. Provision is made for applying modulating voltages to the aluminum coatings of the membranes as well as the aluminized surfaces of the depressions in the discs. The membranes are deformed by the applied electrostatic forces, and the resulting deformations cause the collimation of light beams reflected from the membranes to be "spoiled"; i. e., cause modulation of the reflected beamwidth. This results in amplitude modulation of the beam power at a distant receiver.

NAA's plan for conducting Phase I of the MIROS program incorporated eight separate tasks. These tasks, together with brief summaries of the accomplishments planned as the result of each, are presented in Table I herein. For comparison, brief summaries of the accomplishments actually achieved in each task also are presented in Table I, presented on page 8 at the end of this summary. (These accomplishments, as well as all aspects of the contracted program, are discussed in detail in the following sections of this report).

The actual accomplishments achieved under the Phase I effort reflect the effects of the discovery, definition, and partial investigation of two critical factors, viz: (1) membrane materials problems which tended to limit the beamwidth and reflectivity of the MIROS modulator models which were fabricated and tested, and (2) a "breakthrough" in modulator design which allows achievement of greatly increased bandwidth of the device. These technical problems and the bandwidth "breakthrough" will now be listed and summarized briefly.

(1) Retromodulator reflected beamwidth. During the Phase I program

a an investigation of plastic membrane materials was conducted in order to obtain materials of adequate quality for constructing the MIROS retromodulator. Although more effort was applied to this than originally planned, sufficiently flat mylar was not obtained within the time available. As a consequence, the retromodulator models which were constructed were not diffraction limited and the reflected beamwidths were approximately ± 25 arc-seconds rather than ± 10 arc-seconds.

(2) Reflectivity. The mylar materials obtained during the Phase I effort exhibited microscopic surface roughness as well as the larger scaled waviness alluded to above. When the mylar material is aluminized, the coated surface exhibits the same surface roughness. The results is inferior reflecting surfaces for the modulator units in comparison with polished and coated quartz or similar optical material. The reflectivity of the coated membranes may be only 25 to 30 percent of that of a good first surface mirror. Without further improvement, these two effects - increased beamwidth and decreased reflectivity - would result in the reduction of the range of MIROS to about 60% of that desired for a retromodulator of any given area. (This figure includes the effect of an offsetting increase in the depth of modulation of 80% which can be obtained rather than the goal of 50%.)

(3) Bandwidth. In the course of the experimental investigation a "break-through" with respect to bandwidth was achieved. It was discovered that a significant increase (by a factor of 5 or more) in the first resonant frequency of the membrane could be obtained by operating the modulators under slight pressurization rather than in vacuum as had

been planned. Further theoretical and experimental effort was then applied to investigating the performance of pressurized modulators. These investigations, however, because of schedule and funding restraints, were not adequate to provide a comprehensive understanding of the ultimate performance which might be achieved by selecting a set of optimum parameters (i. e., gas pressure, bias voltage, driving power, and depth of modulation.) The characteristics of the optimum retromodulator design, therefore, are unknown at the present time. If it were necessary to begin the fabrication of a MIROS package immediately, Table II presents the retromodulator performance which could be attained with high confidence.

Because of the information and knowledge gained as a result of the Phase I efforts, it is evident that improvements in the performance of the MIROS retromodulator over that presented in Table II can be achieved by additional effort in selected areas. It is recommended that effort be continued in these areas to provide an improved final design with a higher confidence level prior to actual fabrication and evaluation of the complete MIROS package. The recommended additional effort is summarized in Table III.

TABLE I

MIROS - PHASE I

NAA's Phase I Program Plan (Including Increase of Scope - Reference Supp. Agreement Eff. 10-20-64)

	Tasks	Planned Accomplishments	Actual Accomplishments
I.	Fabrication of Laboratory Test Modulators	Fabricate 3 piston-type (test bed) and 4 disc-type (actual design configuration) modulators	3 piston-type modulators fabricated. Disc-type modulator parts fabricated but not assembled (2 are 90% complete).
II.	Evaluation of Laboratory Test Modulators	Fabricate and assemble test equipment; test and evaluate the modulator models (dynamic tests in vacuum)	Test equipment fabricated and assembled; piston-type modulators evaluated in vacuum; significant bandwidth increase achievable by pressurizing modulators demonstrated; performance of pressurized modulators investigated; membrane characteristics investigated.
III.	Design of retromodulator	Establish retromodulator configuration	Corner reflector configuration established. Generalized analysis of optical corner reflectors by use of computer ray tracing program resulted in configuration optimization.
IV.	Preliminary Design of Optical Receiver	Perform preliminary design in sufficient detail to permit identification of long lead-time components	Completed as planned
V.	MIROS Packaging Design	Preliminary packaging layouts	Completed as planned
VI.	Preparation of Design Report	Design report	Completed as planned, including recommendations for necessary additional research (in place of final detailed retromodulator design)
VII.	Project Coordination and Direction	Project coordination and direction	Performed as planned

TABLE I (Continued)

MTROS - PHASE I

Tasks	Planned Accomplishments	Actual Accomplishments
VIII. Retromodulator Performance Study	Theoretically study performance, particularly to determine feasibility of operating above first resonant frequency to obtain greater bandwidth	Theoretically studied (1) performance of pressurized modulator for extending bandwidth and (2) far field modulation characteristics

TABLE II

MIROS RETROMODULATOR
PRESENTLY ACHIEVABLE PERFORMANCE VS. DESIGN GOALS

	Goal	Performance which can be attained (Present state-of-the-art)
Bandwidth	20,000 cps	4,000 cps (without pressurization)
		15,000 cps (with pressurization)
Beamwidth	± 10 sec	± 25 sec
Depth of Modulation	50%	80%
Power	Order of one watt	0.1 watt (for 4 KCPS)
Optical Efficiency	Not specified	25%

TABLE III - RECOMMENDED ADDITIONAL EFFORT

1. Investigate membrane materials and fabrication techniques. The objective of this effort is to improve the MIROS retromodulator beamwidth and reflectivity by attaining membranes having adequate flatness and surface quality characteristics.

2. Continue analysis, development and test of membrane units to secure the desired characteristics (i.e., ± 10 sec beamwidth, 20 Kc/s bandwidth, improved reflectivity).

3. Perform a Comparative Analysis of the following options for implementing the MIROS retromodulator:

   (1) Performance of plastic film versus piezoelectric modulators;

   (2) Performance of interferometer versus beam spread modulators

   (3) Performance of corner reflector versus telescope retroreflective optics. In addition, perform a MIROS communication system performance analysis.

4. Complete the design of the MIROS retromodulator and final design of the remainder of the MIROS package.

5. Construct one MIROS corner reflector, without modulator units, for evaluation during Phase I. Test and evaluate the optical and mechanical properties of the unit and deliver to NASA.

TABLE OF CONTENTS

TABLE OF CONTENTS

LIST OF ILLUSTRATIONS

LIST OF ILLUSTRATIONS

LIST OF ILLUSTRATIONS

LIST OF TABLES

SECTION 1

DESIGN

OPTICAL DESIGN OF THE CORNER CUBE REFLECTOR

In Appendix I, the basic relationships for the design of a corner cube reflector are given for the condition that the incoming radiation is travelling parallel to the "optical axis" of the reflector. For this on-axis condition, the exit aperture is an image of the entrance aperture produced by inversion and reversion. Therefore, the optimum entrance aperture will be a regular hexagon, as shown in the Figure II-2 to II-5 in Appendix II.

Appendix II gives the basic equations used for tracing any ray of light through the corner cube reflector for any off-axis condition, within the limitation that an entering ray will not make an angle with the optical axis greater than the angle between the reflecting face and the optical axis.

As the optical axis is tipped away from the incoming radiation, the entrance aperture decreases by the cosine of the angle. Unfortunately, this simple relationship is complicated by the fact that all the radiation entering this decreased aperture will not be reflected back to the source. For example, radiation reflected from the bottom edge of the modulating surface, in Figure II-5 in Appendix II, would be reflected back to the source only if the third surface was made twice as big as shown. Thus, instead of the return beam intensity being decreased to 94% (i.e., 100. cos. 20°), the intensity is decreased to 56% of the on-axis condition.

It can be seen from Figure II-2 that increasing the modulating area would increase the amount of returned beam. However, in Figure II-5, an increase in the modulating area would not produce a corresponding increase in intensity. In Figure II-5, the upper two faces would have to be increased. Thus, for random orientation of the incoming radiation, all three faces would have to be increased to produce a prescribed effective aperture.

Figure 1 shows an array of three symmetrical corner reflectors. As can be seen, the symmetrical hexagon shape of the entrance aperture produces gaps along the outside modulating edges because it is impossible to pack efficiently the required number of discs. A slight change in this face will permit a more efficient packing of the discs and will decrease the nonmodulating areas on this face. Figure 2 illustrates possible arrays of modulating discs and the resulting modulating surface. These arrays are obviously nested more efficiently than those nesting in the surface of the regular hexagon corner reflector. This modification of the modulating reflecting face together with an increase in the other two reflecting faces produces a corner cube reflector of the design shown in Figure 3. Figure 4 illustrates a 9% increase in efficiency using an unsymmetrical aperture when compared to a symmetrical aperture, Figure II-5. There are, however, certain restrictions on the changes to improve the off-axis efficiency.

For proper nesting of three corner cube reflector assemblies, the angle between face edges BC and IJ must be 60°, see Figure 5. Also for proper nesting, the length of edges BC and IJ must be equal to edge length BJ. If three identical corner cube reflectors are nested together in an array as shown in Figure 3, the three modulating faces are each oriented ± 120° from the other two modulating faces. For radiation entering the triple assembly at 20° below the x-axis, i.e., cos $\gamma_o = 0$, the patterns on the entrance apertures given by Figure II-2 and II-4 will be obtained. The third pattern on the third assembly will be a mirror image from left to right of Figure II-4. In any off-axis condition with this array, at least one of the three modulating arrays will be more or less fully utilized. The cost of producing the modulating discs is high in comparison to the cost of enlarging the nonmodulating reflecting surfaces. With this array, it is possible to increase the overall effective area of the array by increasing each pair of reflecting surfaces without increasing the modulating disc array. In fact, it is possible to increase the overall aperture and to decrease simultaneously the area of the modulating array with the disc size as a restriction.

In the calculation of effective aperture size, as is given below, the diameter of the modulating disc is kept at two centimeters.

The array as shown in Figure 3 would have an on-axis aperture of 236 square centimeters and a 20° "off-axis" aperture of 143 square centimeters.

A symmetrical shape of the figures as shown in Appendix II would have an effective aperture of 112.5 square centimeters at 20° off-axis, and 204.5 square centimeters on-axis. However, packing efficiency is not optimum and the overall efficiency will lower these figures. The off-axis aperture would be below the required 100 square centimeters.

The single assembly as shown in Figure 5 will have an effective aperture over 128 square centimeters 20° off-axis, and 233 square centimeters on-axis. This configuration, while slightly unsymmetrical for on-axis use, is very efficient for use with off-axis illumination because of efficient packing and use of the minimum number of modulating discs.

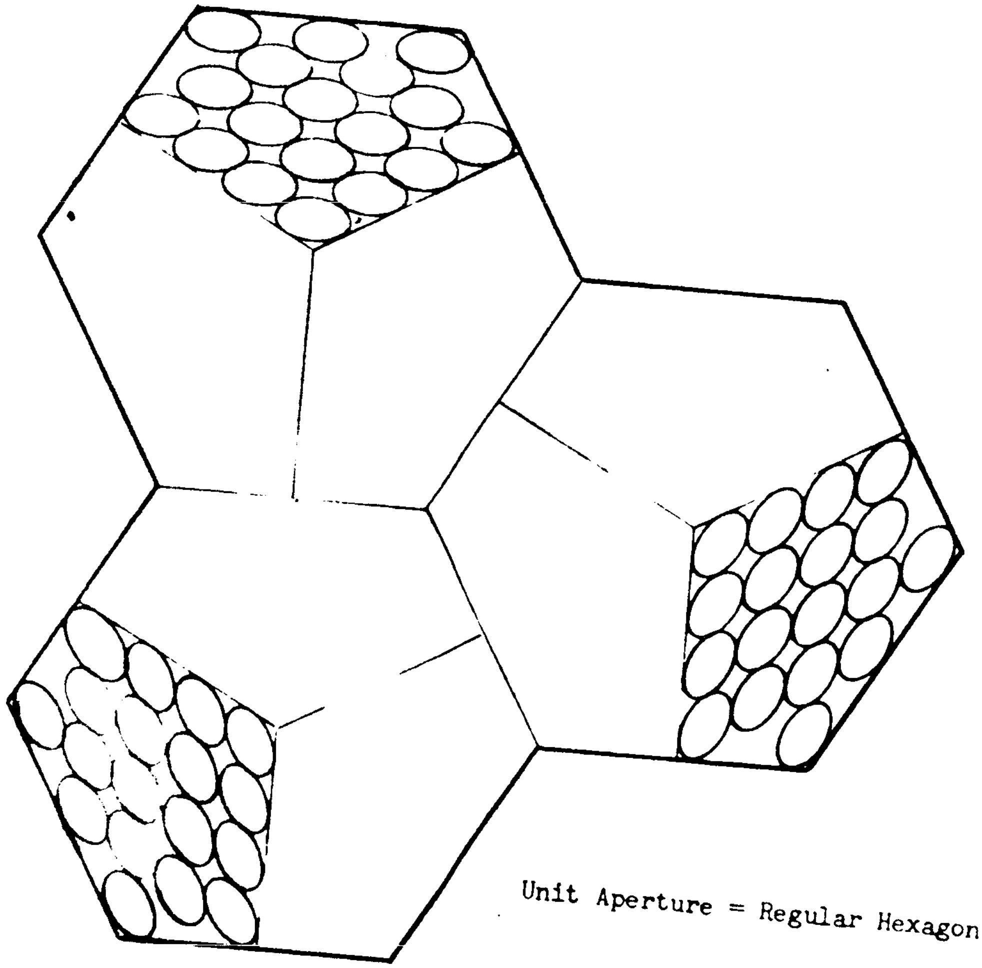

ARRAY OF THREE SYMMETRICAL
CORNER REFLECTOR UNITS

FIGURE 1

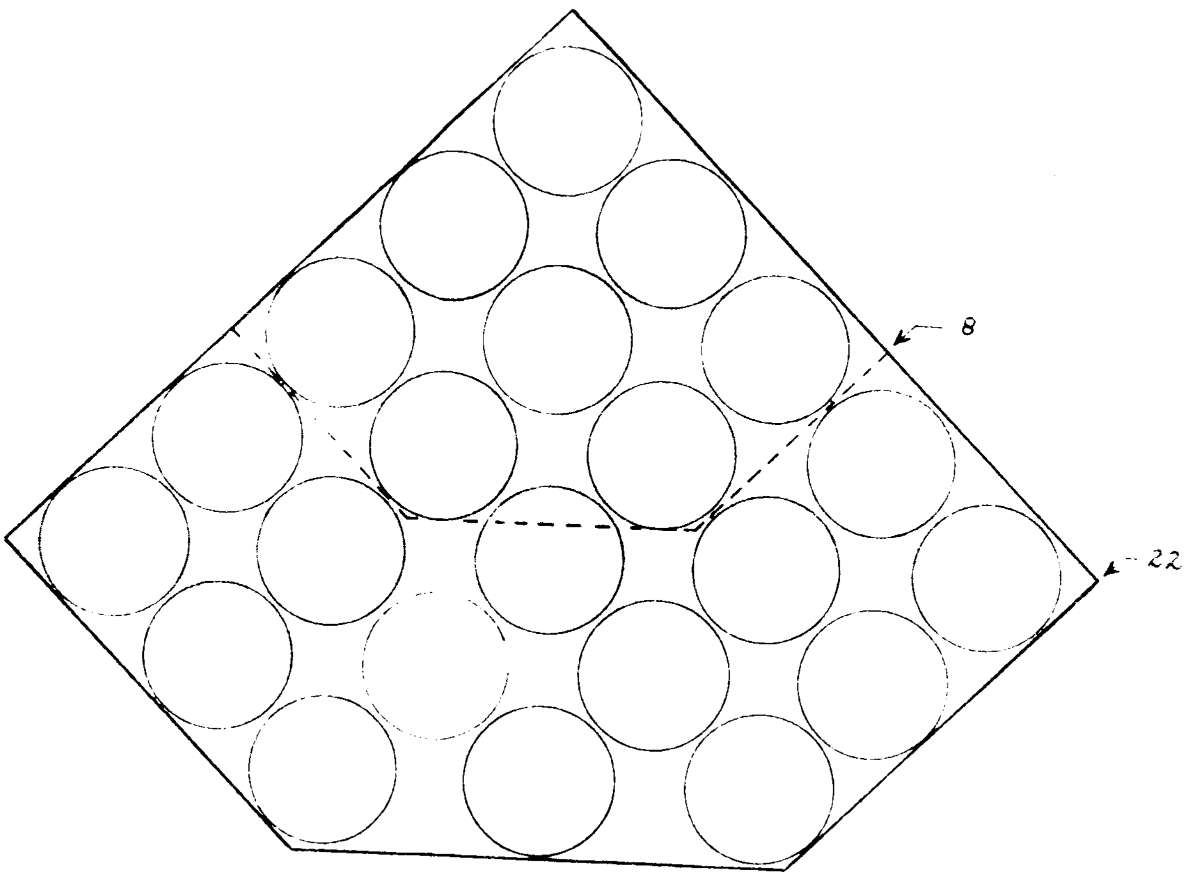

MODIFIED MODULATING SURFACE

FOR

IMPROVED PACKING DENSITY

FIGURE 2

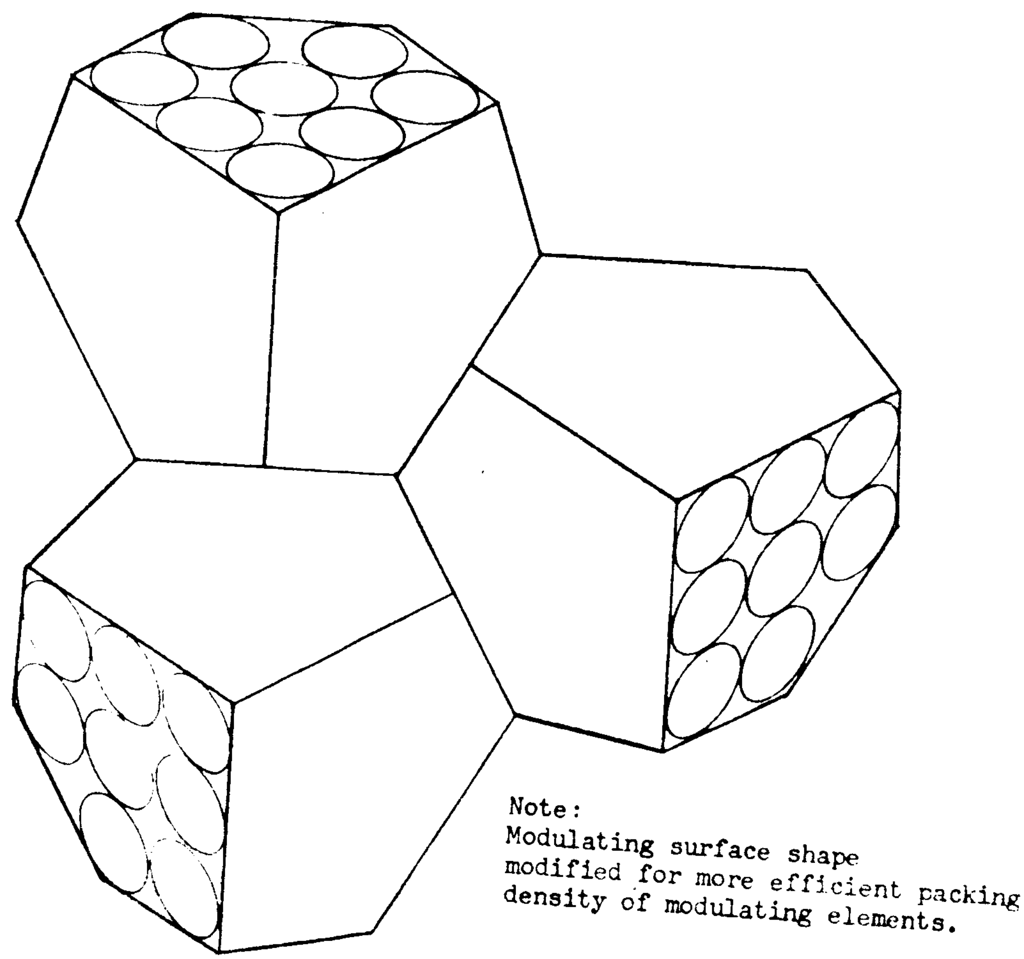

MODIFIED THREE-UNIT CORNER REFLECTOR ARRAY

FIGURE 3

UNSYMMETRICAL APERTURE CORNER REFLECTOR

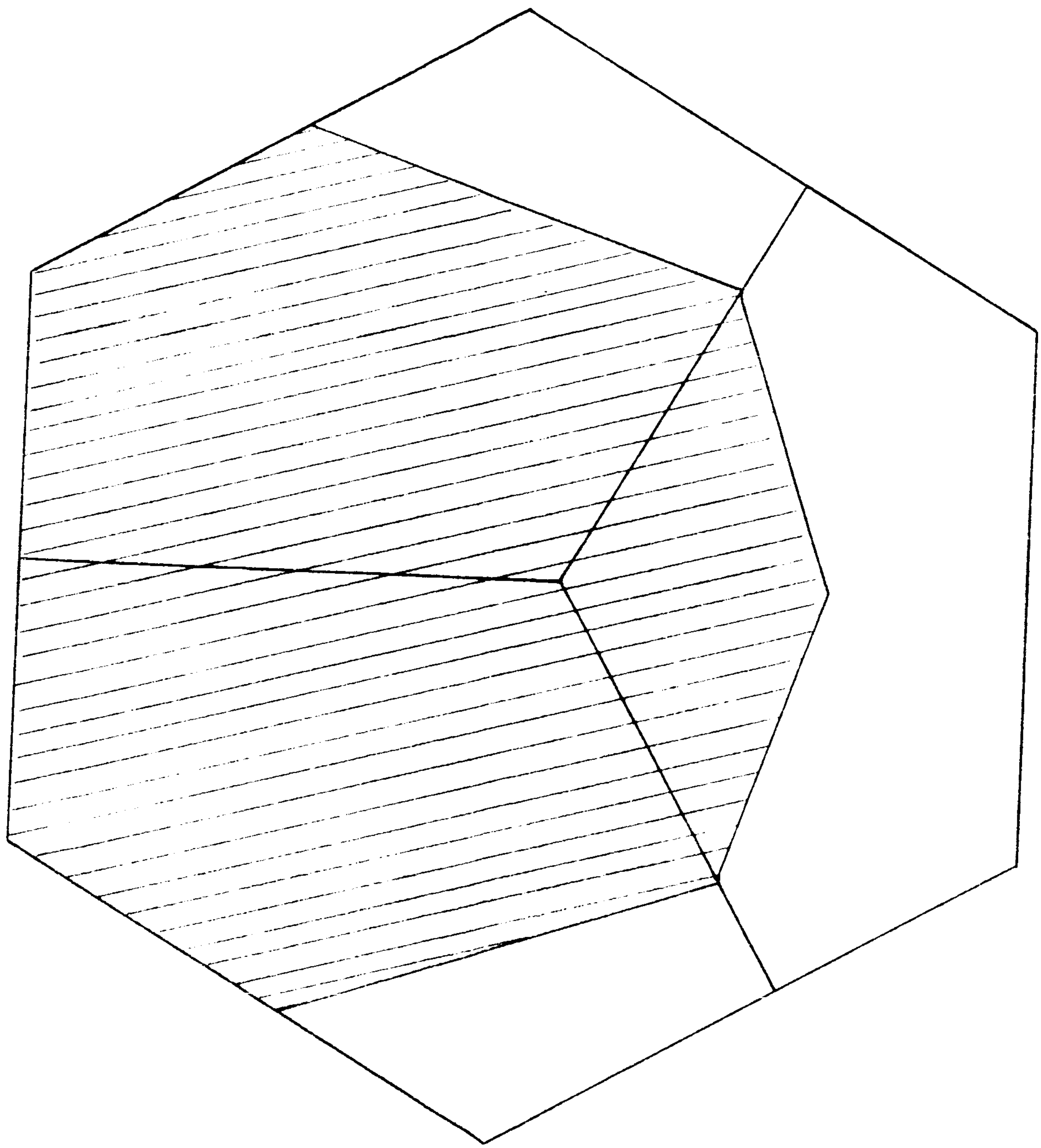

FIGURE 4

AREA UTILIZED FOR $\alpha_o = 20°, \beta_o = -70°, \gamma_o = 90°$ ($\Delta = 180°$)

WITH ENLARGED REFLECTING PLANES

EFFICIENCY = 65%
MODULATING AREA USED = 31.2%

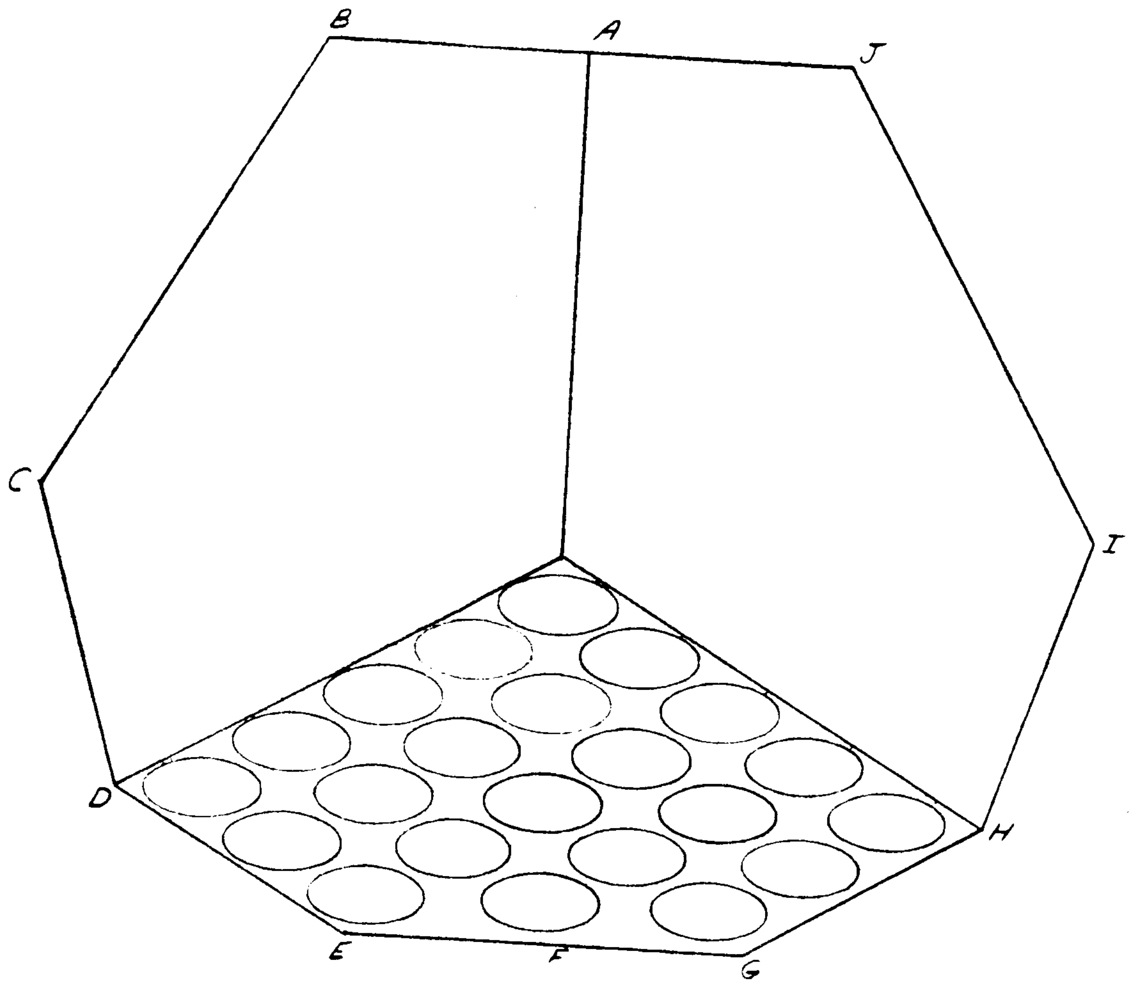

ENTRANCE APERTURE SHAPE, COMPENSATED

FOR

OPTIMUM CONDITIONS AT 20° OFF-AXIS

FIGURE 5

MEMBRANE MATERIALS SURVEY

The purpose of this survey was to compute the first resonance (bandwidth) and required driving voltage for some materials which might be useful as membrane modulators and to compare them to Mylar. For this comparison, results have been normalized to Mylar.

BANDWIDTH (F)

The resonant frequency (F) of a thin membrane under tension is given by:

$$F = \frac{2.40}{\pi D} \left(\frac{\sigma T_m}{\rho} \right)^{\frac{1}{2}}$$

where

D = Diameter of membrane (meters)

σ = Stress/elastic strength limit

T_m = Elastic limit (newtons/m^2)

ρ = Density of membrane material (kg/m^3)

$$F = \frac{2.40}{\pi D} \sqrt{\frac{T\ MAX}{\rho}}$$

$$F = K_1 \sqrt{\frac{T\ MAX}{\rho}}$$

Values of F for various materials, normalized to Mylar - 100, appear in Table 1 and are graphed in Table 2 to indicate the relative bandwidths achievable with different materials.

DRIVING VOLTAGE V:

Rearranging formula (V), Electrostatic Modulator Unit Section, yields:

$$V = \frac{2d}{a} \sqrt{\frac{2t\alpha T_m}{E_o}} \qquad \text{(Va.)}$$

where V = driving voltage required

d = membrane electrode spacing (meters)

Δ = sagitta of deformed membrane (meters)

E_o = 8.85×10^{-12} Farad/meter

a = $D/2$ = radius of membrane (meters)

t = thickness of membrane (meters)

Holding constant α , a, Δ , t, and d, there results the computational formula:

$$V = K_2 \sqrt{T_m}$$

The relationship between required driving voltage and bandwidth can be shown by recalling that

$$F = K_1 \sqrt{\frac{T_m}{\rho}}$$

or

$$\sqrt{T_m} = \frac{F\sqrt{\rho}}{K_1} = \frac{V}{K_2}$$

$$V = K_3 \; F$$

considering all direct variables constant except the membrane stress level. Values of K_3 normalized to mylar = 100 appear in Table 1 and are graphed in Table 3 as an indication of the relative driving voltage requirements of different membrane materials.

TABLE 1

PROPERTIES OF MATERIALS

MATERIAL	$KG/M^3 \times 10^2$*	Tm $NT/M^2 \times 10^6$*	K_3 Mylar = 100	F Mylar = 100
MYLAR	14	140	100.	100
CELLULOSE ACETATE-BUTYRATE	12	34.5	092.	51.7
NYLON	11	69.0	089.	79
POLYETHYLENE	9.5	27.6	082.	54
POLYVINYL CHLORIDE, UNMODIFIED	14	51.7	100.	61
SARAN	17	241	110.	120
ALUMINUM	27	138	139.	71
BRASS	84	276	246.	57
COPPER	89	469	252.	73
GOLD	190	138	369.	27
BERYLLIUM	18.5	414	115.	149
MAGNESIUM	17	228	349.	118
NICKEL	87	1069	250.	112
PALLADIUM	122	269	308.	47
PLATINUM	214	166	392.	28
SILVER	100	290	268.	54
TANTALUM	170	897	349.	73
TIN	73	31	228.	20
TUNGSTEN	190	4069	368.	146
ZINC	72	172	227.	49

* From the "Handbook of Chemistry and Physics," 39th edition, 1957-1958. Chemical Rubber Publishing Company, Cleveland, Ohio.

** Baumeister, Theodore, Mechanical Engineer's Handbook, Sixth Edition. McGraw-Hill Book Company, Inc. 1958.

*** Sigmund Cohn Corp. of America, Products Summary.

Table 2

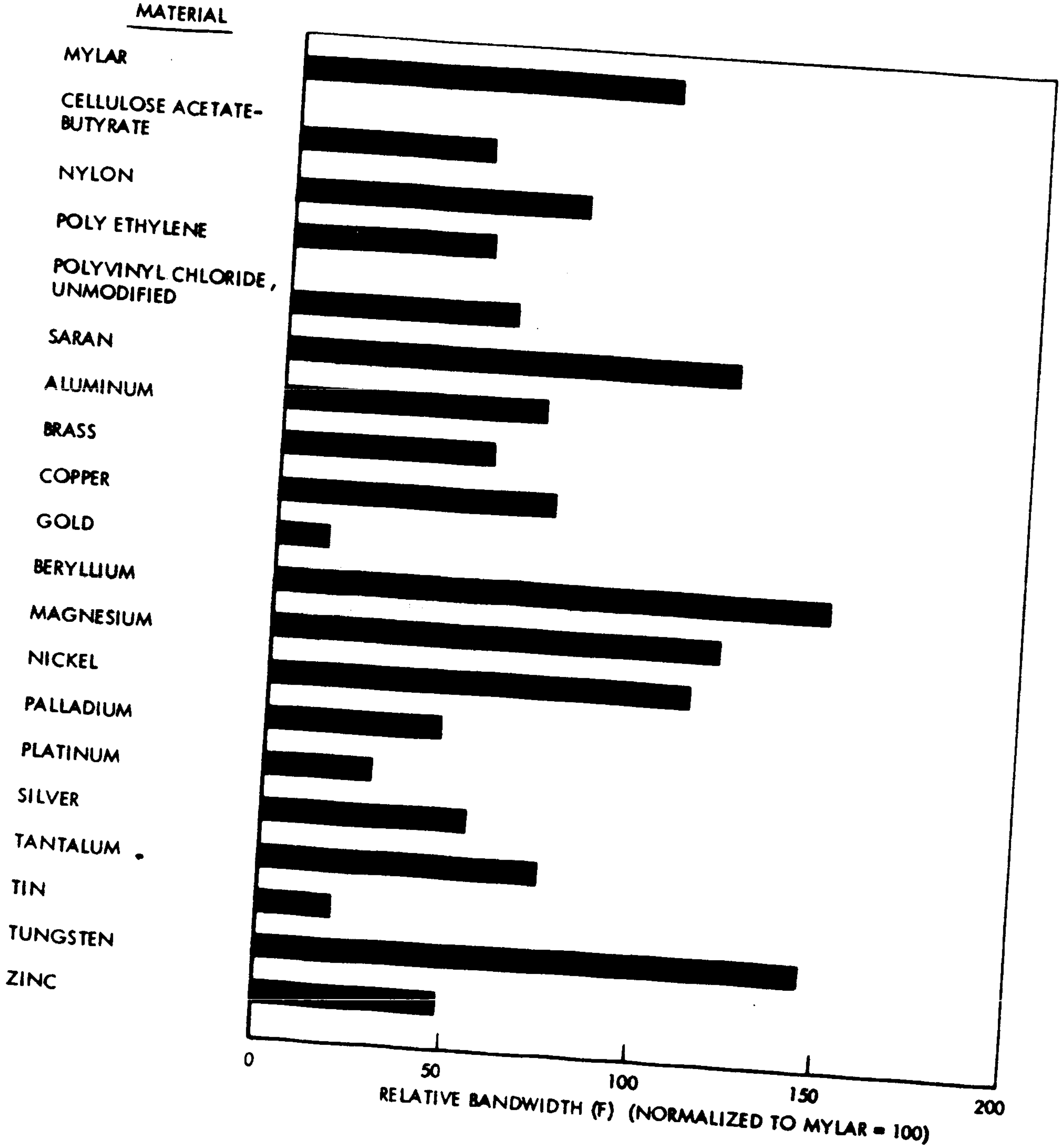
MATERIAL
MYLAR
CELLULOSE ACETATE-BUTYRATE
NYLON
POLY ETHYLENE
POLYVINYL CHLORIDE, UNMODIFIED
SARAN
ALUMINUM
BRASS
COPPER
GOLD
BERYLLIUM
MAGNESIUM
NICKEL
PALLADIUM
PLATINUM
SILVER
TANTALUM
TIN
TUNGSTEN
ZINC
0
50
100
150
200
RELATIVE BANDWIDTH (F) (NORMALIZED TO MYLAR = 100)

Table 3

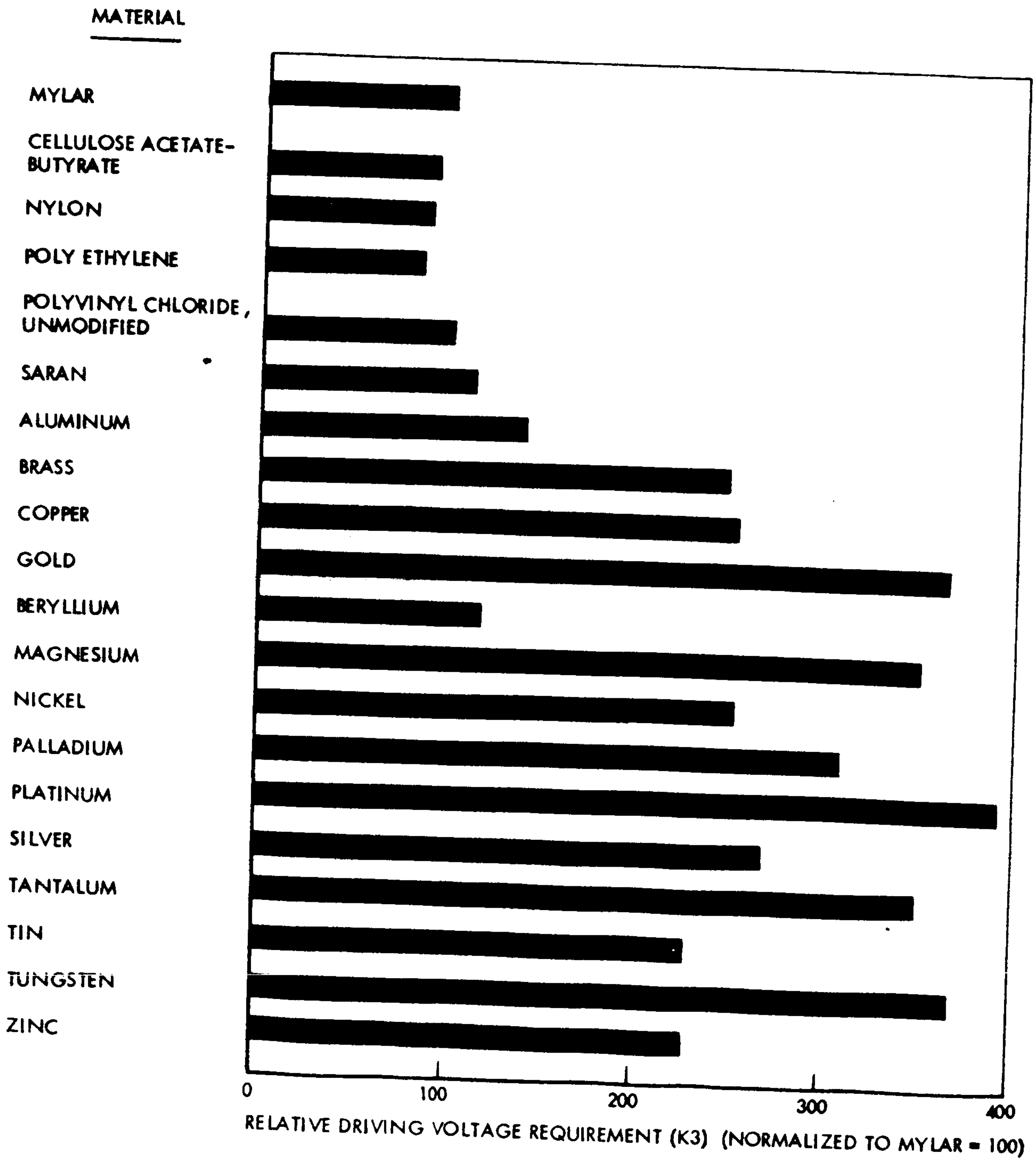
MATERIAL
MYLAR
CELLULOSE ACETATE-BUTYRATE
NYLON
POLY ETHYLENE
POLYVINYL CHLORIDE, UNMODIFIED
SARAN
ALUMINUM
BRASS
COPPER
GOLD
BERYLLIUM
MAGNESIUM
NICKEL
PALLADIUM
PLATINUM
SILVER
TANTALUM
TIN
TUNGSTEN
ZINC
0
100
200
300
400
RELATIVE DRIVING VOLTAGE REQUIREMENT (K3) (NORMALIZED TO MYLAR = 100)

ELECTROSTATIC MODULATOR UNIT

Introduction:

Modulation of the retroreflected beam from a cube corner reflector can be achieved by varying the radius of curvature of any of the three surfaces and thus varying the angular beam spread. The approach selected is to construct one surface of the cube corner reflector as a thin reflective membrane and to change its curvature by application of an electrostatic force created by the electric field between the membrane and a closely-spaced backing surface. Modulation of the electric field is achieved by varying the potential difference between the two surfaces as a function of time.

Design Approach:

The performance goals most significant to the design of the modulatable surface are:

(1) 20 KCPS minimum information bandwidth

(2) 10 arc seconds half-angle spread of the retroreflected beam (modulating membranes undeflected).

(3) Capability for achieving a minimum intensity modulation of 50% in the far field.

(4) Absolute minimal power consumption for modulation of the retroreflector. (On the order of 1 watt.)

(5) Effective reflecting area of $100 CM^2$ within a 20 degree half-angle cone about the retroreflector array axis of symmetry.

For simplicity of both analysis and fabrication only circular membranes are considered.

The bandwidth of this device is defined for use herein as extending from zero frequency to the fundamental (lowest order) resonance of the membrane. The bandwidth is thus numerically equal to the fundamental resonant frequency when expressed in cycles per second. This is the most readily utilized bandwidth although it has been demonstrated that similar devices fabricated at NAA exhibit a usable response above this frequency.[1]

The fundamental resonant frequency (f_o) of a thin membrane under tension is given by:

$$f_o = \frac{2.40}{\pi D} \sqrt{\frac{\alpha T_m}{\rho}} \qquad (I)$$

Where: D = Diameter, M.

T_m = Yield Point Tension, Newton/M^2

ρ = Density, Kg/M^3

α = Ratio of tension applied to yield point tension

Additional conditions that apply to equation (I) are:

(1) Deflections are small enough that the tension is not significantly changed.

(2) The membrane is not loaded.

(3) Tension everywhere in the membrane is uniform.

In order to utilize the small membrane diameters consistent with maximum bandwidth and still provide the required reflecting area, the modulating surface is made up of multiple membranes closely packed and driven in parallel.

---

1 Acoustically-driven membranes with fundamental resonant frequencies of the order of 200 CPS are used in retromodulation systems fabricated by N.A.A. These systems deliver communications quality audio when used as voice channels.

The bandwidth and the diffraction limited beam spread of a single circular membrane are both inversely proportional to the membrane diameter and thus for a given tension in the membrane must be "traded off." The method used for determining the diffraction beam spread is given in Appendix III.

Another parameter related to the membrane diameter is the ratio of modulated area to total area of a practical single membrane modulator unit. This is defined for use herein as the Unit Modulation Efficiency. A plot of this relationship is shown in Figure 6. The fabrication of a practical unit imposes the following requirements:

(1) The membrane must be edge-supported.

(2) The supporting surface must be optically flat to a tolerance consistent with the allowable geometric beam spread.

(3) An area must be provided outside the reference optically flat surface for attaching the membrane. These requirements are fulfilled by having an annular ring around the modulating area diameters of 2 CM or less. Unit Modulation Efficiency is thus proportional to membrane diameter.

From Equation (I), bandwidth of the electrostatically driven membrane is also proportional to the square root of the tension in the membrane. For a given membrane material and diameter operated in vacuum to meet the loading condition on Equation (I), the maximum bandwidth is thus determined by the percent of yield point tension that can be safely maintained. In plastics such as Mylar, the yield strength is a strong function of temperature, decreasing with increasing temperature. (See Figure 7.) For a practical Mylar membrane, a stress of 30% of the elastic limit at 25°C (4800 lb/in^2) allows operation to approximately 125°C.

Depth of Modulation and Required Driving Voltage

The useful depth of modulation is determined by the modulation transfer function which is derived and plotted in Section 2. The measured transfer function for an actual device of this type is shown in Section 4.

The percent depth of modulation is defined for use herein as:

$$M = \frac{I_{max} - I_o}{I_o} (100) \qquad (\text{II})$$

Where: I_{max} = Maximum Intensity when modulated

I_o = Unmodulated Intensity at the selected operating point on the modulation transfer function.

Both the derived and measured modulation transfer functions show the device to be a good approximation to a linear operator at depths of modulation from zero to greater than 50% when operated about the proper bias point.

Although driving voltage and percent modulation are directly related, this relationship is modified by the dependency of the percent modulation for a given membrane deflection on the flatness of the undeflected membrane. The membrane deflection is related to applied voltage as follows:

In a spherically deformed membrane, the sagitta is related to the radius of curvature by

$$\Delta = \frac{a^2}{2R}$$

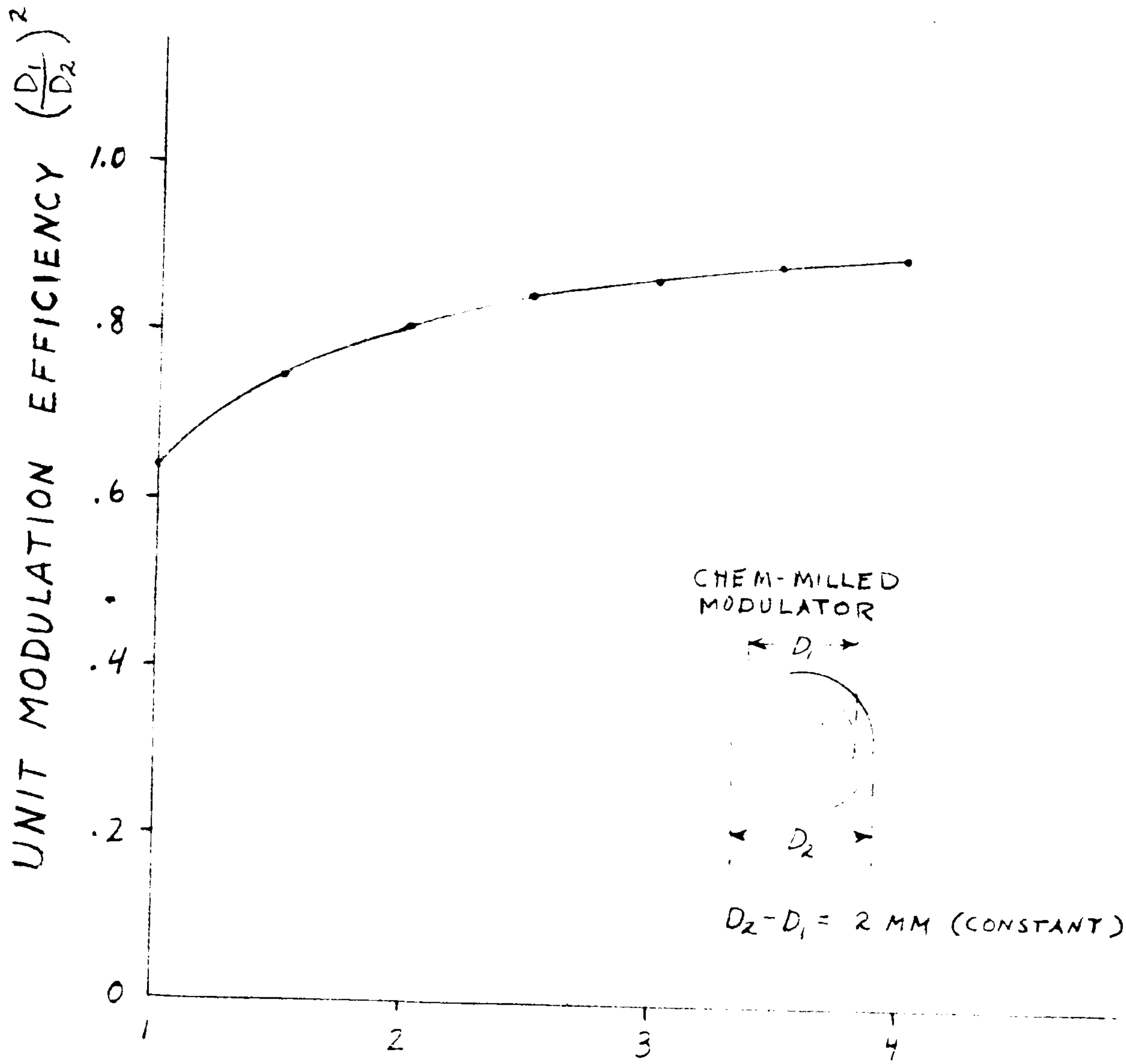

MEMBRANE ACTIVE DIAMETER (D_1)

(CM)

FIGURE 6

MYLAR TENSILE PROPERTIES *

Graph 1
TENSILE FORCE

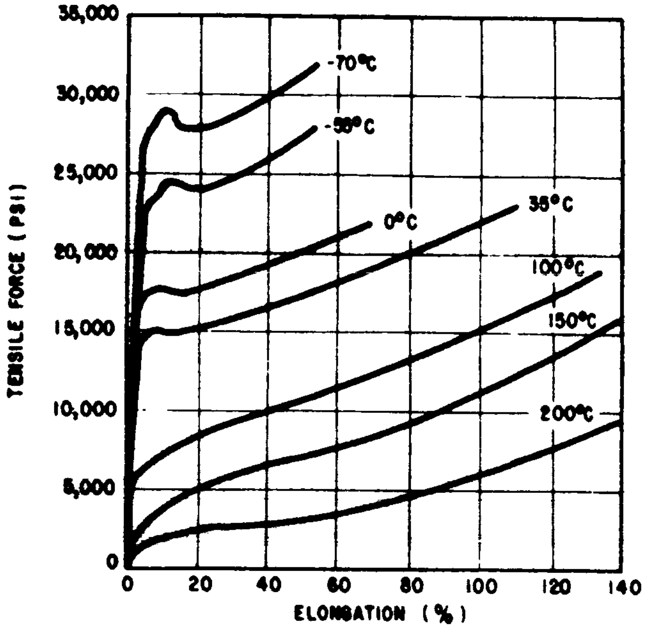

Graph 1 shows typical stress-strain curves for "Mylar"* polyester film at various temperatures.

Graph2 shows how tensile properties vary with temperature. "Mylar" retains its useful physical properties from −60°C. to +150°C. and for some intermittent applications of short duration, it can be used at even higher temperatures.

Graph 2
TENSILE PROPERTIES VS. TEMPERATURE

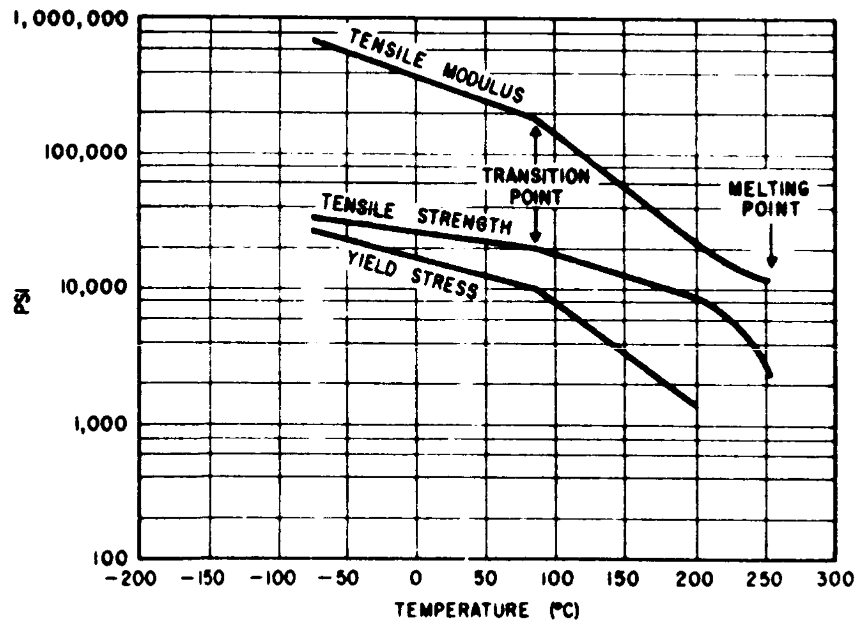

Du Pont registered trademark

* From Dupont Bulletin M-2B

Figure 7

where Δ = deformed membrane sagitta, m

a = membrane radius, m

R = deformed membrane radius of curvature, m

The pressure required to deform the membrane is

$$P = \frac{2N}{R} = \frac{4t\alpha T_m \Delta}{a^2} \qquad \text{(III)}$$

where: P = equivalent pressured required to deform membrane, Newton/m^2.

N = membrane tension, Newton/m.

t = membrane thickness, m.

α = ratio of tension applied to yield point tension.

T_m = yield point tension of the membrane material, Newton/m^2

The pressure applied by the electric field is

$$P = \frac{E_o}{2}\left(\frac{V}{d}\right)^2 \qquad \text{(IV)}$$

where: E_o = dielectric constant of free space, farad/m

V = applied potential difference, volts.

d = spacing between membrane and driving electrode, m.

Equating (III) to (IV) and rearranging yields

$$\Delta = \frac{a^2 E_o}{8t\alpha T_m d^2} V^2 \qquad \text{(V)}$$

Design parameters contained in equation (V) and not yet considered are the membrane thickness (t) and the gap distance (d). Reduction of required voltage by reduction of membrane thickness and gap distance is limited only by available materials and fabrication techniques. Gap distance is, of course, limited to at least 10 times the maximum center deflection of the membrane if operation is to conform to the equations which consider the field intensity to be a constant. For example, with deflections of the order of a wavelength (at 6328Å), corresponding to a 100 percent modulation of a 2 CM diameter membrane of poor undeflected flatness, this would be a gap distance of 6.32×10^{-4} CM or 2.5/10,000ths of an inch.

The design of the modulator unit shown in Figures 8a, 8b, 9a, and 9b was obtained from a consideration of all parameters associated with its performance. This is an integral electrostatic modulator unit. This type of construction was selected to separate the problem of fabrication of the cube corner reflector from that of the modulating surface. This approach has the following advantages:

(1) The cube corner reflectors can be completely assembled and tested prior to installation of the modulating elements.

(2) The modulating surface can be assembled into the cube corner reflector using elements that have been individually tested, allowing rejection of elements that do not meet specifications prior to completion of the retromodulators.

(3) Electrostatic modulator units that are damaged or fail during assembly or test can be replaced.

The Chem-milled modulator was designed to be mounted on one face of the retroreflector described in this section. The nickel pressure relief tube is designed to extend through one plate of the retroreflector. The Chem-milled modulator will be held to the retroreflector surface with epoxy.

Note that no epoxy will be between the modulator and the retroreflector surface. The two sides of the Chem-milled modulator have been machined parallel to 1 arc second. When the back side is in close contact with the surface of the retroreflector, the front side (reflective membrane) is then parallel to the retroreflector surface. The hole for each modulator in the retroreflector surface has sufficient clearance that the Chem-milled modulator's position can be adjusted in relation to adjacent units. This allows loose fabrication tolerances on the pressure relief tube installation.

The electrical connections between the adjacent membranes are made with conductive epoxy between the mylar tabs. The nickel tubes are weld-connected together with bus bars. The electrostatic modulator array is thus connected in parallel and two leads are brought out to the driver unit. See Figure 9b.

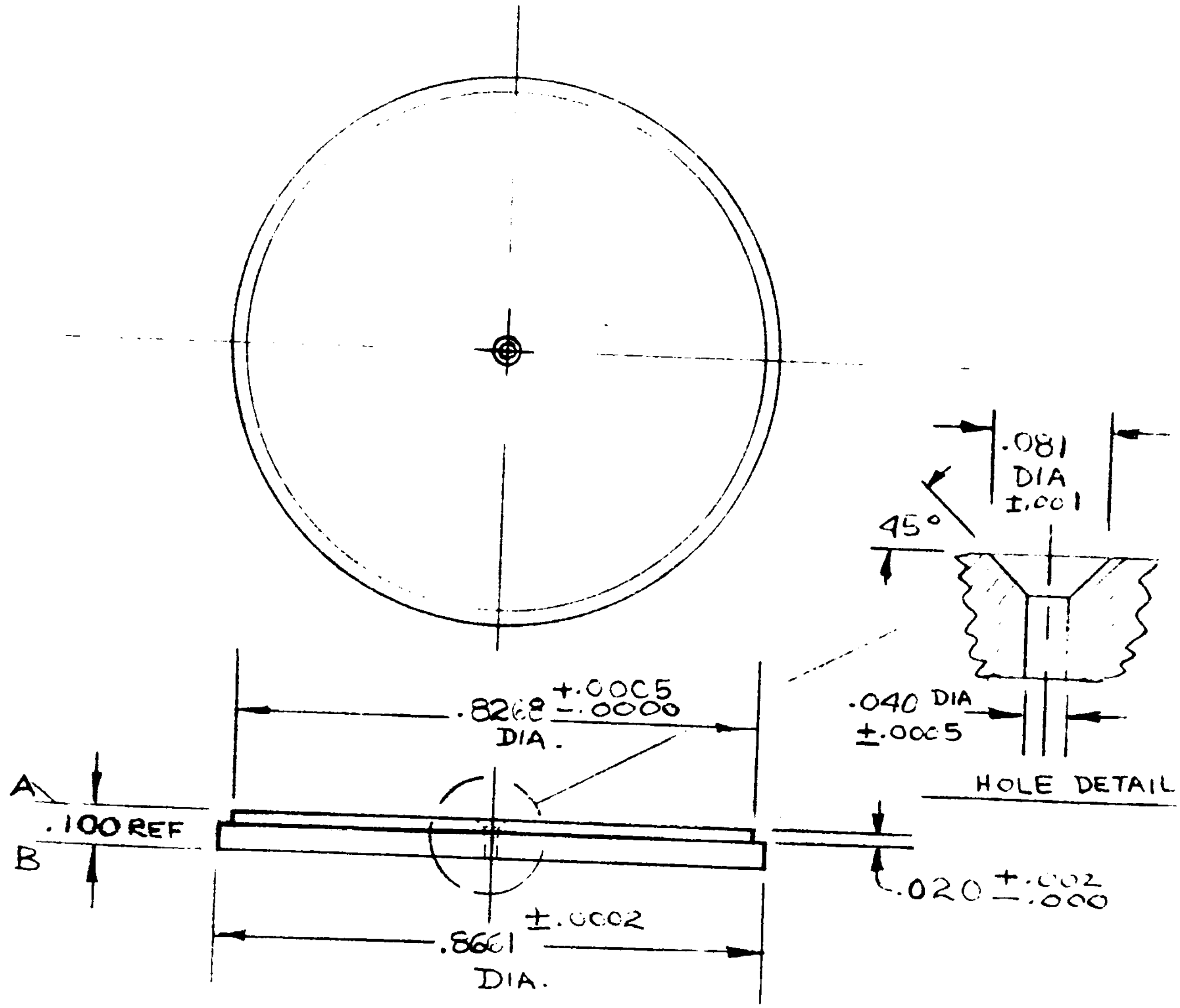

FIGURE 8a

2. SURFACE A & B FINISHED FLAT WITHIN 1/20 WAVE @ .6328 MICRON
1. SURFACE A PARALLEL TO SURFACE B TO 1 ARC [illegible] OR LESS
NOTES:
BLANK AS SUPPLIED

MATL - GE 102 FUSED QUARTZ

FIG. 1 DRAWING NO. 14[illegible]/A

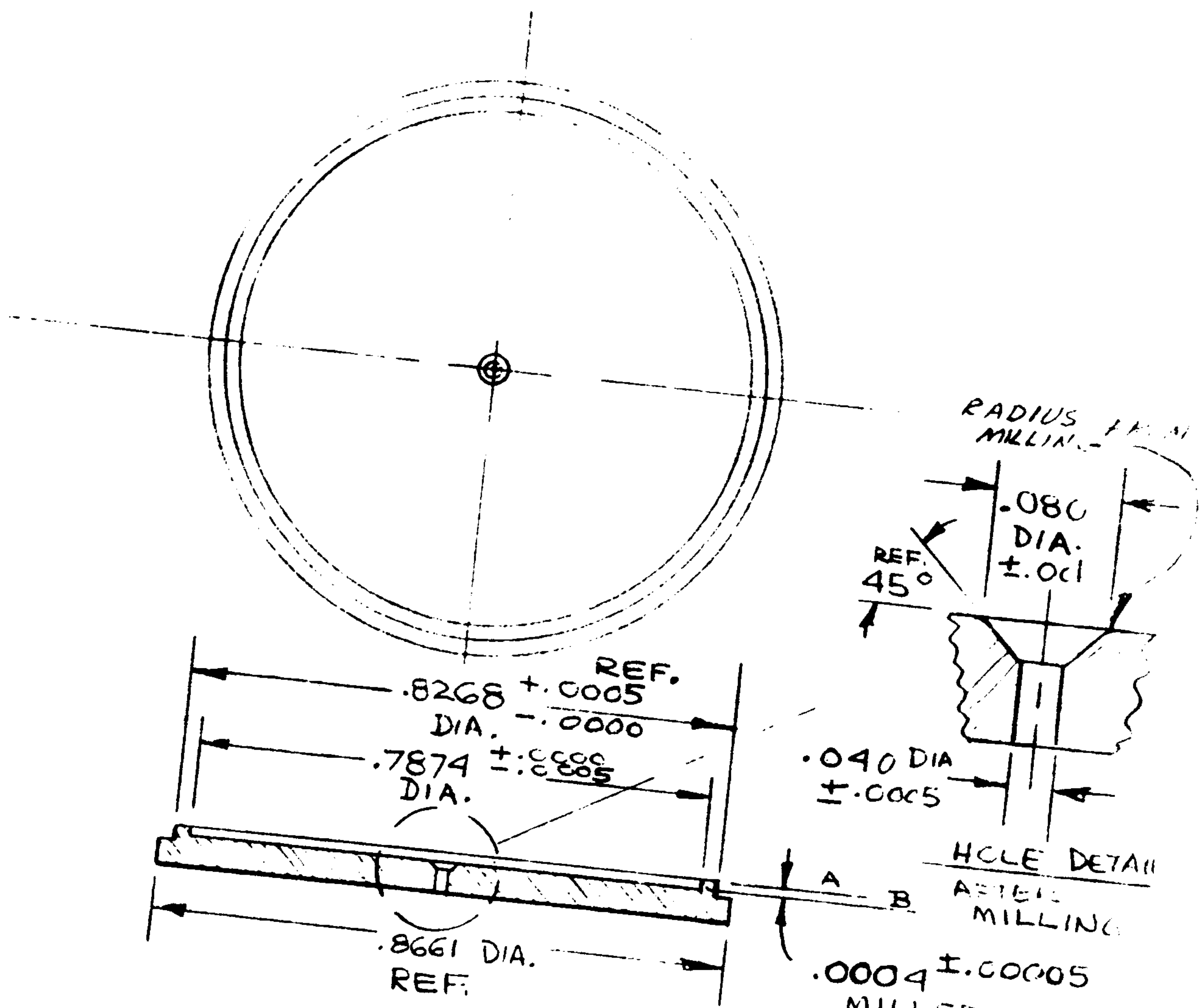

FIGURE 8b

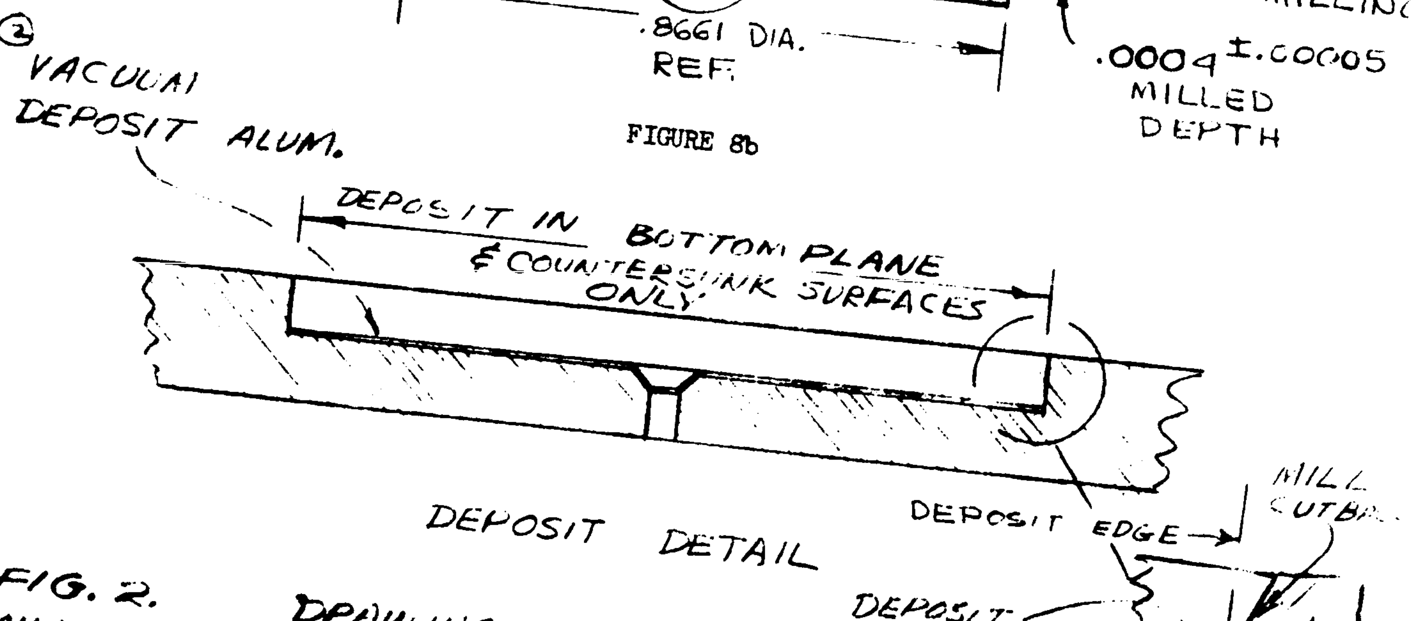

FIG. 2. DRAWING NO. 74340388A

MILLED BLANK & DEPOSIT DETAIL

MATL OF DEPOSIT — ALUM.

2. DEPOSIT 5 TO 10 MICROINCH THICKNESS

1. SURFACE "A" PARALLEL TO SURFACE "B" WITHIN 4" OF ARC.

NOTES:

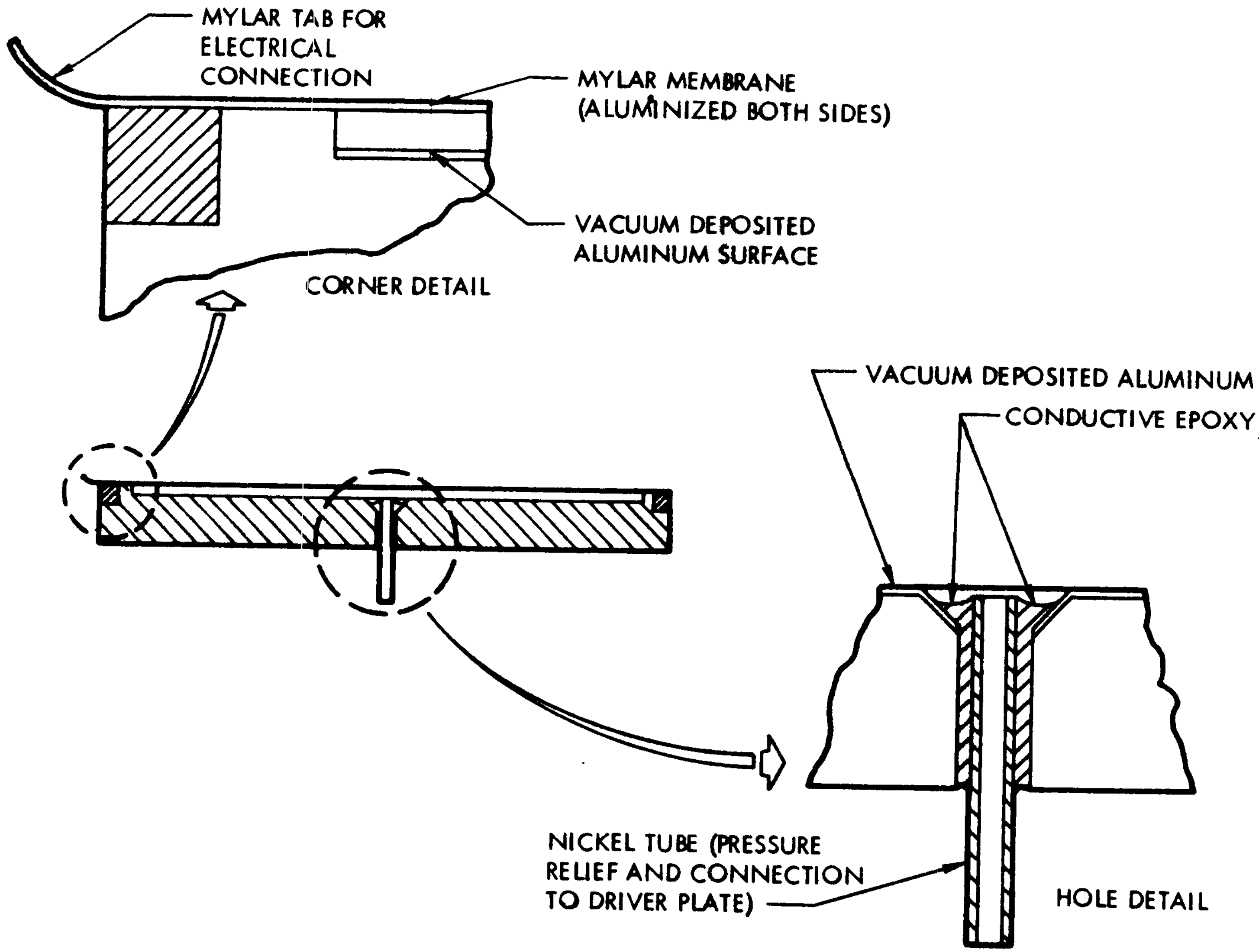

Figure 9A Chem-milled Electrostatic Modulator

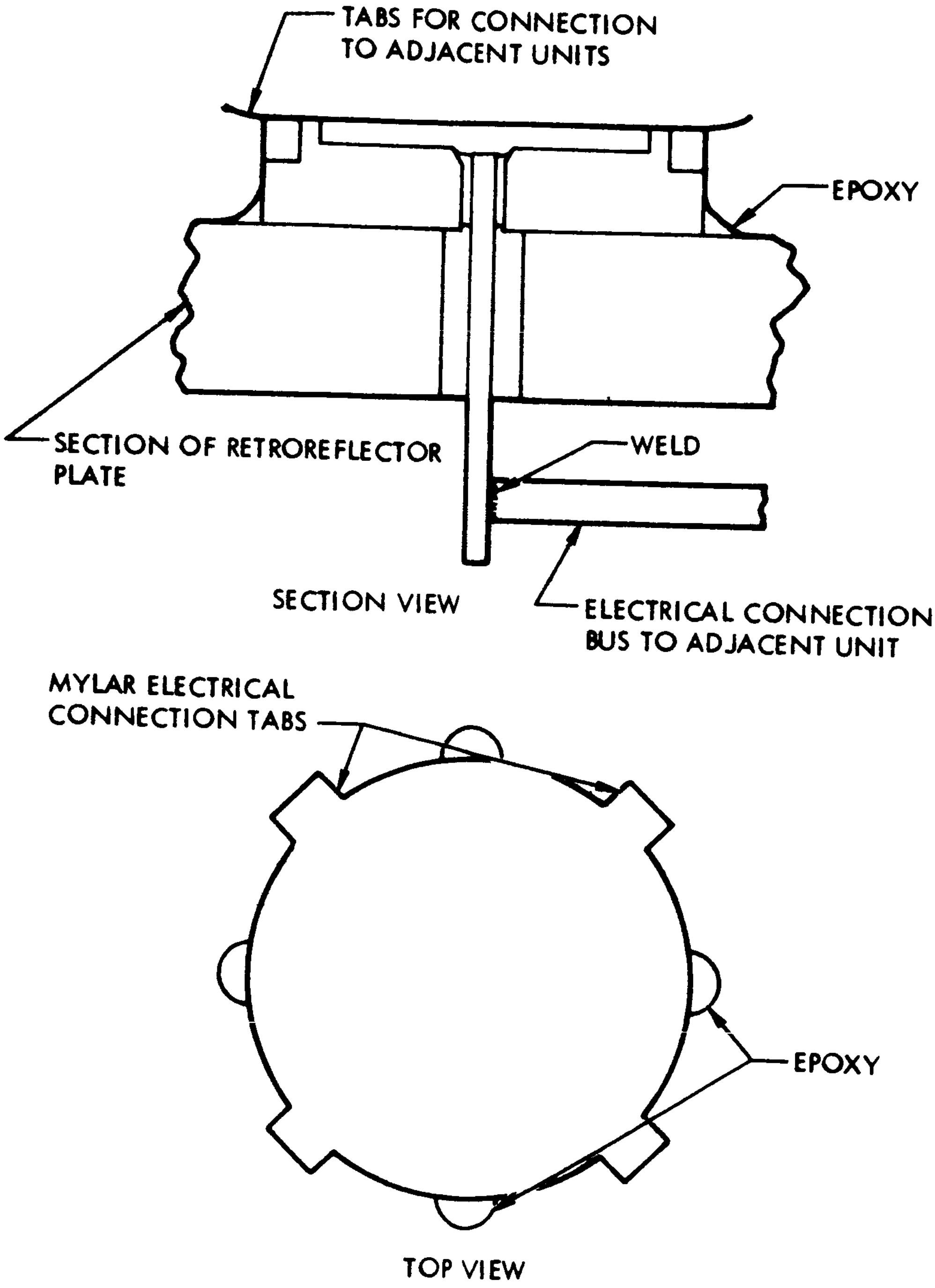

Figure 9B Proposed Mounting of Chem-milled Modulator in Retroreflector

OPTICAL RECEIVER

The design effort on the Optical Receiver, during Phase I of the MIROS Program was limited to a study and analysis of the general structure of its optical and electronic components. These structures together with their operating characteristics are described in some detail in the ensuing paragraphs. The work completed in this area is sufficient to provide a sound basis for the detailed design of the Optical Receiver.

As shown in Figure 10, the optical system consists of a spectral filter, three double convex lenses, a stop and PM tube. All these elements can be contained in a 2.75 inch diameter cylindrical tube. The spectral filter is of the narrow pass interference type and has a maximum transmission at .6328 microns of about 60%.

The three double convex lenses form the collector objective lens. These together with the field stop located in the focal plane, restrict the total field of view to 40°. The on-axis aperture diameter is approximately 2.4 inches. Vignetting introduces a 20% collecting loss at the extremes of the field of view.

The drawings, Figure 11 and Figure 12, are included in this report to show the detail fabrication requirements for the filter and lens system. They, in essence, indicate the feasibility of the optical structure. The final material selection and design will be accomplished during a later phase of the MIROS Program.

The signal-to-noise ratio at maximum range (1000 Kilometers) for the MIROS Optical Receiver, using an RCA 7326 photomultiplier tube is computed from the standard range equation to be 1.16, i.e., 1.3 db. (This computation is presented at the end of this section of the report.)

This is the S/N for background and signal shot noise limited operation. Other sources of noise, arising within the tube, are dynode noise and dark current. According to a DuMont handbook on multiplier phototubes[2], the former normally contributes about 20% of the noise-in-signal, while the latter includes all noise which is not signal dependent (thermionic, gas ionization, ohmic leakage, light feedback, envelope charging, and bleeder supply noise). If the 20% figure for dynode noise is typical, the effective total noise-in-signal is

$$\frac{S}{N} \approx \frac{1.16}{1.25} = 1.04 \text{ or } 0.3\text{dB.}$$

The RCA type 7326 has a maximum equivalent anode dark current input of 1.4×10^{-9} lumen and a cathode luminous sensitivity of 150 μa/lumen. The product of these is the photocathode dark current, 2.1×10^{-7} microamperes. This is negligible compared to that produced by the signal (1.60×10^{-8} watt $\times$ 2.6×10^{-2} amps/watt $= 4.2 \times 10^{-4}$ microamperes), so the system is background and noise-in-signal limited.

2.
"DuMont Multiplier Phototubes," Third Edition. Electronic Tube Sales Department, DuMont Laboratories, Division of Fairchild Camera and Instrument Corporation, Clifton, New Jersey, March 1963.

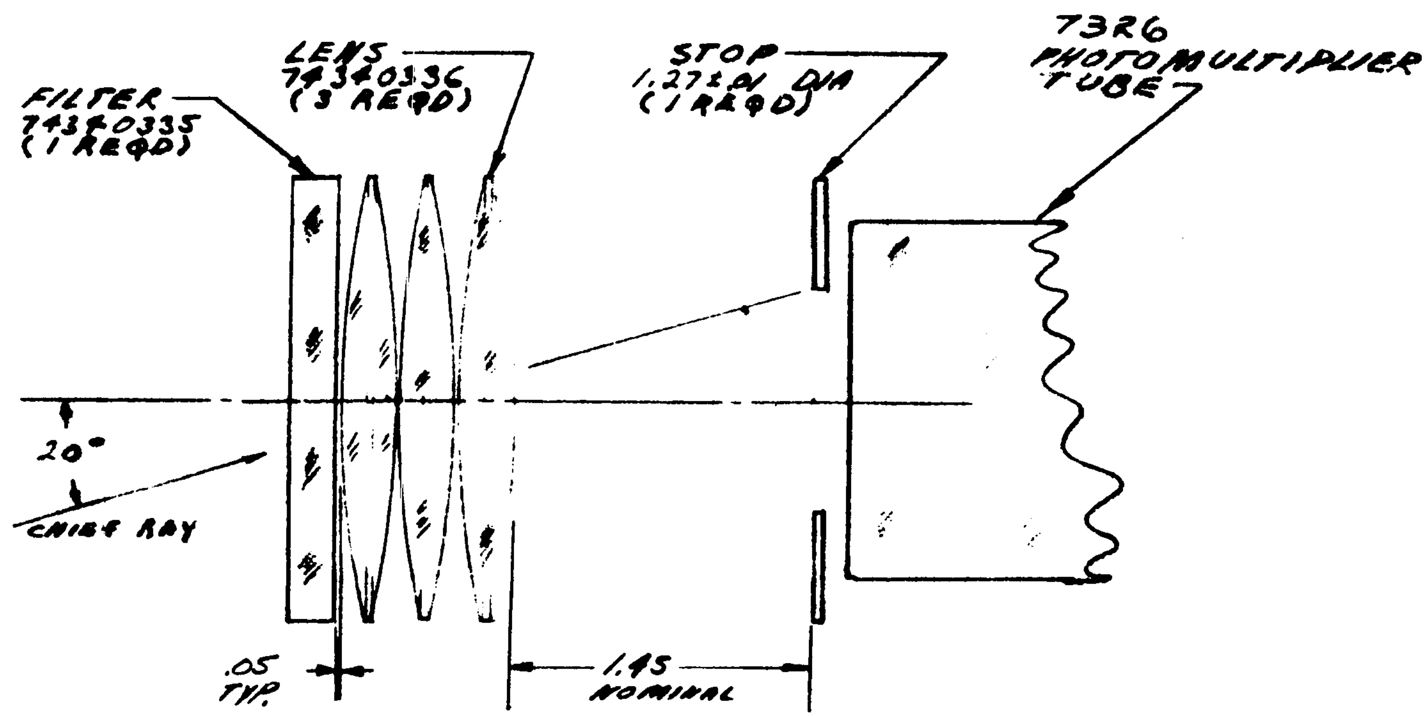

OBJECTIVE EFL — 1.75 inch
FIELD OF VIEW — 40°
OBJECTIVE APERTURE — 2.4 inch
20% VIGNETTING AT EDGE OF FIELD

RECEIVER,
OPTICAL SYSTEM

FIGURE 10

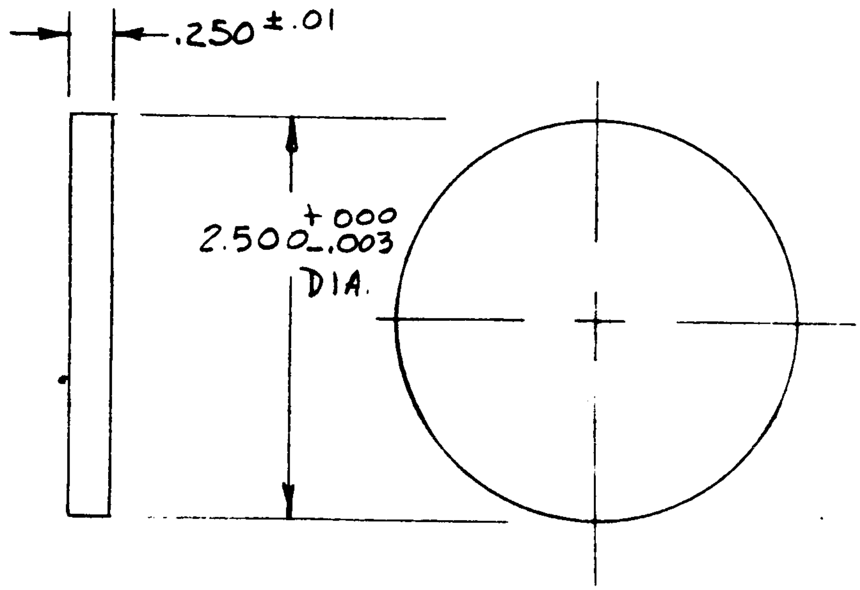

5 FILTER: TO PASS BETTER THAN 60% OF .6328 MICRON LIGHT. TRANSMISSION TO BE LESS THAN 10% AT AND BEYOND 50 ANGSTROMS FROM CENTER WAVE LENGTH THIS SHOULD APPLY FOR LIGHT INCIDENT FROM 0° TO 20°. HIGH AND LOW BLOCKING APPROPIATE FOR S-20 PHOTOSENSITIVE SURFACE

4 ANTI REFLECTION COATING ON BACK SURFACE
3 SURFACES PARALLEL TO 10 ARC MINUTES
2 SURFACE QUALITY 80-50 PER MIL-O-13830
1 SURFACES FLAT TO 3 WAVE NA LIGHT

MATERIAL: GRADE A BSC-2 517-645 PER JAN-G-174

FIGURE 11

NARROW BAND PASS FILTER
74340335

9-15-64 JAE

COPY

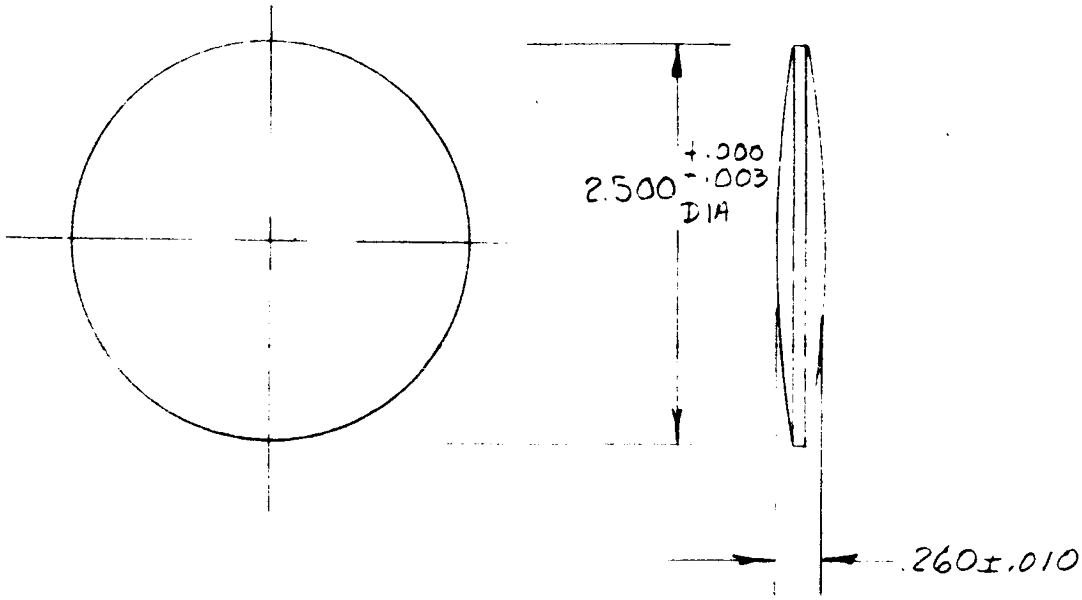

5 ANTIREFLECTION COATED FOR 95% TRANSMITTANCE
OF .6328 MICRON LIGHT
4 SURFACE QUALITY 30-50 PER MIL-O-13830
3 CENTER TO .01 INCH
2 SPHERICITY 4 WAVES NA LIGHT
1 R1 = R2 = 7.0 ± 0.1 INCHES

NOTES

MATERIAL: GRADE A EDF-3
720-293 PER
JAN-G-174

FIGURE 12

DOUBLE CONVEX LENS

74340336

9-15-64 JAB

COPY

Signal to noise ratio calculations for MIROS Optical Receiver:

<u>Definition of symbols</u>:

W_t = Signal power at receiver

W_b = Background power at receiver

P_t = Transmitter power output

θ_t = Half-angle spread of transmitted beam

A_m = Receiver lens area

B_d = Background radiation

η = Quantum efficiency of PMT

Υ_1 = Optical efficiency for signal

Υ_2 = Optical efficiency for background

Δf = Bandwidth

ϕ_m = Receiver half-angular field of view

$\Delta\lambda_m$ = Filter bandwidth

e = Charge on an electron

R = Range

The signal power at the spaceborne receiver is

$$W_t = \frac{P_t A_m \Upsilon_1}{\pi (\theta_t)^2 R^2}$$

and the background power is

$$W_b = B_d A_m (\Delta\lambda_m) \pi (\phi_m)^2 \Upsilon_2$$

For background and signal shot noise limited operation, the voltage signal-to-noise ratio is:

$$\frac{S}{N} = \frac{\eta W_t}{\left[2\eta (W_t + W_b) e \Delta f\right]^{\frac{1}{2}}}$$

The following values are assumed:

P_t = 100 mW

θ_t = 10 arc-seconds (48.6 rad)

$A_m = 2.83 \times 10^{-3}$ m^2 (6 cm diameter)

B_d = 173 watts/m^2/Steradian (sunlit earth)[3]

η = 0.026 amps/watt (S-20 at 6328Å)

τ_1 = 0.42[4]

τ_2 = 0.41[5]

Δf = 20 Kc/sec

ϕ_m = 20°

$\Delta\lambda_m$ = 100A

$e = 1.6 \times 10^{-19}$

R = 1000 Km

Using these values,

$W_t = 1.60 \times 10^{-8}$ watts

$W_b = 7.69 \times 10^{-4}$ watts

$\frac{S}{N}$ = 1.16 or 1.3 db.

The light intensity appearing at the photocathode of the photomultiplier tube varies in strength proportional to the second power of the distance between the transmitting light source and the optical receiver. This distance is presumed to vary from 185 kilometers to 1000 kilometers resulting in a 30 to 1 light signal level variation. A method of compensation for signal level variation or automatic gain

(3) D. S. Bayley, "Technical Note on Optical Communications I," ASTIA No. AD 261583.

(4) Atmospheric transmission is 0.84 (from Bayley lens transmission for the triplet is .86, PMT faceplate 0.95, filter 0.60 at 6328A (all assumed). The product of these is 0.42.

(5) Lens (triplet) .86, PMT faceplate 0.95, and filter average 0.50 (all assumed). The product is 0.41.

control involves varying the cathode to anode voltage of the photomultiplier tube to keep its average output voltage level constant. Figure 13a illustrates the variation of dynode current gain as a function of cathode to anode voltage for an RCA 7326 photomultiplier. Practical design considerations restrict the useable range of cathode to anode voltages from 800 volts to 2000 volts producing a gain variation of approximately 400. This gain characteristic can be used in an automatic gain control system (AGC) for the Optical Receiver (see Figure 13b).

A typical photomultiplier circuit is shown in Figure 14. MIROS Receiver power requirements limit anode current to approximately 30 ua. The AGC system provides gain control to keep the photomultiplier operating at this 30 ua. level at ranges from 185 KM to 1000 KM. The output voltages and bandwidths possible with this tube configuration are shown in Figure 15 which gives the required anode resistances as a function of desired cutoff frequency. The DC anode voltage is also plotted on the same graph as a function of the cutoff frequency.

The output voltage dynamic range will be $\pm$ 1 volt maximum. Calculations were performed to determine the gain variation necessary to compensate for the range of operation. The supply voltage of 1240 volts would be the nominal voltage used for a range of 430 kilometers with a median gain tube. Variation of $\pm$ 325 volts in the supply voltage is necessary to keep gain of the system constant.

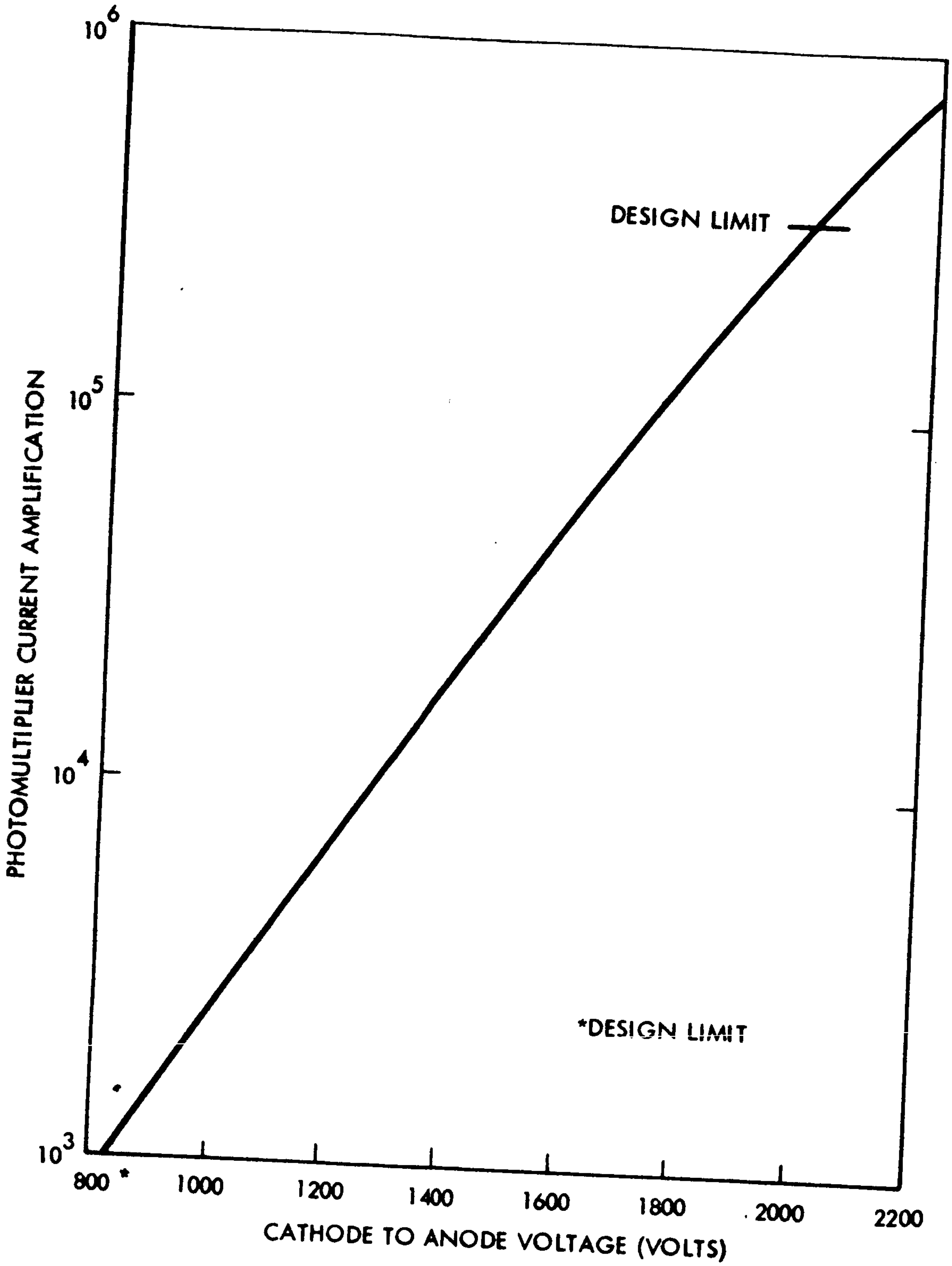

Figure 13A.RCA 7326 Gain Characteristics

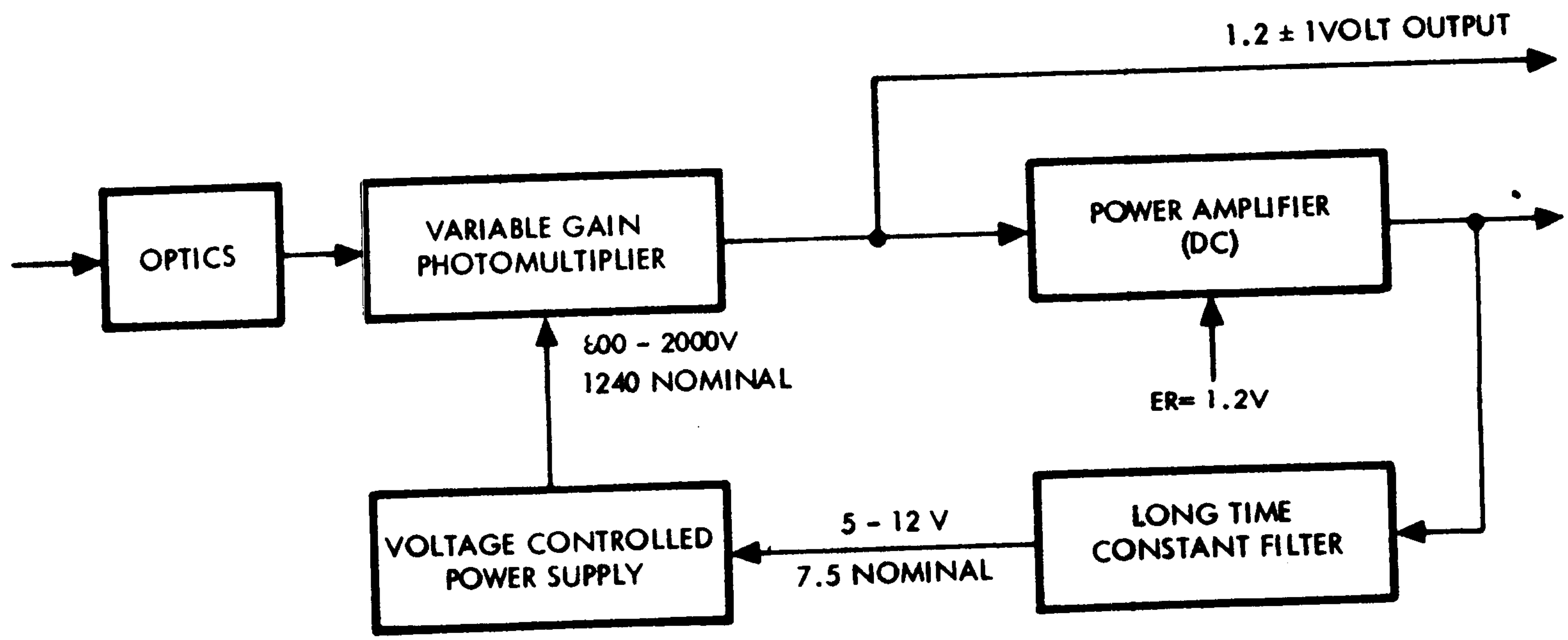

Figure 13B MIROS Optical Receiver System Block Diagram

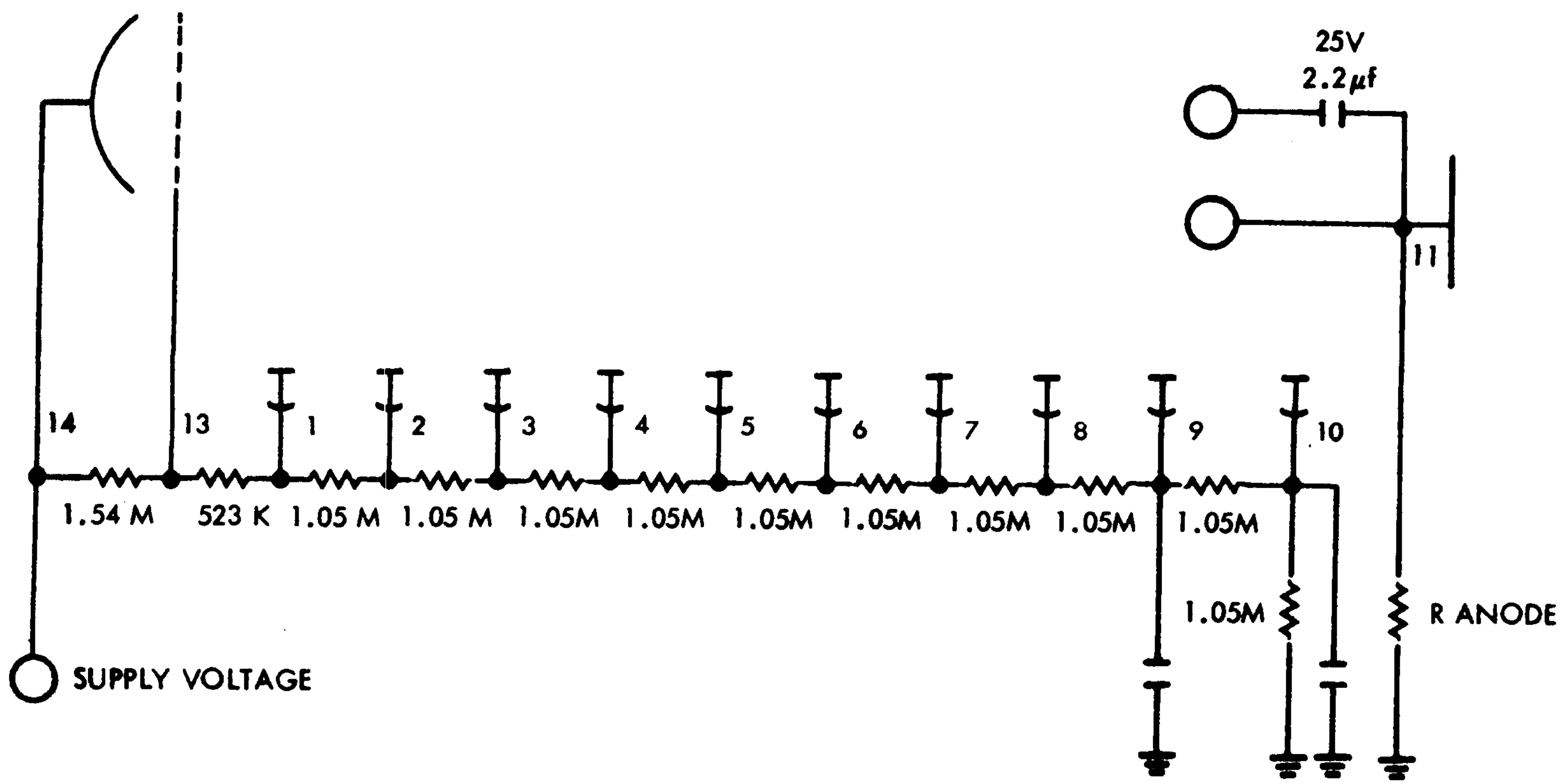

Figure 14. Low Power RCA :326 Multiplier Phototube Circuit

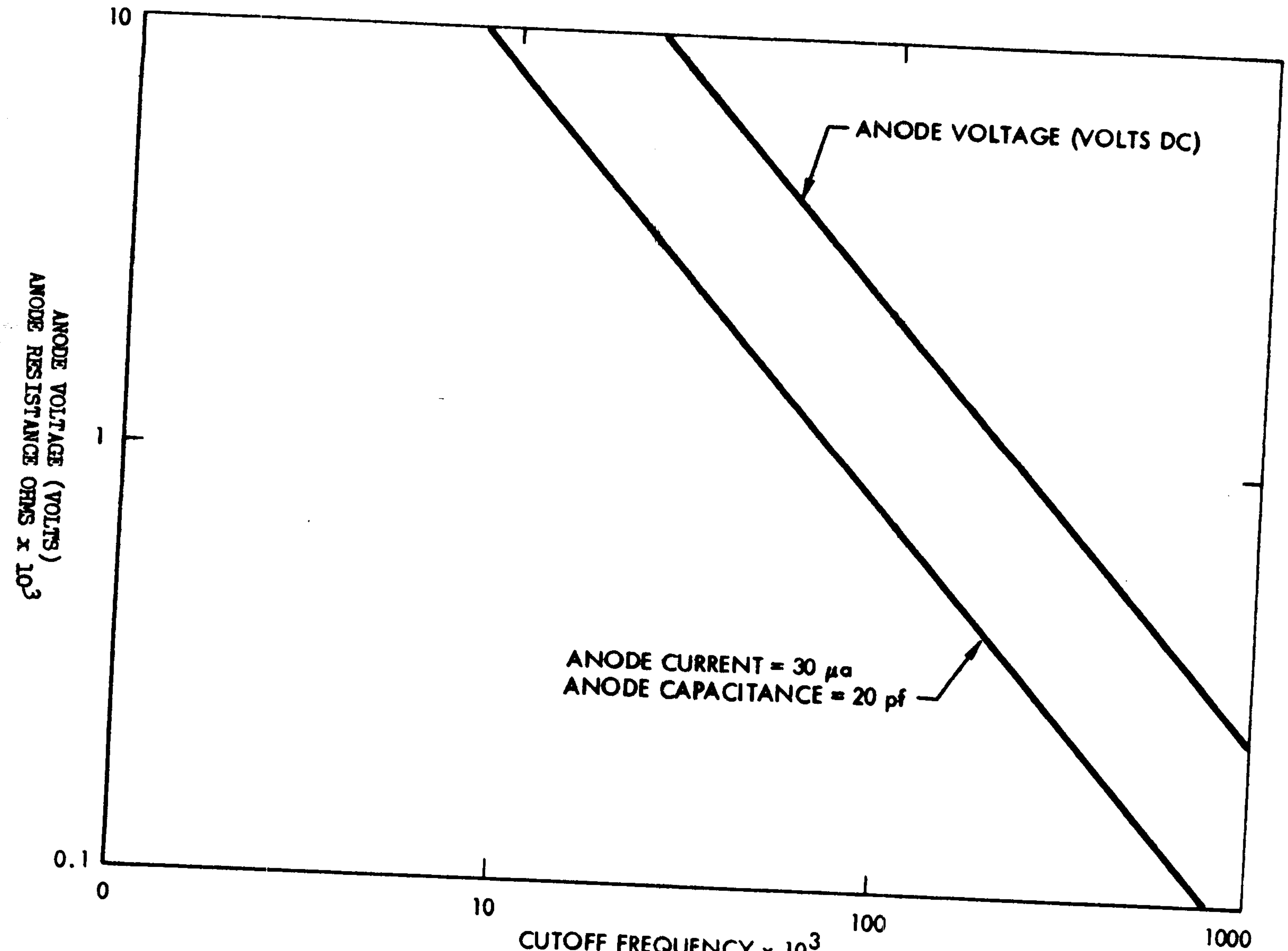

Figure 15. Anode Resistance vs Cutoff Frequency
Anode Voltage vs Cutoff Frequency

To handle non-median gain phototubes requires still greater operating range. High gain tubes are more of a problem than low gain tubes since there is a limit to the minimum practical supply voltage. With a minimum supply voltage arbitrarily selected at 800 volts, increases of gain of 60% can be compensated for in high gain tubes. For gains higher than this the number of dynodes used must be reduced. For low gain photomultipliers an additional 12 DB of gain is available by increasing the supply voltage to 2000 volts (2000 volts has been selected as the upper limit of phototube operation). An absolute maximum supply voltage of 2400 volts is given. (The 2000 volt figure was arrived by derating for reliability and to minimise power consumption.) Power dissipation in the photomultiplier can be calculated for any supply voltage from the following equation.

$$P_{PM} = E_s^2 \times 8 \times 10^{-8} + E_s \times 3 \times 10^{-5}$$

where E_s is the cathode to anode voltage

This equation is plotted graphically in Figure 16. The circuit shown in Figure 17 illustrates a typical configuration for a voltage controlled power supply. An emitter follower (Q5) serves as a variable power supply for a push-pull amplifier composed of Q3 and Q4. The push-pull amplifier operates in the switching mode with the transistors being driven from saturation to cutoff by a free running R-L multivibrator operating at 200 KC or higher to reduce the size of the transformers needed as well as the filter capacitors. A voltage doubler and filter are used after the output stage to reduce the number of turns needed in the secondary of T2 to reduce the effects of interwinding capacitance at high frequencies.

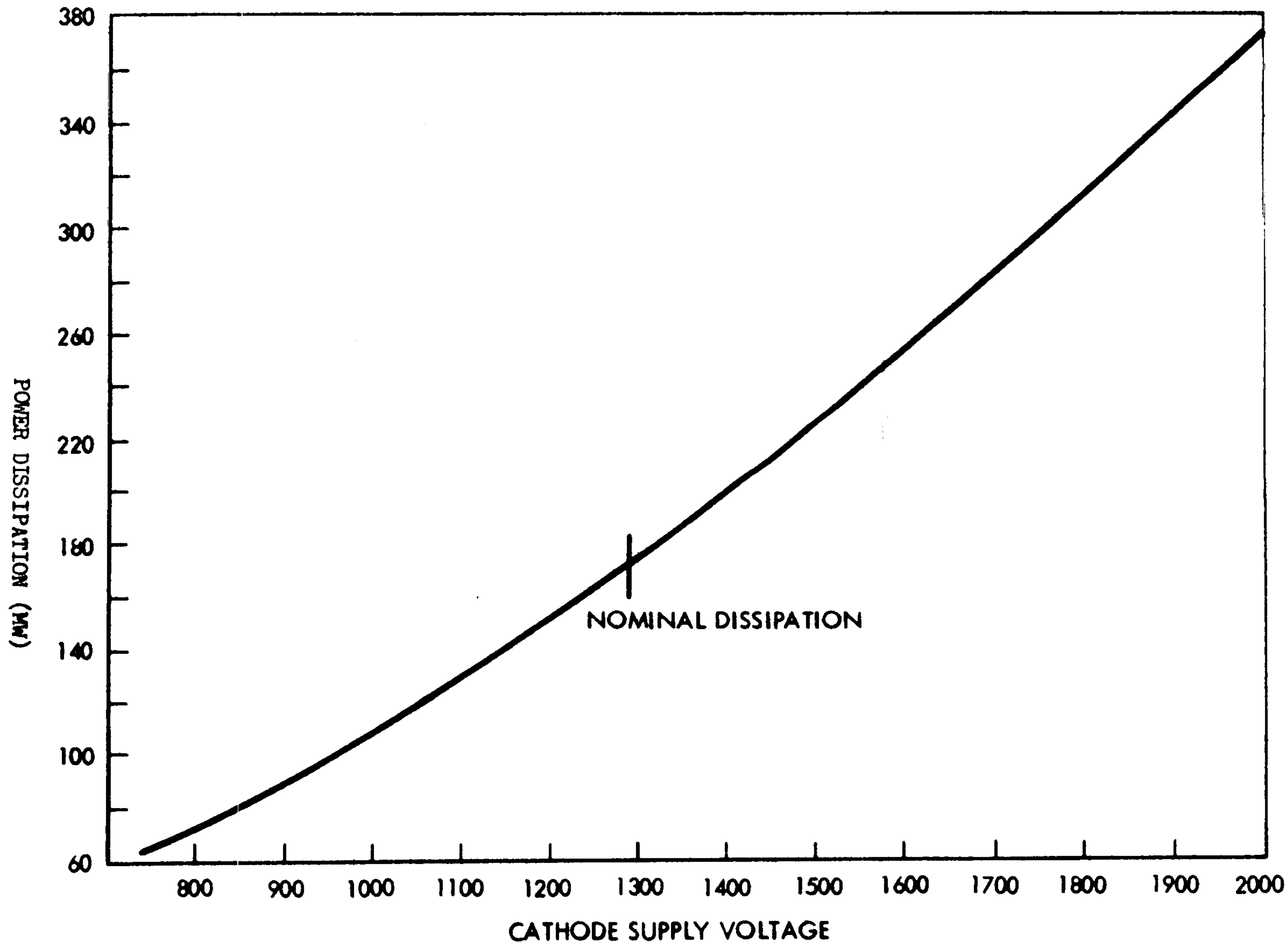

Figure16. Photomultiplier Power Dissipation

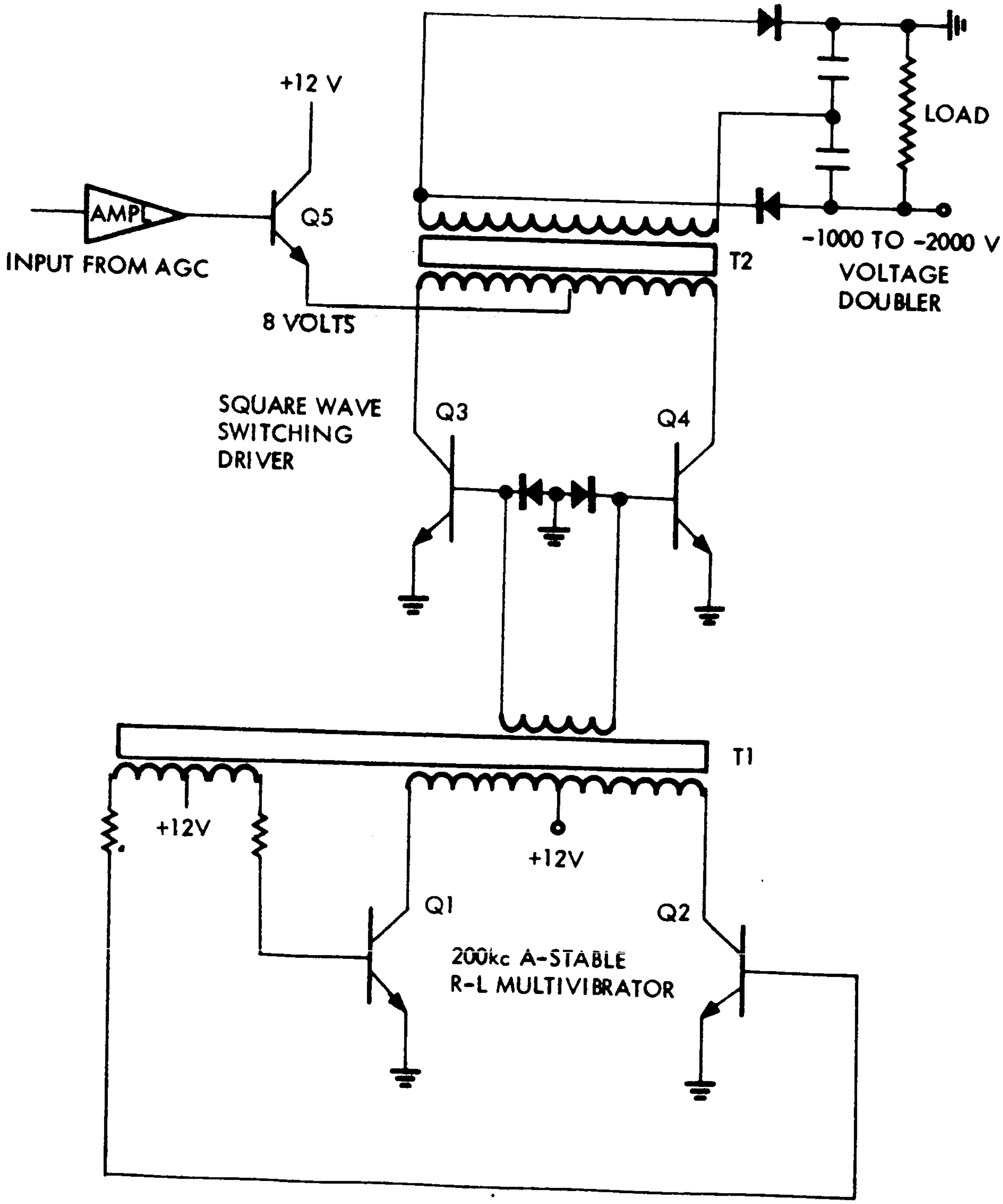

Figure 17. PM - AGC Power System

Tentative specifications for the power system follow:

Output Voltage -	Maximum	2000 volts
	Nominal	1240 volts
	Minimum	800 volts
Input Voltage	Maximum	12 volts
	Nominal	7.5 volts
	Minimum	4.8 volts

Ripple - Less than 1 volt peak-to-peak

Lowest Ripple Frequency 200 KC (Quadrature)

Maximum Current Output 200 microamperes

$$\text{Converter Gain} = \frac{2000\ \text{volts}}{12\ \text{volts}} = 167 \pm 5\%$$

Since the voltage gain of the DC to DC converter is 167, a dynamic input range of $\pm$ 2 volts is sufficient to give the necessary gain compensation. Doubling this dynamic range handles the variation of photomultiplier gains normally encountered. The output current of the photomultiplier is held constant within bounds determined by the AGC system at 30 ua. An additional amplifier and long-time constant filter is necessary in the system to provide the necessary AGC frequency response characteristic and to provide additional gain. If the 30 ua operating point is to be held to $\pm$ 1 ua, the amplifier must convert a change of 1 ua into a 2 volt signal into the power supply. The gain of this amplifier then is 2 volts/ua.

SECTION 2

PERFORMANCE ANALYSIS

ELECTROSTATIC MODULATOR UNIT D.C. TRANSFER FUNCTION

This section will be concerned with the derivation of the modulation D. C. transfer curve for a membrane modulator. The modulation D. C. Transfer curve is defined as the light intensity at the center of the far field image pattern as a function of applied voltage. Two cases will be treated. The first case is based on the assumption of an ideal spherical membrane, i.e., a spherically perfect, defect-free membrane. In the second case, the spherical membrane considered possesses a graininess and other defects and hence will be treated as an aberrated system.

CASE I:

In the operation of the membrane modulator, collimated light is reflected from the membrane, and because of possible spherical membrane deformation, the reflected beam may no longer be collimated. The intensity of the beam in the forward direction (i.e., the direction the reflected beam would travel if the membrane were flat) will vary with the amount of deformation of the membrane. The amount of deformation is measured by the sagitta, Δ , of the deformation. To measure and to analyze the relationship between the sagitta and the intensity in the forward direction in the far field, we may pass the reflected beam through a lens and bring it to focus. The intensity at the center of the focal spot is proportional to the intensity in the far field. We let $\mu(\vec{x})$ be the complex amplitude of the image at the image point $\vec{x}$ in the focal plane. Then

$$U(\vec{x}) = \mu^*(\vec{x})\mu(x)$$

is the image intensity at $\vec{x}$. We wish to compute U (o). We know that if a lens is illuminated by a wave front with complex amplitude $A(\vec{v})$, where $\vec{v}$ is a position vector in the plane of the lens, then

$$\mu(\vec{x}) = \int d\vec{v}\, A(\vec{v})\, \exp\left\{-i \frac{2\pi}{\lambda F} \vec{v} \cdot \vec{x}\right\}$$

where the integration is over the lens aperture, λ is optical wavelength and F is the lens focal length. Then

$$\mu(0) = \int d\vec{v}\, A(\vec{v})$$

and

$$U(0) = \iint d\vec{v}\, d\vec{v}'\, A^{*}(\vec{v}')\, A'(\vec{v})$$

The wavefront of the beam reflected by the membrane is uniform in amplitude but spherically deformed with a sagitta 2Δ. It may be denoted by

$$A(\vec{v}) = A_0 \exp\left\{-i\, k\, 2\Delta \frac{v^2}{R^2}\right\}$$

where R is the radius of the lens (and also of the beam and the membrane). Thus,

$$U(0) = A_0^2 \iint d\vec{v}\, d\vec{v}'\, \exp\left\{-2i\, k\Delta \frac{v^2 - v'^2}{R^2}\right\}$$

$$U(0) = A_0^2 \int_{-\infty}^{\infty}\!\!\int d\vec{v}\, e^{-2ik\Delta \frac{v^2}{R^2}}\, e^{2ik\Delta \frac{v'^2}{R^2}}\, d\vec{v}'$$

$$U(0) = A_0^2 \int_0^{2\pi} d\theta \int_0^R v\, dv\, e^{-2ik\Delta \frac{v^2}{R^2}} \int_0^{2\pi} d\theta' \int_0^R v'\, dv'\, e^{2ik\Delta \frac{v'^2}{R^2}}$$

$$U = 4\pi^2 A_0^2 \int_0^R v\, dv\, e^{-2ik\Delta \frac{v^2}{R^2}} \int_0^R v'\, dv'\, e^{2ik\Delta \frac{v'^2}{R^2}}$$

$$U(0) = 4\pi^2 A_0^2 \left[\frac{R^2}{-4ik\Delta} e^{-2ik\Delta \frac{r^2}{R^2}}\right]_0^R \left[\frac{R^2}{4ik\Delta} e^{2ik\Delta \frac{r^2}{R^2}}\right]_0^R$$

$$= \frac{4\pi^2 A_0^2 R^2}{4\cdot 4 k^2 \Delta^2}\left[1 - e^{-2ik\Delta}\right]\left[1 - e^{2ik\Delta}\right]$$

$$= \frac{\pi^2 A_0^2 R^2}{4k^2\Delta^2}\left[2 - 2\cos 2\Delta k\right]$$

$$= \frac{\pi^2 A_0^2 R^2}{k^2\Delta^2}\left[\frac{1-\cos 2\Delta k}{2}\right]$$

$$= \frac{\pi^2 A_0^2 R^2}{k^2\Delta^2}(\sin \Delta k)^2$$

$$= (\pi A_0 R)^2 \left(\frac{1}{\Delta k}\right)^2 (\sin \Delta k)^2$$

$$U(0) = (\pi A_0 R)^2 \left(\frac{\sin x}{x}\right)^2$$

where x = k.

Now normalizing the response $U(0)$ vs. Δ so that the maximum value is unity and the minimum zero, we get the D. C. transfer function

$$T_{DC}(\Delta) = \left\{\frac{\sin(\Delta k)}{\Delta k}\right\}^2$$

In Figure 18, we plot $T_{DC}(\Delta)$ vs. $\sqrt{k\Delta}$. We do this because $\sqrt{k\Delta}$ is proportional to the modulating voltage. The experimental curve in Figure 18 is adjusted to produce a good fit of the second peak. This fit is presumed on the basis of the analysis made in Case II.

CASE II:

Collimated light is directed onto an aluminized membrane, is reflected and brought to focus by a diffraction limited lens. If a voltage is applied across the membrane it will deform, the deformation being proportional to the square of the applied voltage, thus varying (modulating) the light intensity at the center of the diffraction image. The light intensity variation can be calculated directly from Kirchoff-Fresnil diffraction theory as was done in the previous section. However, the quantity being calculated is directly related to the Strehl Definition,[6] D, of the optical system. (D is defined as the ratio of the intensity at the center of the image formed by an optical system from collimated light to the intensity at the center when all components in the system are ideal, (i.e., diffraction limited). It has been shown[6] that the Strehl Definition is proportional to the integral over spatial frequency f, of the optical system image modulation transfer function, $\Upsilon(\vec{f})$.

$$D = A\int d\vec{f}\,\Upsilon(f) \tag{1}$$

Evaluating the integral provides another approach to the calculation of the D. C. transfer function of the membrane $T_{DC}(\Delta)$. This method is much more complicated than the previous method but permits treatment of the effect of

---

6 O'Neill, Edward L., "Introduction to Statistical Optics", Addison-Wesley Publication Company, Reading, Mass., 1963, pg. 88.

FIGURE 18

MODULATION TRANSFER CURVES

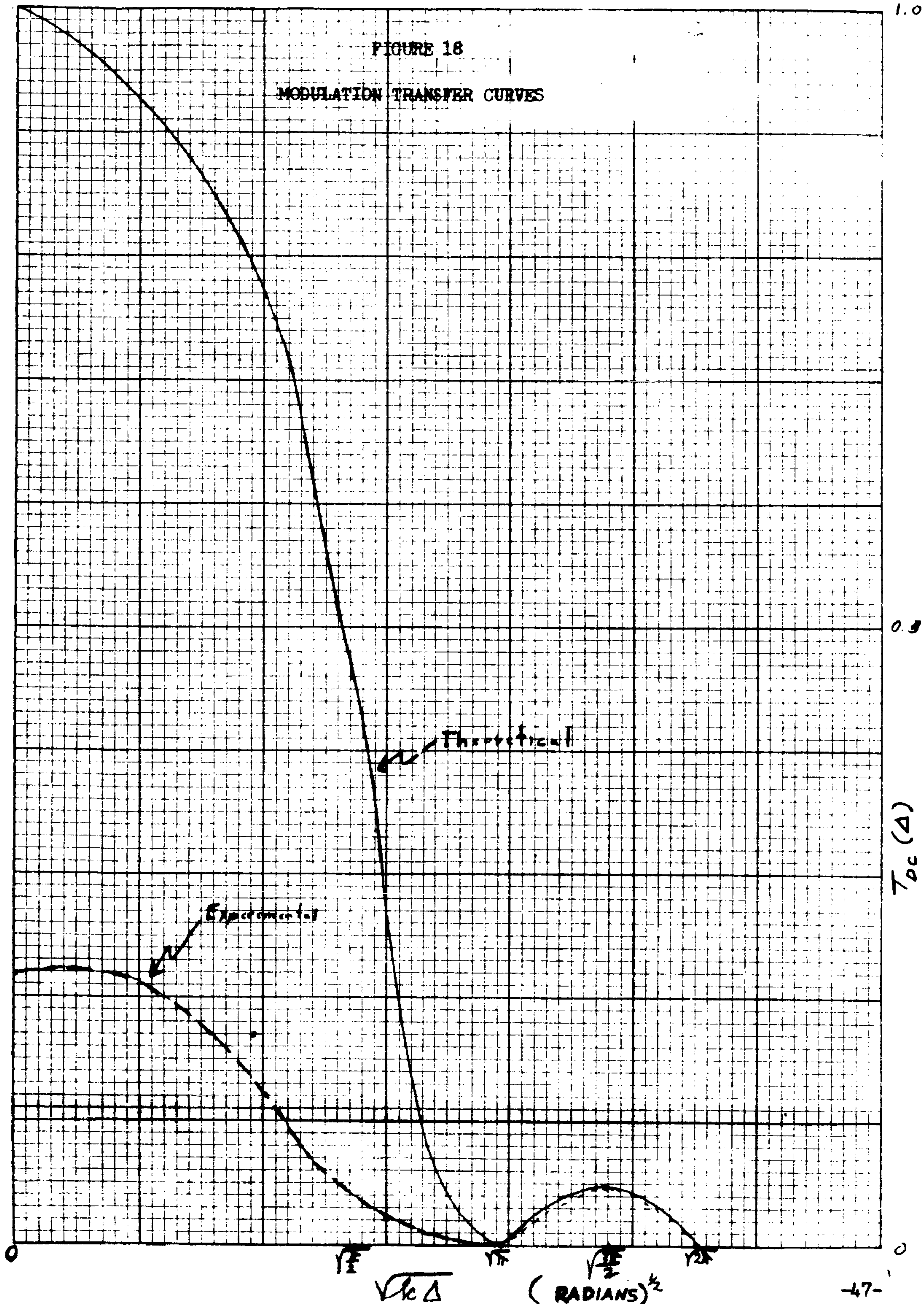

membrane irregularities on $T_{DC}(\Delta)$. If $\Upsilon(\vec{f},\Delta)$ is the image modulation transfer function when the membrane is ideal but bowed with sagitta Δ , then

$$T_{DC}(\Delta) = \int d\vec{f}\ \Upsilon(\vec{f},\Delta) \tag{2}$$

(A and B are both constants of proportionality in Equations (1) and (2). The function $\Upsilon(\vec{f},\Delta)$ has been evaluated by Hopkins[7] and found to be expressible in terms of an infinite series of bessel functions. We will not work with the expressions but with the graphs of $\Upsilon(\vec{f},\Delta)$ for various Δ , shown in Figure 19[8]. (Note that Υ is dependent only on f , the magnitude of $\vec{f}$, not on its orientation.) It has been shown[9] that the effect of random wavefront distortion on the modulation transfer function of an optical system can be expressed as an additional factor $T_D(f)$ which is to be multiplied by $\Upsilon(f,\Delta)$ to give the composite modulation transfer function. If σ^2 is the variance of the phase distortion (in radians) and C (r) is the spatial correlation of phase distortion for separation r , then

$$T_D(f) = \exp\left\{C(\lambda R f) - \sigma^2\right\} \tag{3}$$

where λ is the wavelength and R is the lens focal length. Assuming σ is not more than a few radians (which it must be if the membrane is reasonably

---

7 Hopkins, H. H., "The Frequency Response of a Defocused Optical System," Proceedings of the Royal Society of London, Series A., Vol. 231, Sept. 20, 1955, pg. 96.

8 Ibid, pg. 98.

9 North American Aviation, Inc., Space & Information Systems. Proposal, "Analysis of Optical Wave Front Distortion Caused by the Atmosphere," Appendix B, SID 64-1946.

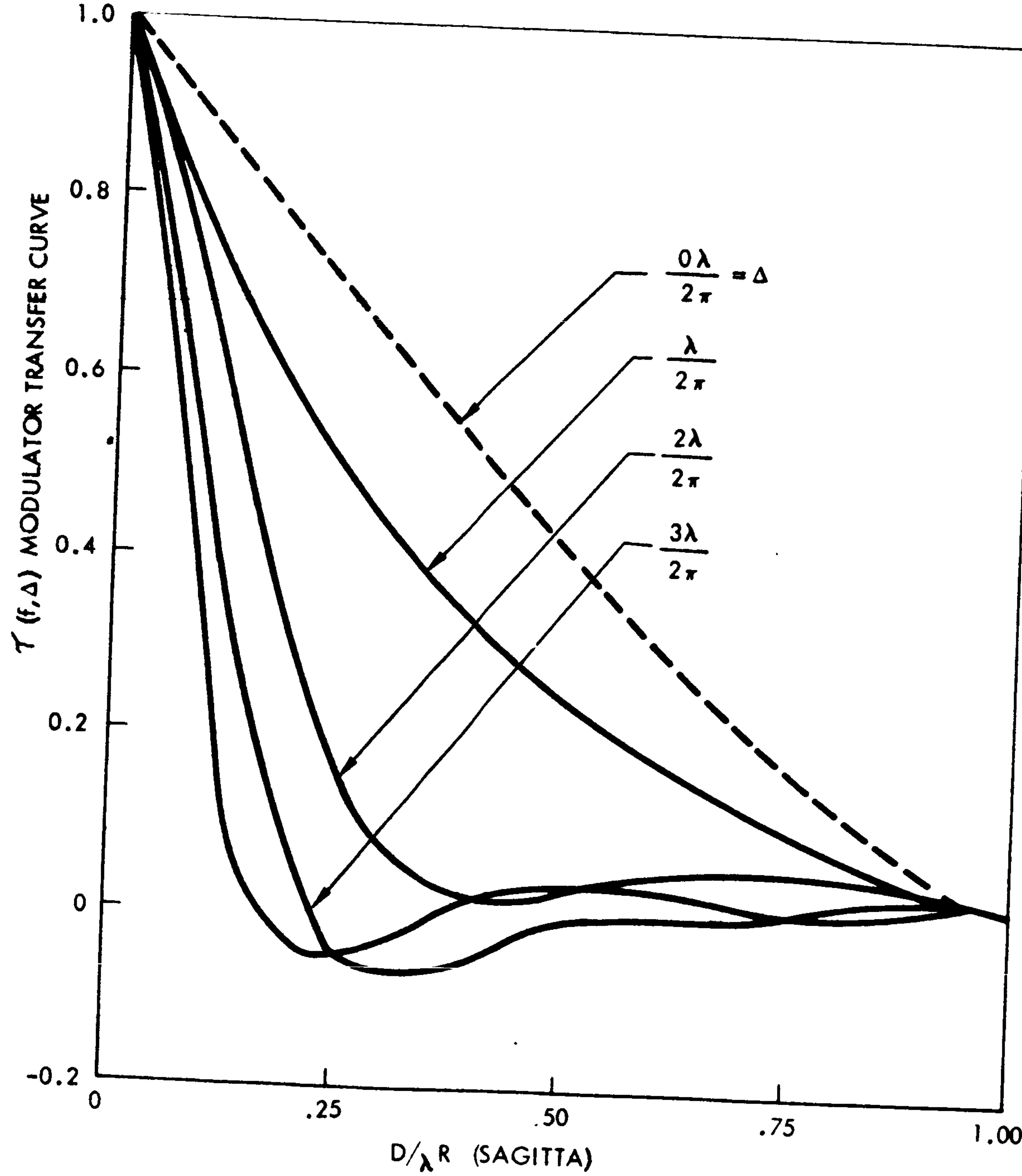

MODULATION TRANSFER CURVES

NON-IDEAL SURFACE PROPERTIES

Figure 19

flat) then $\Upsilon_D(f)$ does not become significant until $C(r)/\sigma^2$ is much less than unity. We may call this distance Λ_0 the correlation distance, and $f_0 = \frac{\Lambda_0}{\lambda R}$ the correlation frequency.

In normal operation, the modulator acquires sagitta which varies the appropriate modulation transfer curves from 0 to $3\lambda/2\pi$ as shown in Figure 19 . If f_0 is located at a higher level than say $D/2\lambda R$ then it can be seen that it will have little effect on

$$\int d\vec{f}\; \Upsilon_D(f)\, \Upsilon(f, \Delta) \tag{4}$$

If f_0 is small than $f_0 D/\lambda R$ then it will have equal effects for virtually all values of Δ giving

$$\int d\vec{f}\; \Upsilon_D(f)\, \Upsilon(f,\Delta) \simeq \exp\{-\sigma^{-2}\} \int d\vec{f}\; \Upsilon(f,\Delta) \tag{5}$$

The conditions on f_0 are equivalent to conditions on Λ_0 i.e., $\Lambda_0 > D/2$ and $\Lambda_0 < D/10$. For values of f_0 (or Λ_0) between the above two values, the effect will have to be calculated in detail. Thus we can distinquish three cases corresponding to the values of f_0, namely: (1) the micro-ripple case, (2) the macro-ripple case, and (3) the intermediate case. In the first case, $T_{DC}(\Delta)$, is modified by a constant factor, $\exp\{-\sigma^2\}$, but not changing the shape of the curve for $T_{DC}(\Delta)$. In the intermediate case, $T_{DC}(\Delta)$ is reduced only for smaller values of Δ and not for large values thus changing the shape of $T_{DC}(\Delta)$.

In summary, we see that for the micro-ripple case the shape of the modulation transfer curve is not changed, but only scaled by a constant factor independent of sagitta. In the macro-ripple case, the scaling factor is dependent on sagitta for small sagittas but quickly becomes a constant as the sagitta increases. Hence, the shape of the modulation transfer curve is changed only at small sagitta values. The intermediate case is between the micro and macro-ripple case. The scaling factor is dependent on sagitta for sagitta values greater than those in the macro-ripple case and does not become a constant until much larger sagitta values are encountered.

ELECTROSTATIC MODULATOR UNIT UNPRESSURIZED MODEL

A stretched circular aluminized membrane forms the top of a cylinder the bottom of which is aluminized. See Figure 30. Aluminizing the bottom of the cylinder allows a bias voltage to be placed across the membrane. This bias voltage reduces the tendency of the driven membrane toward frequency doubling and allows the modulator to be operated in the linear portion of its modulation transfer curve. The differential equation governing the vibration of a membrane stretched with uniform tension over a circular hoop is the two-dimensional wave equation. It is expressed in polar coordinates as

$$\frac{1}{r}\frac{\partial}{\partial r}\left(r\frac{\partial U}{\partial r}\right)+\frac{1}{r^2}\frac{\partial^2 U}{\partial \theta^2} = k^2\frac{\partial^2 U}{\partial \tau^2}$$

where r and θ are polar coordinates, $U(r,\theta,\tau)$ is the displacement normal to the r θ plane and $k^2 = \frac{\rho}{T}$; ρ and T being the density and tension respectively of the membrane. Employing the method of separation of variables, i.e., letting

$$U = R(r)\,\Theta(\theta)\,\Phi(\tau)$$

one can reduce the second order linear partial differential equation down to three linear second-order differential equations:

$$\frac{d^2\Phi}{d\tau^2}+\omega^2\Phi = 0\,, \qquad \frac{d^2\Theta}{d^2\theta}+m^2\Theta = 0$$

$$r^2\frac{d^2R}{dr^2}+r\frac{dR}{dr}+\left(k^2\omega^2r^2-m^2\right)R = 0$$

The solution of the first two equations is straightforward. The solutions are

$$\Phi = A \cos wt + B \sin wt$$

$$\Theta = C_3 \cos n\theta + C_4 \sin n\theta$$

$r^2 \dfrac{d^2R}{dr^2} + \dfrac{r\,dR}{dr} + (k^2 w^2 r^2 - n^2) R = 0$ is a bessel equation and as such its solution is known, namely $R = C_1 J_n (kwr) + C_2 Y_n (kwr)$.

Since the deflection of the membrane is single-valued, Θ must be periodic such that $\Theta(\theta) = \Theta(\theta + 2\pi)$; hence, n must be an integer. This demands that the bessel functions be of integer order. Since $Y_n (kwr)$ becomes infinite at the origin ($r = o$), this solution cannot be physically meaningful in our example, therefore $C_2 = 0$. Furthermore, we assume that the membrane starts its vibration from its equilibrium position with no initial velocity, hence, $B = 0$. Therefore a particular solution to the two dimensional wave equation with the stated conditions with new constants is

$$U (r, \theta, t) = J_n (kwr) \left[C \cos n\theta + D \sin n\theta \right] \cos wt.$$

Now the boundary conditions require that $U = o$ when $r = a$, the radius of the membrane. Therefore, $J_n (kwa) = 0$. The roots of this equation determine the natural angular frequencies of vibration. For any given order n there are theoretically an infinite number of roots; $m = 1, 2, ----$.
The complete solution of the wave equation for our stated conditions is

$$U(r,\theta,\tau) = \sum_{m=1}^{\infty} \sum_{n=1}^{\infty} J_n(k\omega_{mn} r)\left[C_{mn} \cos n\theta + D_{mn} \sin n\theta\right] \cos \omega_{mn} \tau$$

If the membrane were perfectly flat, and absolutely parallel to the bottom of the cylinder, then only the $n = o$ order would be present. However, these conditions are not realized; therefore, higher orders of n will be present in the resonance pattern. The force applied to the membrane is a nearly symmetric force, hence only symmetric oscillatory modes will be present to any great degree, i.e., J_n (kwr) where n is odd will not appear strongly. Furthermore, since the higher roots of J_o (kwr) represents less average displacement but require greater forces to excite, they are damped out. The same is also true for higher even order of n. Namely, for n greater than two. Therefore, one expects, for instance, to find the first three natural frequencies of order $n = o$, the first two of order $n = 1$, and the first frequency for $n = 2$ present in the resonance pattern of the circular membrane. Figure 20 is an experimental plot of modulation index vs. frequency of the driven membrane. The resonance points clearly shows the values as predicted by the theory. In this comparison, we have identified the resonances by assuming that the initial, large resonance is for $q_{o,1}$, i.e., $n = o$, $m = 1$, and taking the ratio of all resonant frequencies to that frequency and comparing the ratios to entries in Table 5.

TABLE 4.

BESSEL FUNCTION ROOTS, $n,_m$

n / m	0	1	2	3	4
1	2.40	3.83	5.14	6.38	7.59
2	5.52	7.02	8.42	9.76	11.07
3	8.65	10.17	11.62	12.02	14.37
4	11.79	13.32	14.79	16.22	17.62
5	14.93	16.47	17.96	19.41	20.83

TABLE 5.

NORMALIZED BESSEL FUNCTION ROOTS, $n,_m/n_{o,1}$

n / m	0	1	2	3	4
1	1.00	1.60	2.14	2.66	3.16
2	2.30	2.93	3.51	4.07	4.61
3	3.60	4.24	4.85	5.44	5.98
4	4.91	5.56	6.16	6.77	7.34
5	6.23	6.86	7.49	8.09	8.69

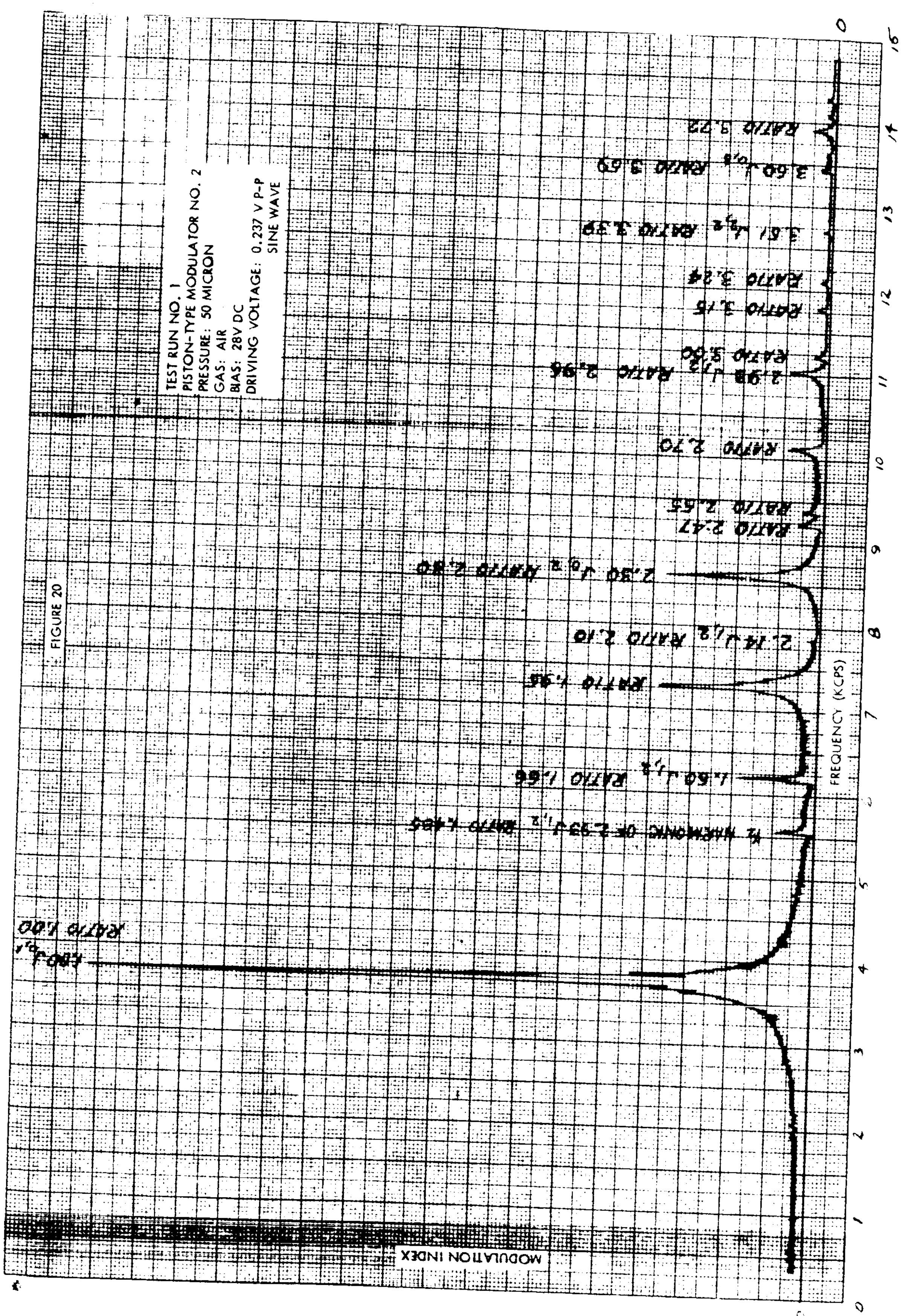
TEST RUN NO. 1
PISTON-TYPE MODULATOR NO. 2
PRESSURE: 50 MICRON
GAS: AIR
BIAS: 28V DC
DRIVING VOLTAGE: 0.237 V P-P
SINE WAVE
FREQUENCY (KCPS)
MODULATION INDEX

FIGURE 20

ELECTROSTATIC MODULATOR UNIT PRESSURIZED MODEL

Now consider the case where the cylinder contains a gas under pressure p. The stretched circular aluminized membrane possesses a restoring force due to the tension applied to it. One can think of this restoring force as analogous to a free, rigid membrane disc connected to a spring with spring constant k. As the membrane deforms, it compresses the gas in the cylinder. The gas on the other side of the membrane generates a uniform restoring force on the membrane caused by the pressure differential. For unit displacement at the center of the membrane, the average displacement of the membrane is α , a quantity less than one which is computed later from the shape of the deformed membrane. The cylinder, which the membrane covers, has a depth L so that for unit displacement of the center of the membrane, the compression is α/L and the pressure increase in the cylinder is approximately $\alpha p/L$. The restoring force on the membrane area A is $\alpha p A/L$. Assuming the membrane acts like a harmonic oscillator, one can calculate the effects of pressure on the first resonance. The equation of motion of the membrane is given by $m\ddot{x} = (k + \alpha p A/L)x$. Dividing through by the mass, m, of the membrane gives $\ddot{x} = \left(\frac{k + \alpha p A/L}{m}\right)x$. This is just the standard form for a harmonic oscillator. Hence the resonant angular frequency is given by $w = \sqrt{\frac{k + \alpha p A/L}{m}}$ If we considered an unpressurized system, we would have obtained $w_o = \sqrt{k/m}$ as its resonant angular frequency. Therefore, expressing w in terms of w_o, one obtains $w = \sqrt{w_o^2 + \alpha p A/L}$. Letting the mass of the membrane be represented in terms of its density, area, and thickness, $m = \rho A t$, and substituting this into the expression for w, one obtains $w = \sqrt{w_o^2 + \frac{\alpha p}{L\rho t}}$. Notice that the effect of pressure is to move the system resonant point to a higher value. Figure 52, test run No. 1, shows the resonance point for an unpressurized system and Figure 53, test run No. 3, shows the resonance points of the same system when pressurized. Hence, we see that pressurization of the system increases the useable bandwidth by raising the first resonance's frequency.

Squaring both sides of $w = \sqrt{W_0^2 + \frac{\alpha p}{L\rho t}}$, one obtains $\omega^2 = \omega_0^2 + \frac{\alpha}{L\rho t} p$

If w^2 vs. p is plotted on linear graph paper from experimental data, the slope of the resulting straight line would be $\frac{\alpha}{L\rho t}$. Knowing the values of L, ρ , and t allows one to calculate α experimentally. Theoretically, the value of α is determined by the area normalization of the membrane amplitude function. For the case of interest, namely the first resonance,

$$\alpha = \frac{\int_0^{2\pi} d\theta \int_0^R r\,dr\, J_0(r)}{\pi R^2}$$

Evaluation of this expression yields a value of .4 for $\alpha_{\text{theoretical}}$. Figures 21 and 22 give the value for $\alpha_{\text{experimental}}$ as .58, decreasing to .27 at higher pressures, suggesting that the membrane shape under pressure does not match J_0 exactly and is pressure dependent. Theory and experiment are in reasonable agreement. Therefore, it is reasonable to assume that the electrostatic membrane modulator's characteristics can be described with reasonable quantitative accuracy by the mathematical model used, and extrapolation to relatively high pressure and high resonant frequencies should be straightforward.

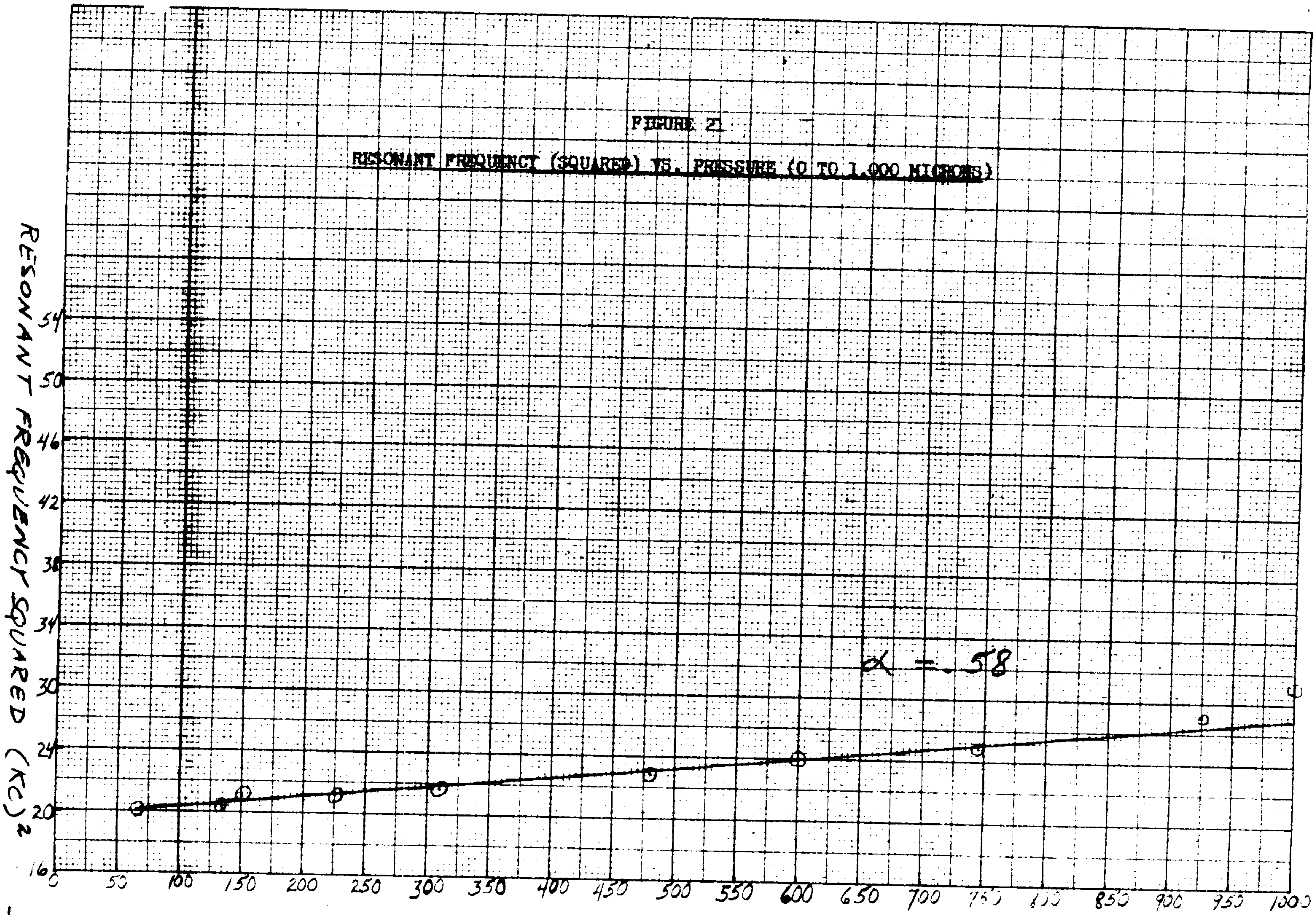

FIGURE 21

RESONANT FREQUENCY (SQUARED) VS. PRESSURE (0 TO 1,000 MICRONS)

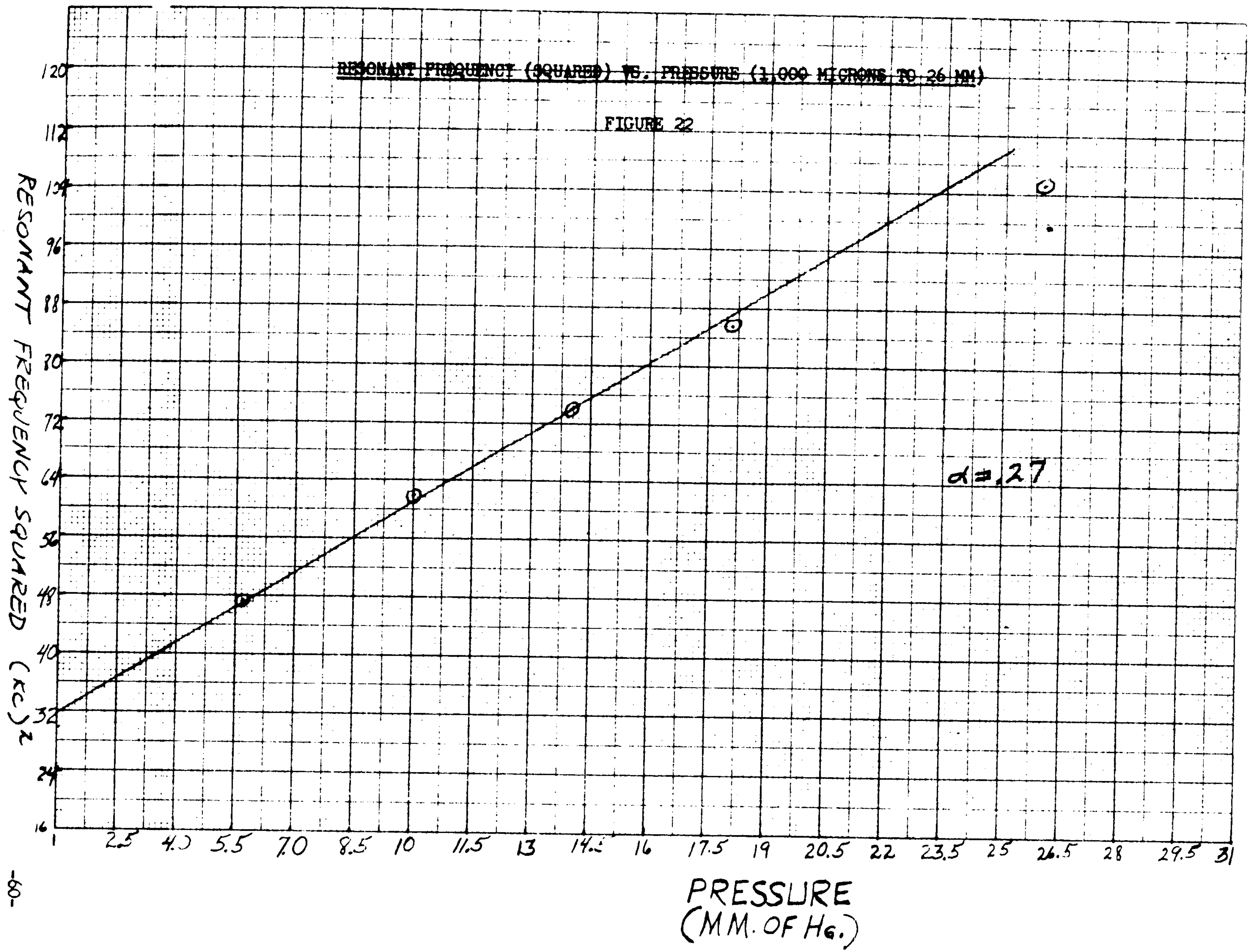

RESONANT FREQUENCY (SQUARED) VS. PRESSURE (1,000 MICRONS TO 26 MM)

FIGURE 22

SECTION 3

FABRICATION

FABRICATION OF MEMBRANES

The fabrication of aluminized, pre-tensioned membranes must be carefully controlled to insure uniformity of membrane characteristics and to provide optical quality surfaces. Special jigs and fixtures were designed to provide adequate control over all phases of the membrane fabrication process. This section of the report describes the membrane fabrication technique developed in Phase I and the special devices used in the process.

In summary, the process involves stretching sheet mylar on a 9-inch diameter stretching ring, designed to insure uniformity of tension and provide a means of adjusting the tension in very small increments to an empirically determined value. The stretched mylar is then transferred to a six-inch diameter ring aluminized and adjusted for maximum flatness. The aluminized membrane is finally transferred to a modulator unit.

The sheet mylar must first be inspected. Defects in the mylar can be located by visual inspection prior to stretching the mylar and an inspection of the stretched mylar with the use of crossed polarizers. The preselected mylar, (Dupont Type C Polyester Mylar Film), is placed in the 9-inch ring with minimal tension. See Figure 23 and 24. The ring and mylar are baked in air at 125°C for thirty minutes to remove the residual shrinkage and thus to stabilize the mylar. The 125°C temperature was chosen for this stabilization bake because the mylar will not be exposed to higher temperatures during fabrication or operation.

After the stabilization bake, the 9-inch ring and membrane are placed in the acoustic resonance setup to adjust the tension. This setup contains a variable frequency oscillator, amplifier, and a loudspeaker. The membrane is placed about two inches from the loudspeaker. The frequency of the oscillator is slowly increased from 10cps until the fundamental resonance of the membrane is reached. The fundamental resonance is unique in that it is the frequency where the center of the membrane has its largest amplitude of displacement. The opposing tension adjusting nuts (Figure 24) are slowly tightened, uniformly around the perimeter, until the resonant frequency exceeds a minimum of 100 cps. As the tension increases, the resonant frequency increases until the yield point is reached. The resonant frequency past the yield point decreases slightly with an increase in tension. The resonant frequency that corresponds to the yield tension varies from one membrane to another but is usually between 115 cps and 140 cps.

Those membranes which satisfy the resonant frequency criteria are transferred to the 6-inch I.D. membrane holding ring (Figure 25 and Figure 26). The 6-inch ring consists of three parts: the base ring, the clamping ring, and the o-ring flatness adjuster. The membrane in the 9-inch ring is placed on the clamping surface of the base ring and the clamping ring tightly screwed to the base ring with the flatness adjusting o-ring in place. The membrane is then cleaned and aluminized on both sides.

The membrane is aluminized on one side to form the optical mirror surface. Use of a front surface mirror is mandatory due to the poor transmission of the mylar. The opposite side is aluminized to form one of the two electrostatic surfaces and to improve the bond strength of the membrane to the modulator unit. (Epoxy to mylar bonds are quite weak and the mylar will peel easily from the cured epoxy.) Apparently the aluminum adheres strongly to the mylar and the epoxy adheres strongly to the aluminum, thus forming, in effect, a strong mylar-epoxy bond.

The main contaminant on the mylar, fresh from the roll, is an oily film. A strong detergent was therefore chosen as the first cleaning agent. Mylar accepts a reasonable amount of gentle rubbing with a surgical cotton ball saturated in a strong solution of Alconox and water without being scratched. The detergent can be removed by thoroughly rinsing the detergent-scrubbed mylar with hot (120° to 180°F) tap water. The membrane must be carefully dried to prevent water staining on the membrane.

The pressure in the vacuum chamber must be below 5×10^{-5} torr when aluminizing the membrane. If the pressure increases above 5×10^{-5} torr, the reflectivity of the resulting reflective membrane is usually unsatisfactory. The aluminized membrane's reflectivity is measured and the membrane is rejected if its reflectivity is below 80%. (Total reflectivity measured in the near-field.)

A special fixture was designed and built to allow the flatness of the aluminized membrane to be adjusted to the desired degree. This fixture (Figure 27 and Figure 28) consists of a stand to hold the 6-inch membrane holding ring and a partially aluminized optical flat. The 6-inch holding ring is fastened to its part of the fixture by Allen-head screws and then is attached firmly to the top part of the tripod legs. The optical flat is placed in the lower part of the tripod stand with the partially aluminized surface facing up. The optical flat is gently raised until the four adjusting screws are engaged in their respective tapped holes in the lower part. These adjusting screws are then used to adjust the membrane parallel to the optical flat until the desired interference fringe pattern is obtained. The membrane adjusting set screws in the 6-inch ring are adjusted so that the membrane is as flat as possible over the central area. The mylar membrane is now ready to be cemented to the modulator structure.

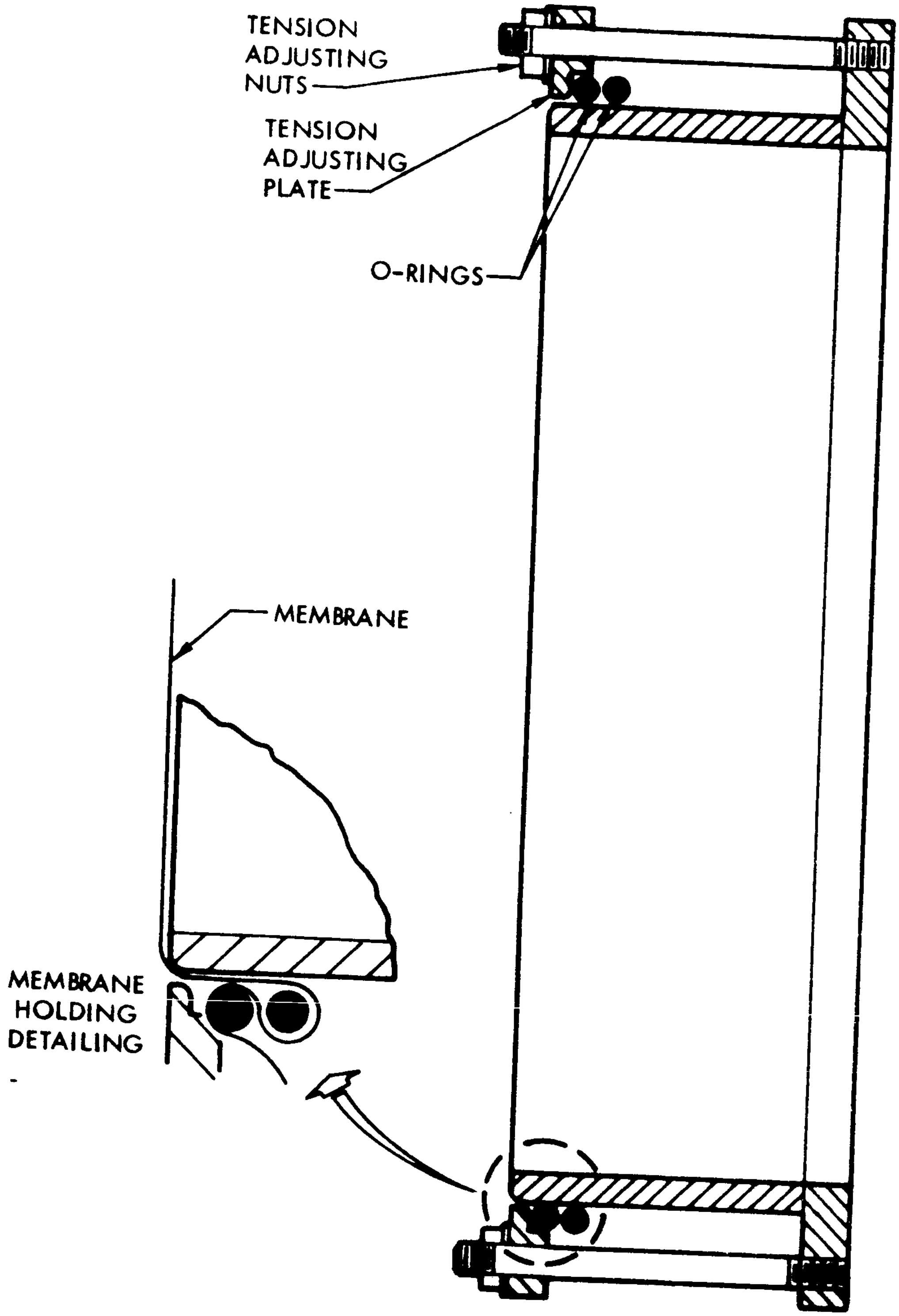

Figure 23. Mylar Stretching Ring, 9-inch I. D.

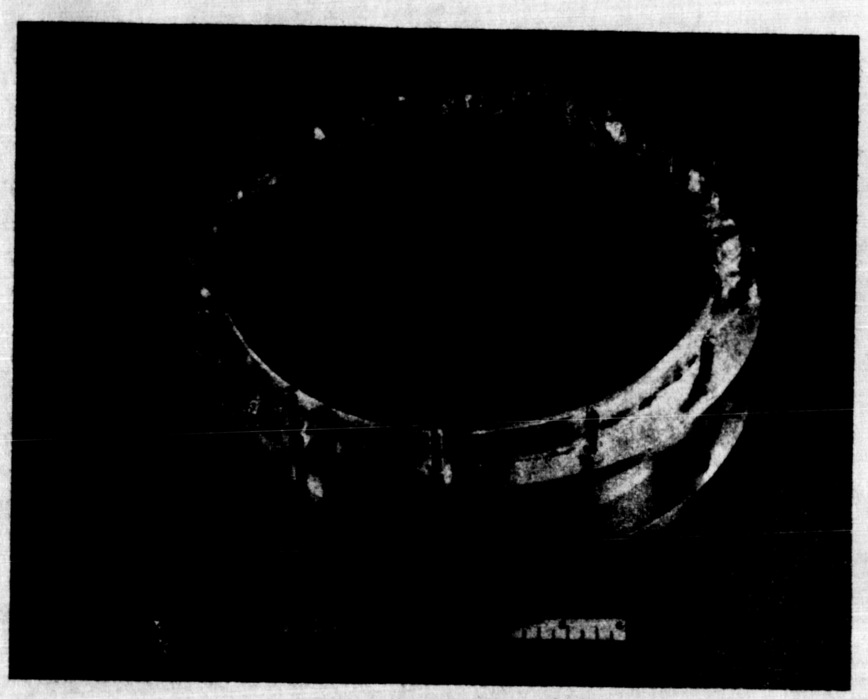

Figure 24. 9-inch I. D. Stretching Ring

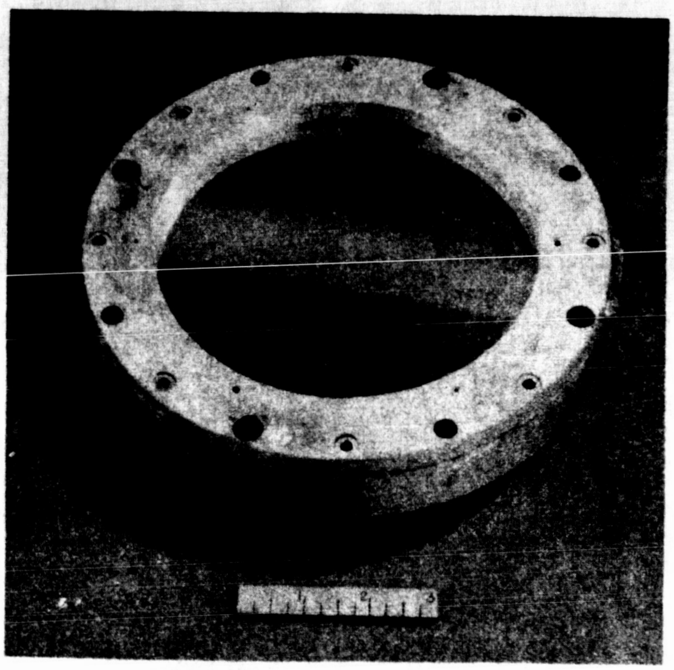

Figure 25. 6-inch I. D. Holding Ring

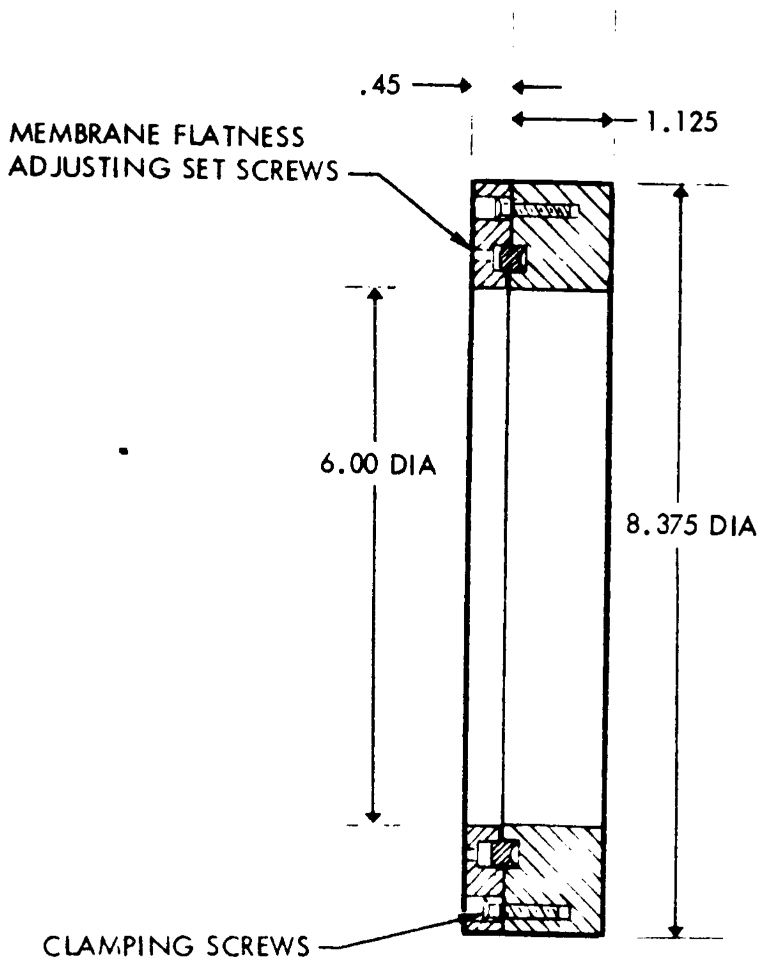

Figure 26. Membrane Holder, 6-inch I. D.

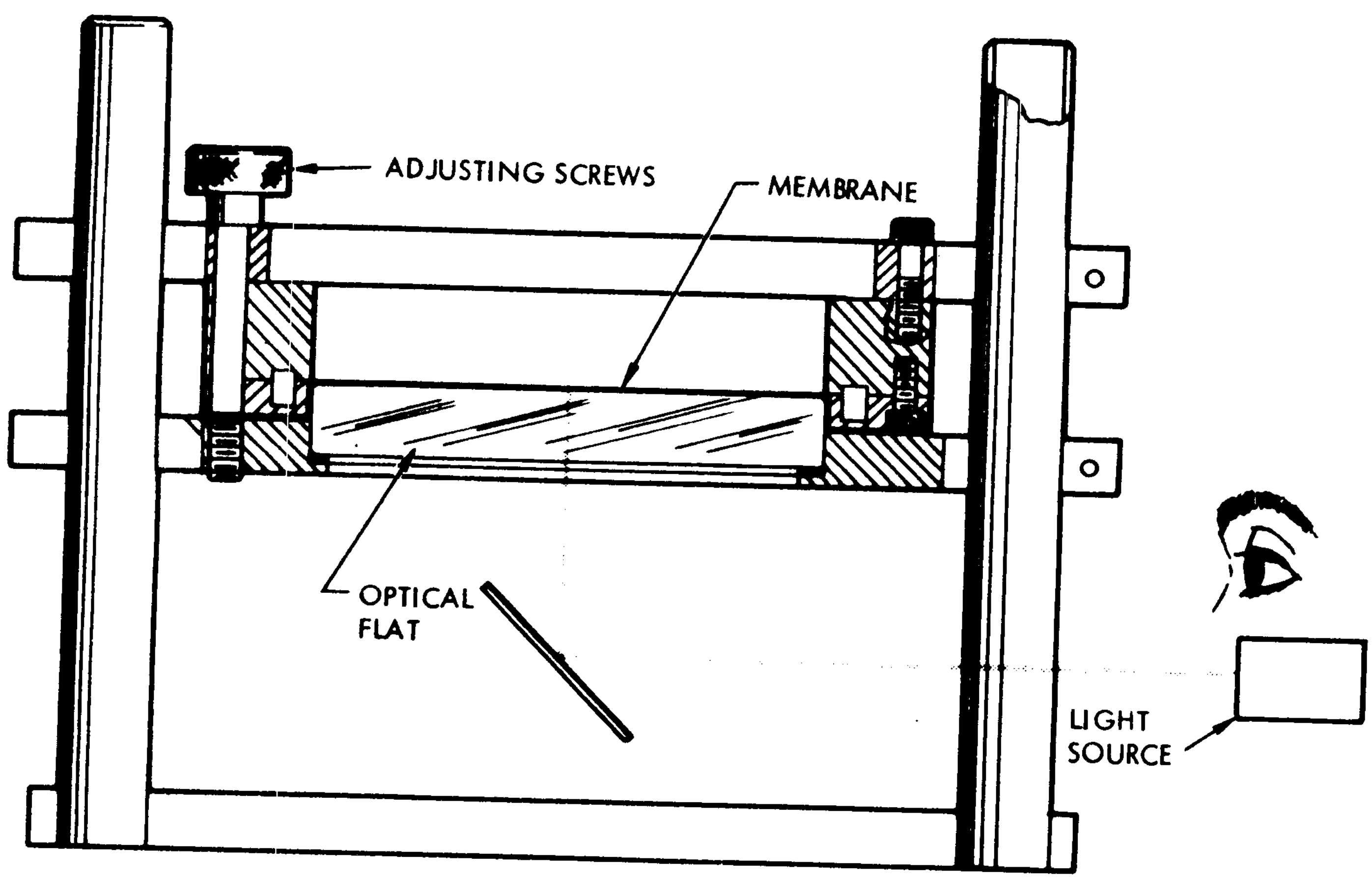

Figure 27. Coated Mylar Flatness Measurement Instrument

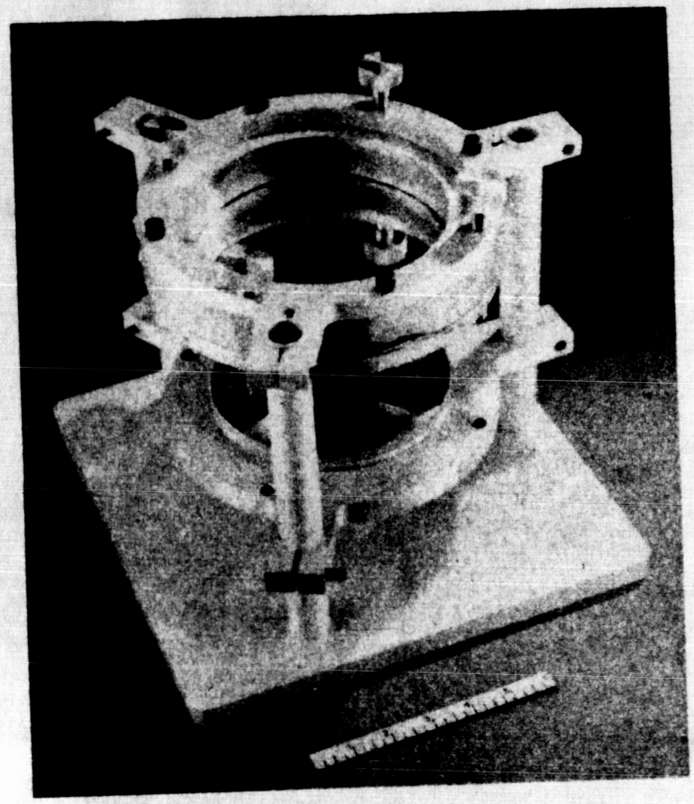

Figure 28. Membrane Flatness Testing Assembly

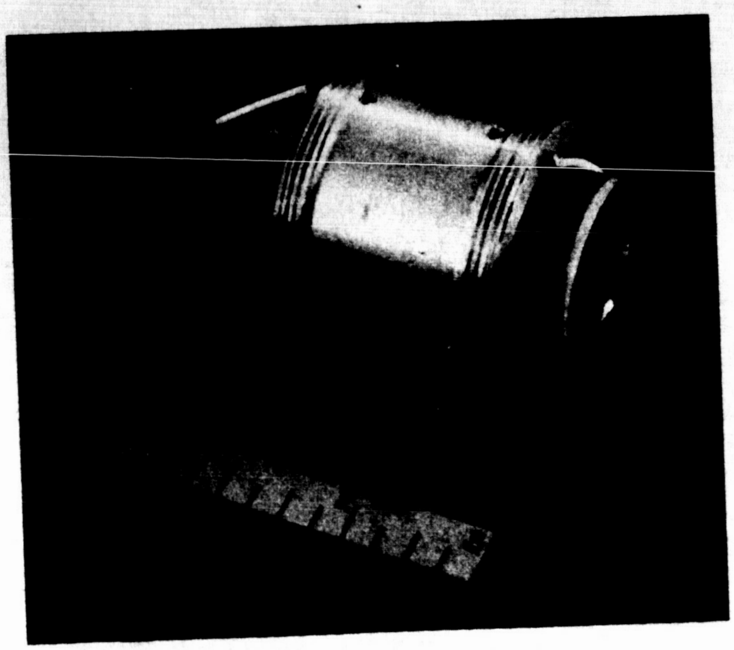

Figure 29. Piston-Type Test Modulator in Holder, Without End Caps

FABRICATION OF ELECTROSTATIC MODULATOR UNITS

Two types of electrostatic modulators have been designed. The piston-type modulator, see Figure 30, and Figure 31, consists of a cylinder which supports the aluminized membrane and the piston which can be moved to adjust the electrostatic gap to the desired value. The Chem-milled modulator consists of a quartz disc with a pressure-relief, electrical connection, a chemically milled gap, and a ridge which supports the membrane, see Figure 8 and Figure 37.

Piston-Type Modulator Units:

The quartz cylinder and piston are fabricated by West Coast Optical Company, Los Angeles, California. After receipt by N.A. A., the piston is cleaned and the conductive lead attached to the pressure-relief groove with conductive epoxy. The piston is then aluminized so that a conductive coating is formed on the flat face and a conductive bridge formed to the conductive epoxy in the groove.

The cylinder is cleaned and placed face down on the flat aluminized membrane supported by an optical flat. (Note: The membrane is held in tension on a 6-inch ring.) A weight is placed on the cylinder to hold the cylinder in place during the epoxy application. The epoxy is extruded from a plastic syringe into the chamferred groove formed by the membrane and the cylinder edge, (Figure 32). After the epoxy cures, the membrane is cut from the 6-inch ring and trimmed so that a tab of the membrane is left for the attachment of a gold wire lead. This lead is attached to the aluminized side of the membrane closest to the face of the inserted piston.

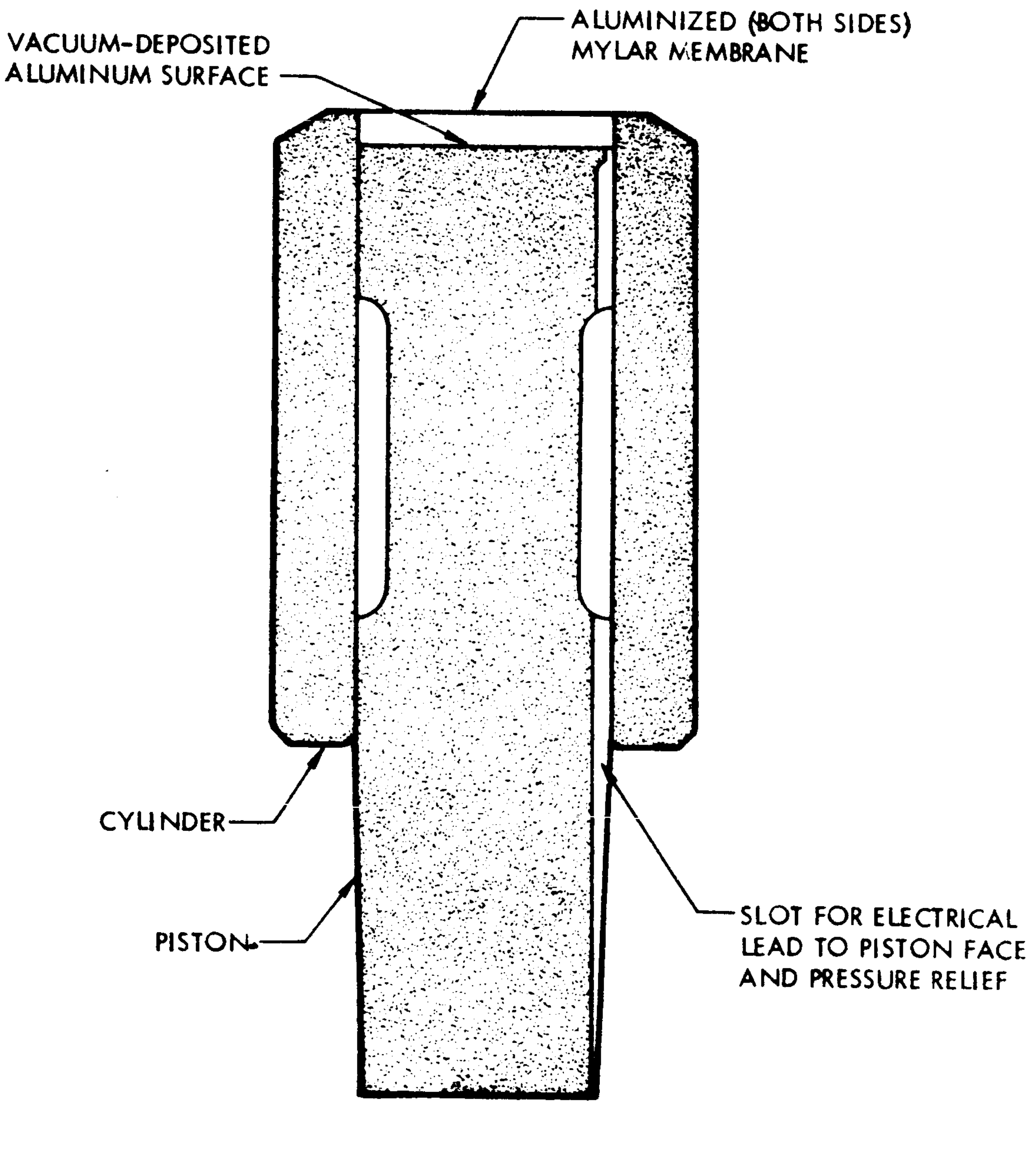

Figure 30. Sectional View of Piston-Type Modulator

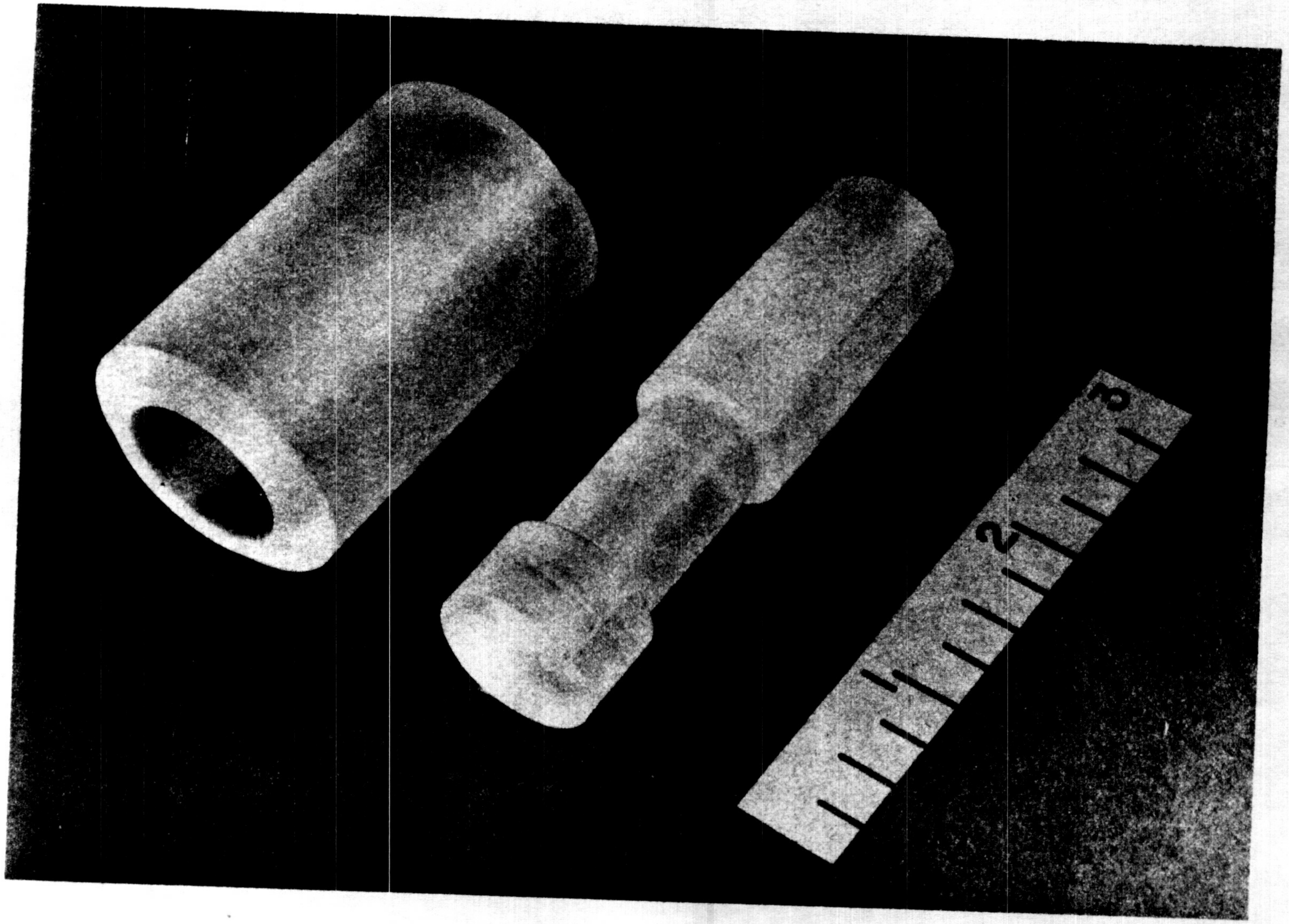

Figure 31. Piston and Cylinder, Piston-type Modulator

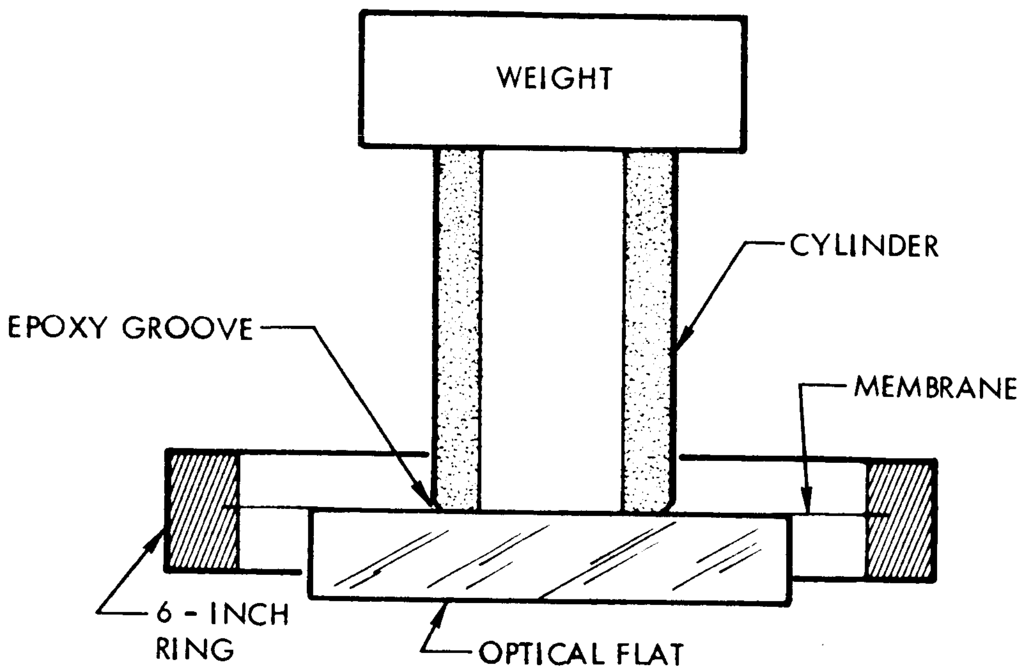

Figure 32. Configuration for Bonding Membrane to Cylinder

The prepared cylinder is mounted in the center part of the protective holder, Figure 29. The protective holder also serves as a mount for the piston modulator. The piston is coated with a light film of silicone grease and inserted part way into the mounted cylinder. The cylinder-piston pair is attached to the gap adjustment fixture, Figure 33, and the membrane to piston-face gap adjusted with the micrometer. The capacitance of the piston modulator can be calculated for any desired gap in accordance with the equation given below.

$$C = \frac{E_o A}{d}$$

where

C = Capacitance in farads.

E_o = 8.85×10^{-12} farads per meter

A = Area of one plate in square meters

d = Gap distance between plates in meters.

The piston-modulator gap is then easily adjusted to the calculated capacitance with the use of a capacitance bridge. After the gap is properly adjusted, the piston-cylinder pair are sealed together by a few drops of epoxy. The same type epoxy used for bonding the membrane to the cylinder causes a 5% change in gap distance.

During testing of the first and second piston modulators, a ring of aberrations appeared in the membrane. The aberrations coincided with the location of the inside lip of the cylinder face and appeared as if they had been formed by irregularities on that edge. The third cylinder, prior to attaching the membrane, was lightly polished on the inner lip and a micro-chamfer formed. In the subsequent testing of the third piston-modulator, the ring of aberrations did not develop.

Figure 33. Gapping Fixture for Piston-Type Test Modulator

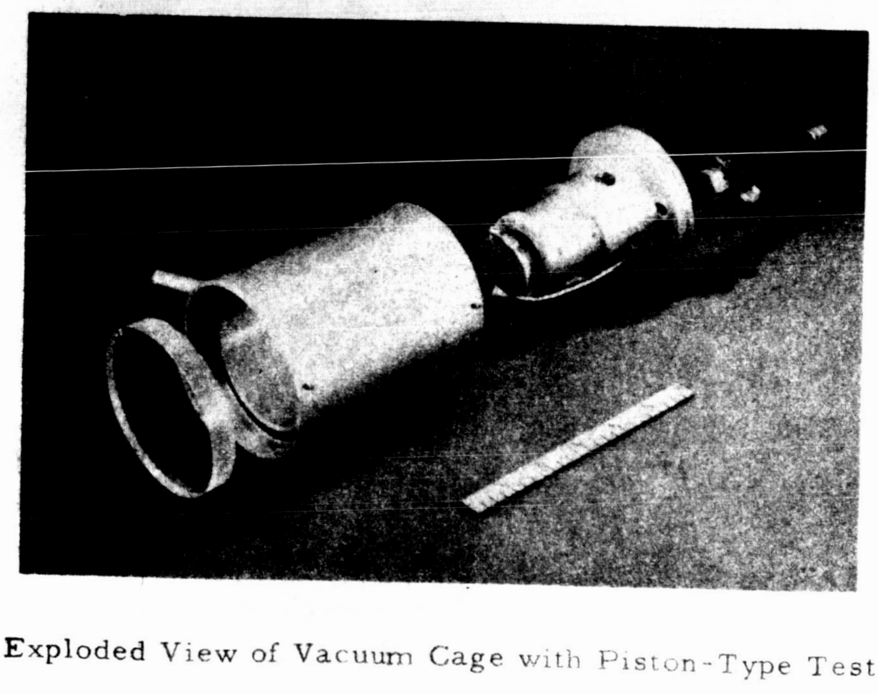

Figure 34. Exploded View of Vacuum Cage with Piston-Type Test Modulator

Chem-milled Modulator Units:

The Chem-milled modulator consists of a reflective aluminized mylar membrane, a specially fabricated quartz element, and a nickel pressure-relief tube. The membrane fabrication is discussed in a previous section. The quartz piece is machined and polished by an optical component subcontractor prior to being Chem-milled* by the Autonetics Division of North American Aviation. Final assembly is done by the Electro-Optical Laboratory of N. A. A.

The quartz piece is machined to a disc-shape with the two sides of the disc flat and parallel to each other. A hole for the pressure relief tube is ground through the axis of the disc and a chamfer is put on the front edge of the hole. The front edge of the quartz disc is ground to produce a ledge for the epoxy-membrane bond (Figure 35).

The machined and polished blanks are acceptance tested by the Autonetics Division of N. A. A. Accepted blanks are cleaned and a photo-mask applied to the areas which are not to be chemically etched. The blank is mounted in an etching holder. The etching holder is specifically designed for this task. The Chem-milling process is performed at a slow rate to preserve the etched surface's optical polish and its parallelism with the back surface. The Chem-milled surface of the modulator blank is tested for flatness and parallelism with the back surface. The masking material is then removed.

The Chem-milled surface is cleaned, placed in a mechanical masking frame and a thin film of aluminum vacuum deposited (Figure 36) to form one plate of the electrostatic modulator.

* Chem-milling is a proprietary process developed by North American Aviation, Incorporated.

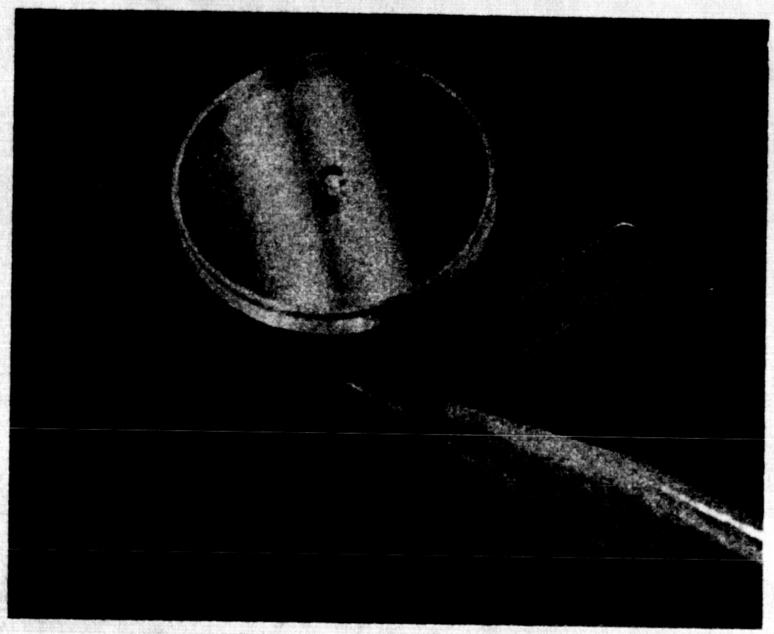

Figure 35. Quartz Blank, Chem-milled Modulator, Prior to Chem-milling Operation. (Machined as per Figure 8A)

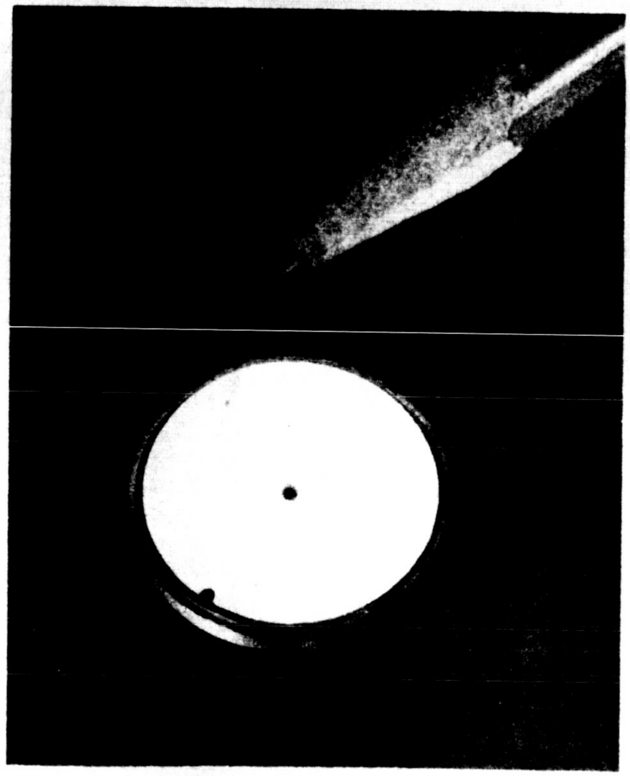

Figure 36. Chem-milled Modulator Blank, with Aluminized Chem-milled Inner Surface. (Processed as per Figure 8B)

The aluminized and Chem-milled modulator blank is inspected and cleaned. A nickel tube is fastened into the pressure relief hole with conductive epoxy, (Figure 37). The tube makes electrical connection to the aluminized surface of the modulator blank and also acts as a pressure relief. An aluminized membrane in a 6-inch ring is bonded to the finished modulator blank with epoxy.

After the epoxy has been cured, the membrane is cut away from the 6-inch holding ring. The excess mylar is trimmed off around the edge of the modulator unit except for small tabs left for electrical connection to the back surface of the membrane. A .005-inch diameter gold lead wire is cemented to the outer edge of one of the tabs with conductive epoxy. (This lead is used during test of the unit and is removed by clipping off the edge of the tab prior to installation of the modulator unit in a cube corner reflector.)

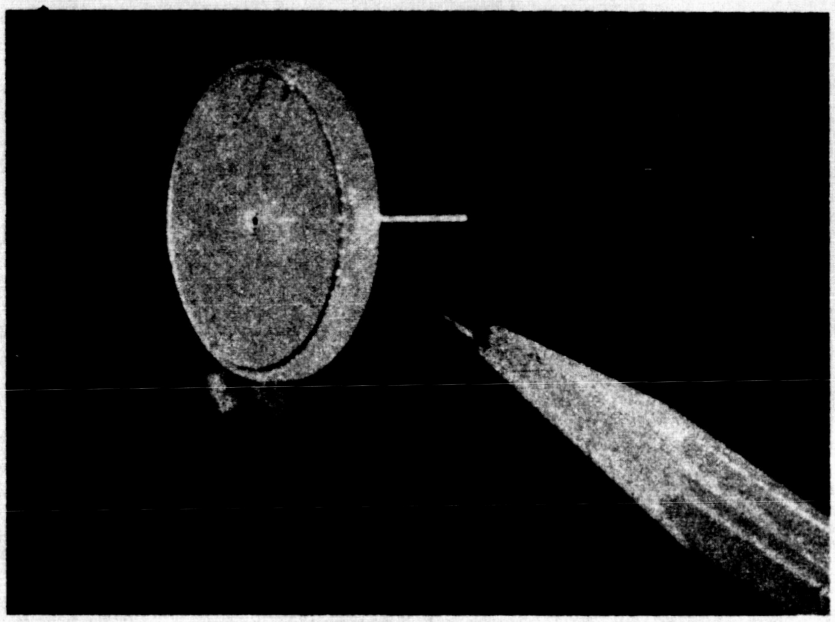

Figure 37. Chem-milled Aluminized Blank with Conductive Pressure-relief Tube. (Membrane Not in Place)

FABRICATION OF VACUUM CHAMBER

The vacuum chamber is designed to provide the desired vacuum or partial pressure of gas during the testing of either the piston-type or chem-milled type modulator. It consists of an optically flat Vycor window, a cylindrical housing, a modulator-supporting base and a valve. The Vycor window is polished optically flat. The window and base are sealed to the cylindrical housing with Viton o-rings. As the chamber is evacuated by the vacuum pump, the air pressure forces the base and window against the o-rings thus forming pressure seals. The modulator-supporting base has a threaded stud onto which the bottom end cap of the piston modulator is screwed. The vacuum chamber maintains a pressure of 50μ while being pumped by the vacuum pump. Its leak rate, when not being pumped, allows the pressure to rise from $50\,\mu$ to $1000\,\mu$ in approximately 15 hours. See Figure 34 for exploded view of vacuum chamber with piston-type modulator. Figure 34a shows the vacuum chamber in use testing a piston-type modulator.

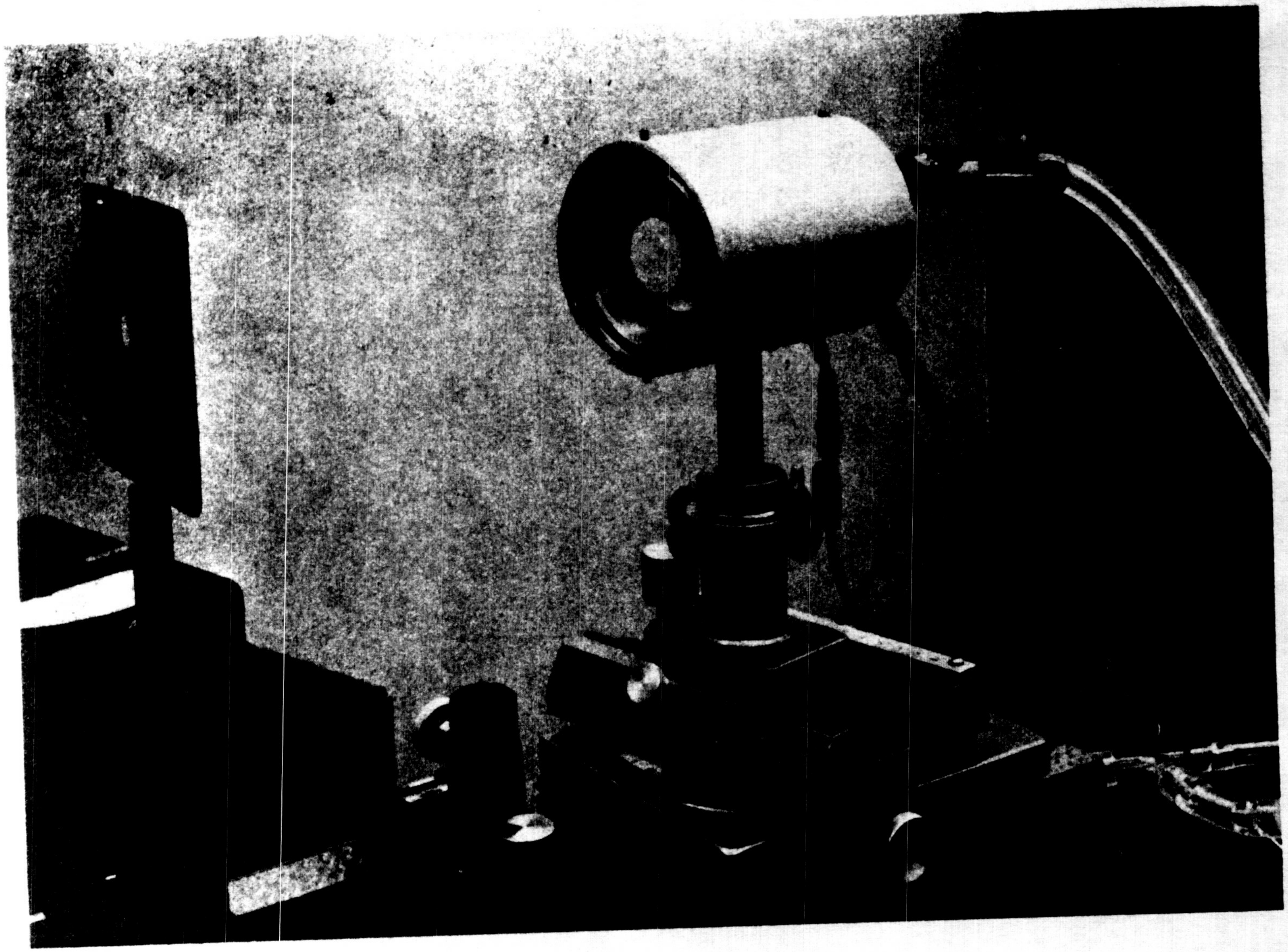

Figure 34a Piston-type Modulator in Vacuum Chamber

SECTION 4

TEST PROGRAM REPORT

MEASUREMENTS ON PROPERTIES OF MYLAR

The manufacturer's catalog values are typical performance data and are not intended to be used as design data.

A series of experiments was performed to provide design data. The following physical properties of commercial grade Mylar were measured using material rolls on hand:

(1) Thickness

(2) Density

(3) Yield Strength

(4) Young's Modulus

Thickness was measured with a high precision dial indicator.

Density was determined by weighing samples of measured dimensions on a precision balance.

Yield stress was determined by loading a mylar strip of measured dimensions and measuring elongation.

Young's Modulus was determined from the slope of the experimentally determined stress-strain curve.

Test Results - Type C Mylar:

Property	Catalog Value	Measured Value
Thickness	0.25×10^{-3} in.	$0.25 \pm .02 \times 10^{-3}$ in.
Density	1.395 gm/cc	1.29 gm/cc
Yield Stress	Approx. 16,000 lb/in^2 (25°C)	Approx. 9,500 lb/in^2 (25°C)
Young's Modulus	550,000 lb/in^2	535,000 lb/in^2

Observations and Conclusions:

The samples tested exhibited "creep" under load at stresses approaching the yield point stress. A test was performed to measure the creep rate at 90% of yield point stress. The results are plotted as Figure 38. In a second test with the sample loaded at 30% of measured yield point stress there was no measurable creep over an interval of 22.5 hours.

Difficulty was encountered in establishing uniform loading across the strip as evidenced by strain lines in the strips under load.

This most probably accounts for the difference in the catalog yield point and the measured yield points which are approximately 60% of catalog values. Measured thickness, density, and Young's Modulus are in good agreement with the manufacturer's data.

TYPE C MYLAR
2.5 X10^{-4} IN. THICKNESS

FIGURE 38

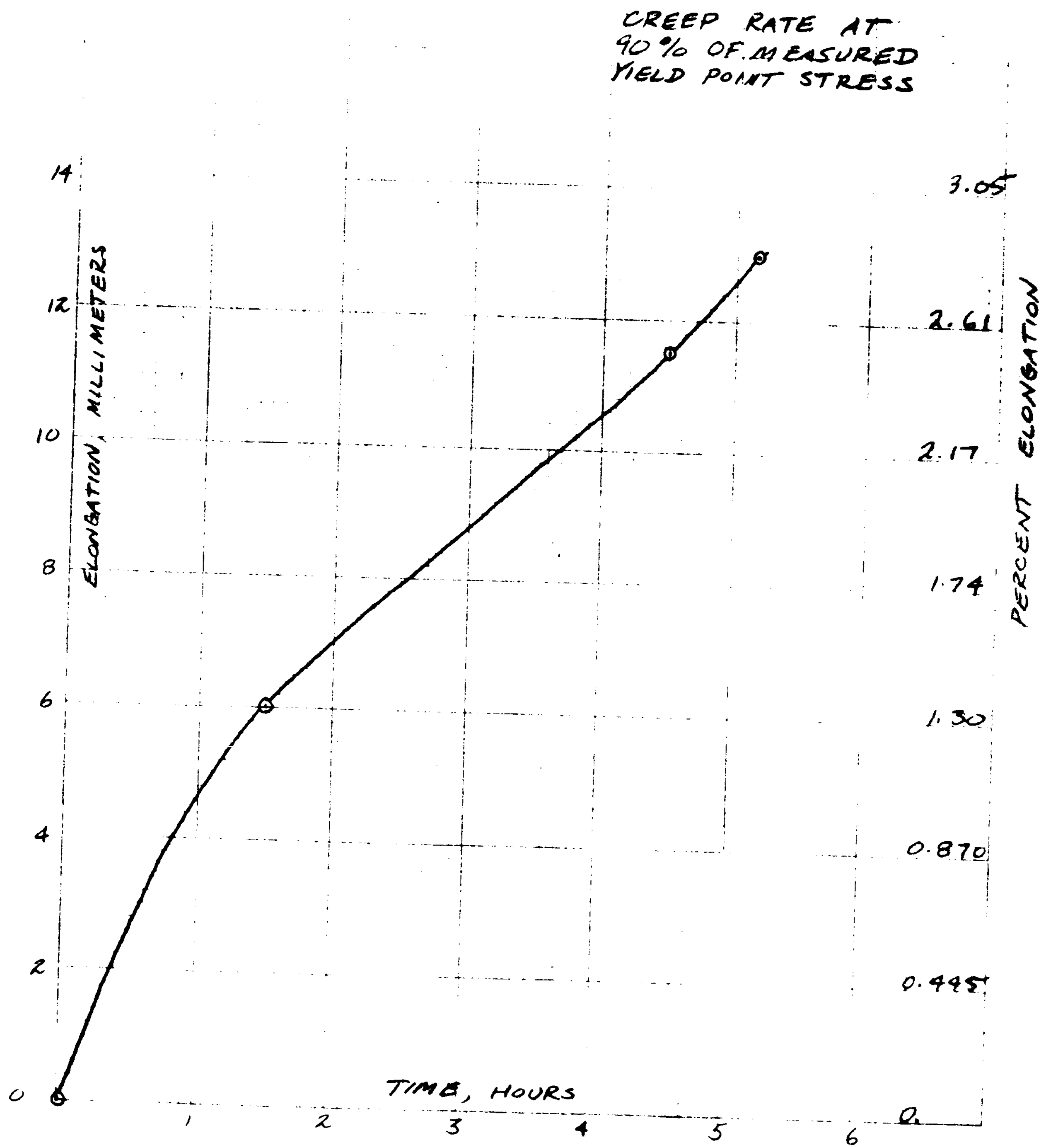

MEASUREMENTS OF ELECTROSTATIC MODULATOR UNIT MEMBRANE FLATNESS

Each of the three piston-type modulators fabricated was tested to determine the flatness of the modulatable membrane.

A piston modulator was inserted as the end mirror in one leg of a Michelson Interferometer. The light source wavelength used was 5893 Angstrom, (Sodium D line). The resultant interference fringe pattern was photographed. Figure 39 is a photograph of the second unit fabricated. The circle designates the 2 cm diameter active area. The fringe interval is 1/2 wavelength and the average flatness across the 2 cm diameter is of the order of 1/2 wavelength at 5893 Angstrom. Figure 40 is a photograph of the third unit fabricated and also indicates a flatness of the order of 1/2 wavelength across the 2 cm active diameter. The edge irregularity of the fringes in Figure 40 further indicates that the roughness or short-term irregularities are also of the order of 1/2 wavelength. (The cylinder surface over which the membrane is stretched is ground to better than 1/5 wave flatness.)

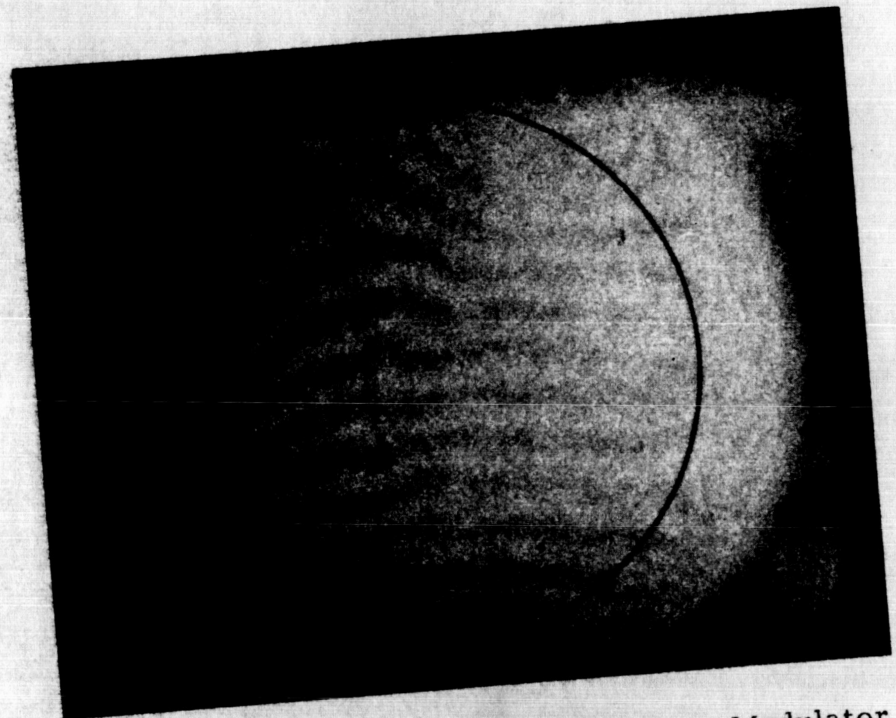

Figure 39. Interference Pattern from Piston-Type Modulator No. 3

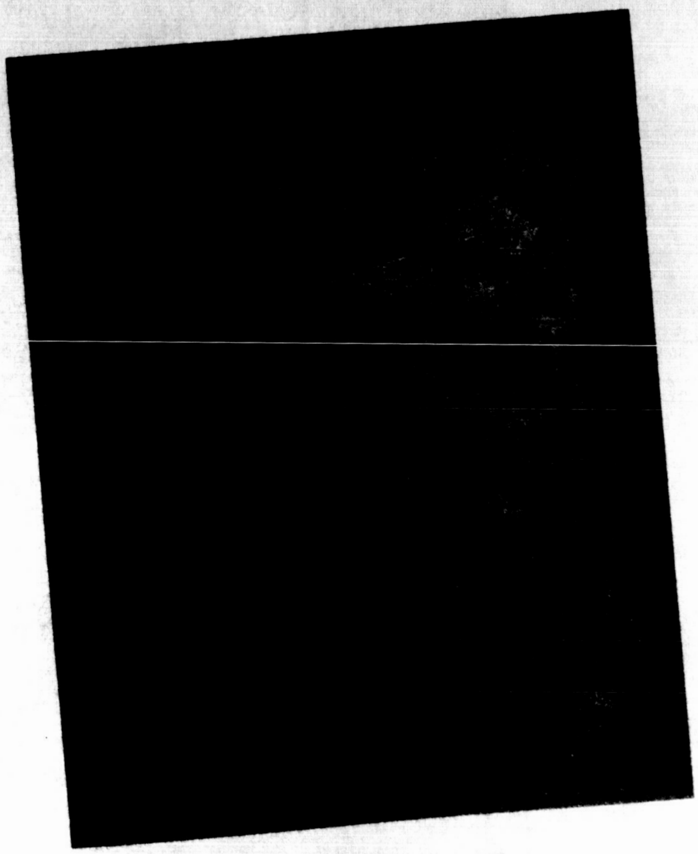

Figure 40. Interference Pattern from Piston-Type Modulator No. 2

MEASUREMENTS OF ELECTROSTATIC MODULATOR UNIT MEMBRANE TENSION AND DEFLECTION

Device Tested:

Piston-type Modulators, Nos. 1 and 3.

Purpose of Test:

1. To determine the sagittal deflection characteristics of the membrane as a function of applied DC voltage.
2. To determine the tension in the membrane by a technique not dependent on the resonant frequency equation for the membrane.

Method Used:

A DC voltage was applied to the modulator unit and the sagittal deflection of the membrane was measured by observing the interference fringe shift at the geometric center of the membrane. Interference fringes were obtained by using an interference microscope and a Thallium (5350Å) light source for the first test on Modulator No. 1. The second test on Modulator No. 1 and the test on Modulator No. 3 were performed with a Michelson interferometer and a 5893 Angstrom light source (Sodium D line).

Results of Test:

See Figures 41, 42, and 43.

Observations and Conclusions:

From Equation (V)*

$$\Delta = \frac{a^2 \; E_0}{8t\alpha \; T_m \; d^2} V^2 \tag{V}$$

* Electrostatic Modulator Unit Design Section.

sagittal deflection is seen to be of the form

$$\Delta = K_d V^2$$

where K_d is a deflection constant

$$K_d = \frac{a^2 E_0}{8\tau\alpha T_m d^2}$$

Figures 41, 42, and 43, indicate that both units follow the square law deflection characteristic quite well out to one wavelength deflection (for λ = 6,328Å). K_d is selected to give the best fit to the experimental data.

Rearranging Equation (V), to find the tension:

$$\text{Tension} = \alpha T_m = \frac{a^2 E_0}{8\tau d^2}\left(\frac{V^2}{\Delta}\right)$$

$$\text{but} \quad \left(\frac{V^2}{\Delta}\right) = \frac{1}{K_d}$$

Where K_d = deflection constant and $d = \dfrac{E_0 \pi a^2}{C}$ where C = Capacitance.

Therefore

$$\alpha T_m = \frac{C^2}{8\pi^2 E_0 K_d \tau a^2}$$

Modulator No. 1 was fabricated from a 6.00 inch diameter aluminized mylar membrane that exhibited an acoustic resonance at 308 cps. in air at 25°C.

A 5.75 inch diameter membrane was tested and found to have a 320 cps. resonance under the same conditions. The 5.75 inch diameter membrane was then tested by a water-loading method. The tension was determined to be 5,640 lb/in^2. Correcting for the small differences in resonant frequency and diameter, the estimated tension in the membrane used to fabricate Modulator No. 1 was

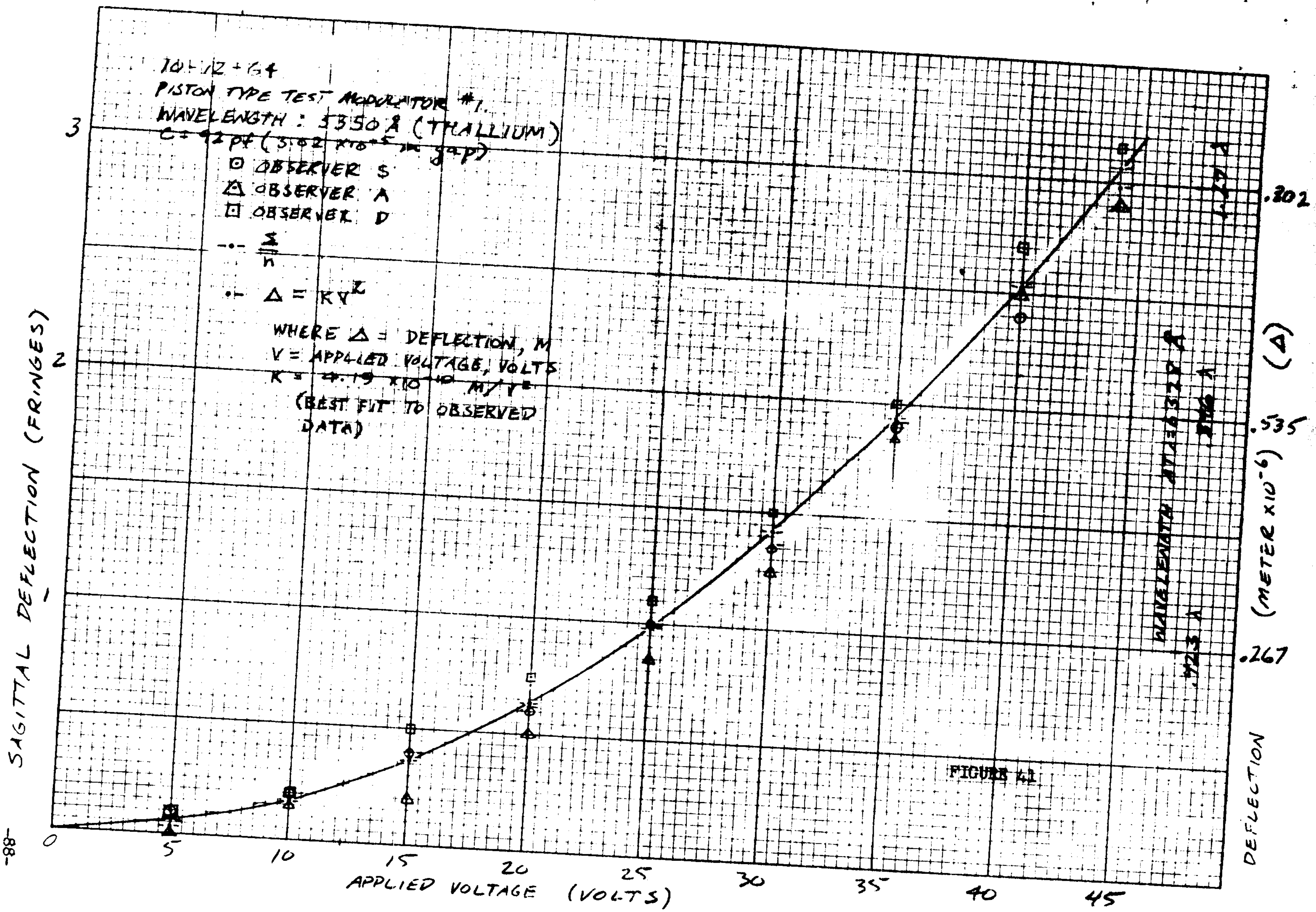

10-12-64
PISTON TYPE TEST MODULATOR #1.
WAVELENGTH : 5350 Å (THALLIUM)
OBSERVER S
OBSERVER A
OBSERVER D
Δ = KV²
WHERE Δ = DEFLECTION, M
V = APPLIED VOLTAGE, VOLTS
(BEST FIT TO OBSERVED DATA)
SAGITTAL DEFLECTION (FRINGES)
APPLIED VOLTAGE (VOLTS)
0
5
10
15
20
25
30
35
40
45
1
2
3
.267
.535
.802
(METER x10⁻⁶)
(Δ)
DEFLECTION

FIGURE 41

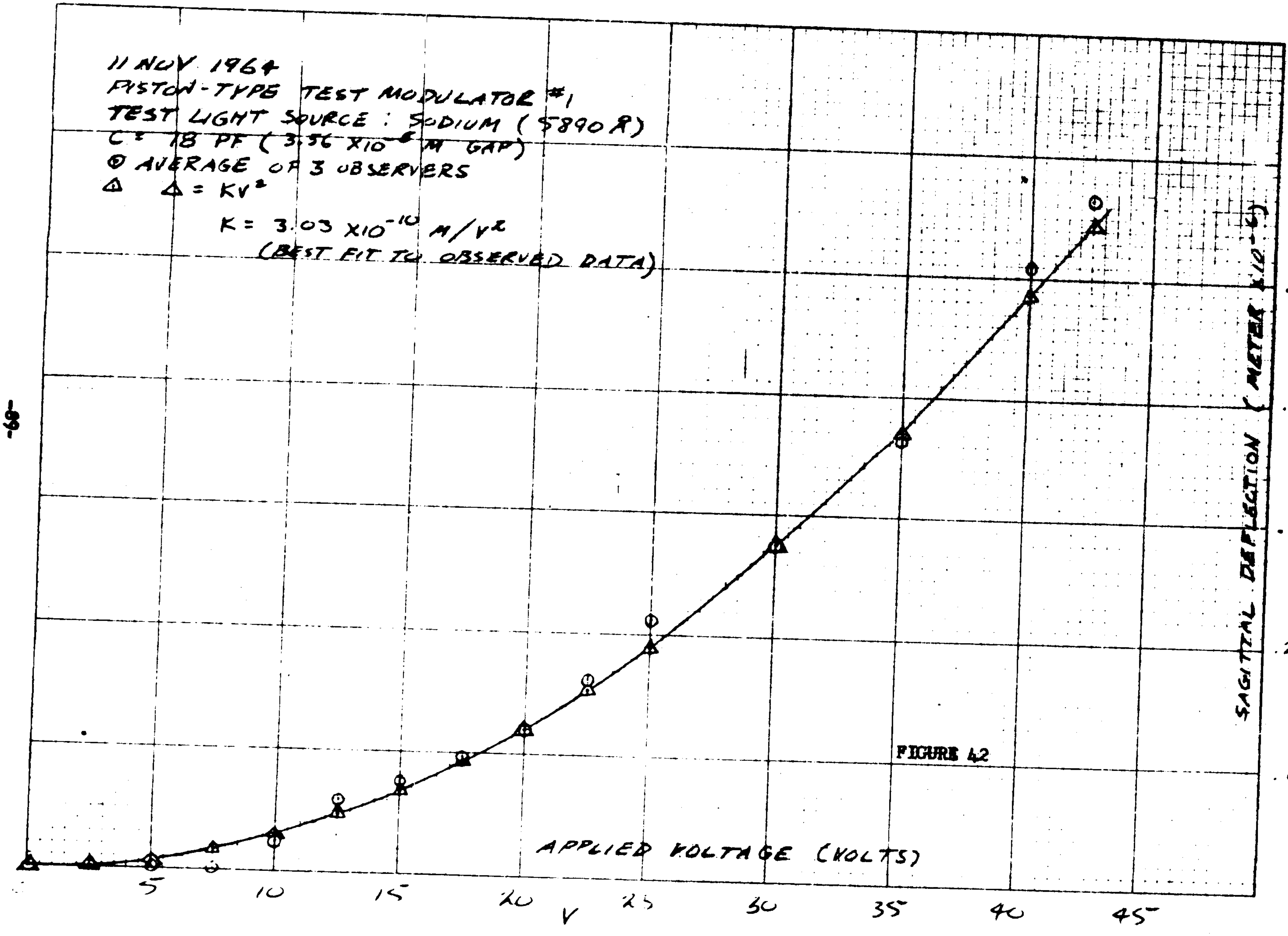
11 NOV 1964
PISTON-TYPE TEST MODULATOR #1
TEST LIGHT SOURCE : SODIUM (5890 Å)
C = 18 PF (3.56 X10⁻⁶ M GAP)
⊙ AVERAGE OF 3 OBSERVERS
△ △ = KV²
K = 3.03 X10⁻¹⁰ M/V²
(BEST FIT TO OBSERVED DATA)
APPLIED VOLTAGE (VOLTS)
V
SAGITTAL DEFLECTION (METER X10⁻⁶)
△
5
10
15
20
25
30
35
40
45
.1
.2
.3
.4
.6
FIGURE 42

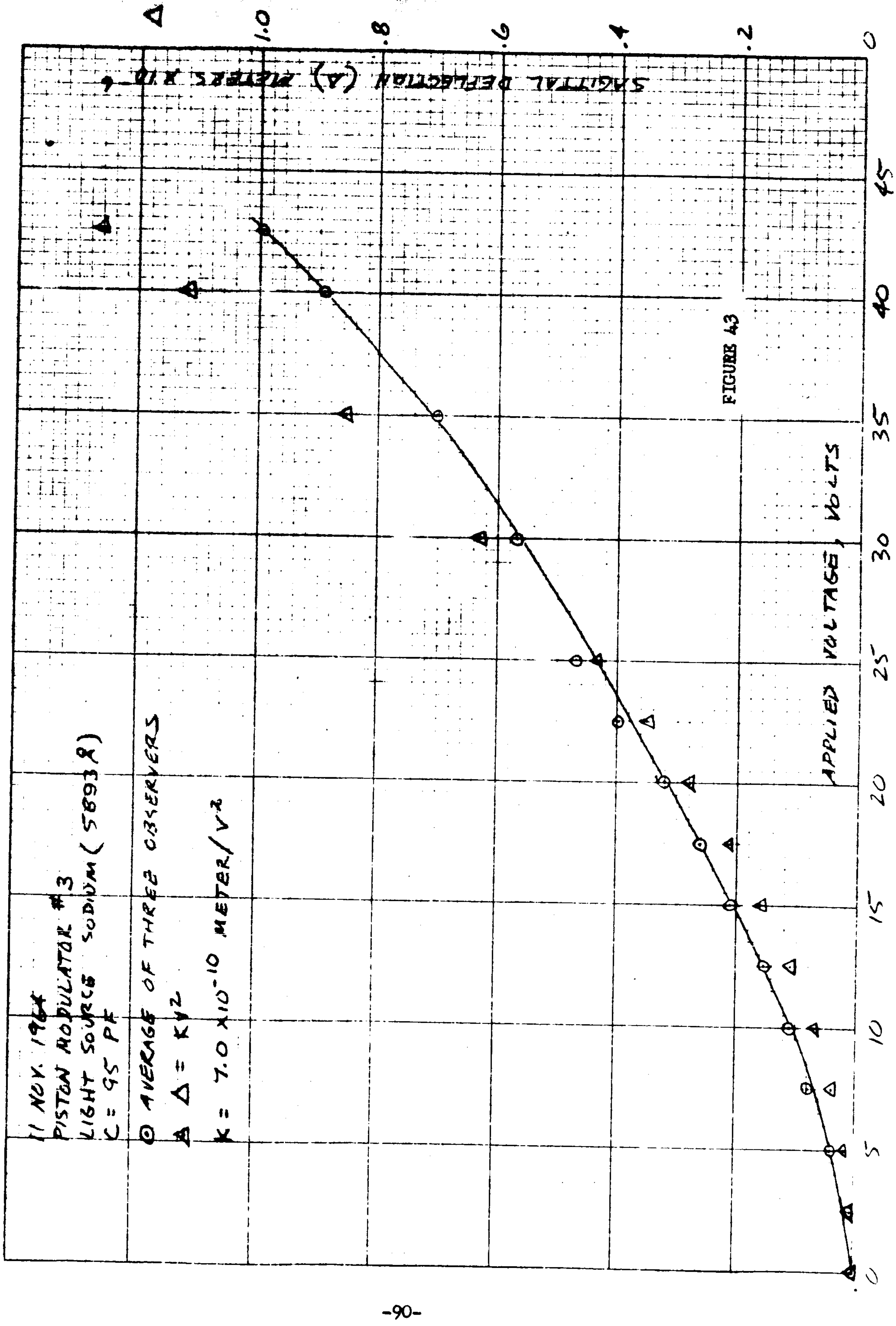

11 NOV. 1964
PISTON MODULATOR #3
LIGHT SOURCE SODIUM (5893 Å)
C = 95 PF
⊙ AVERAGE OF THREE OBSERVERS
Δ Δ = KV²
K = 7.0 X10⁻¹⁰ METER/V²
SAGITTAL DEFLECTION (Δ) METERS X10⁻⁶
APPLIED VOLTAGE, VOLTS
0 .2 .4 .6 .8 1.0 Δ
0 5 10 15 20 25 30 35 40 45

FIGURE 43

$$\frac{(308)^2}{(320)} \; (5{,}640 \text{ lb/in}^2) \; \frac{(6.00)}{(5.75)} = 5{,}470 \text{ lb/in}^2$$

which is approximately one-third the manufacturer's value for yield point tension at 25°C.

This is 12 to 17 percent greater than the tension values measured by electrostatic deflection. (See Table 6 for membrane tension after transfer of membrane to modulator.)

Values of tension obtained for Modulator No. 1 with two different test setups and two different gap settings agree within six percent.

TABLE 6

MEMBRANE DEFLECTION AND TENSION MEASUREMENTS FOR PISTON-TYPE MODULATOR

Piston-Type Modulator	Membrane Thickness (Meters) (t)	Membrane Diameter (Meters) (2a)	Measured Deflection Constant (Meter/Volt^2) (K_d)	Measured Capacitance (Farad) (C)	Computed Tension (Newton/Meter^2) $\sigma T_m = \frac{C^2}{8\pi^2 \epsilon_o K_d t a^2}$ (σT_m)
#1 - (First Test)	6.35×10^{-6}	2.00×10^{-2}	4.3×10^{-10}	$92. \times 10^{-12}$	4.52×10^{7} (=6,550 lb/in^2)
#1- (Second Test)	6.35×10^{-6}	2.00×10^{-2}	2.85×10^{-10}	$78. \times 10^{-12}$	4.81×10^{7} (= 6,970 lb/in^2)
#3-	6.35×10^{-6}	2.00×10^{-2}	7.0×10^{-10}	$95. \times 10^{-12}$	2.91×10^{7} (= 4,220 lb/in^2)

NOTES: (1) A test was run on Piston-Type Modulator #1 for each of the two different gap settings (d).

MEASUREMENTS OF ELECTROSTATIC MODULATOR UNIT
D.C. TRANSFER FUNCTION

The D.C. transfer function of an electrostatic modulator was measured during Phase I of the MIROS Program. This transfer function defines the relationship between the applied DC voltage on the modulator and the radiant intensity at a point in the far-field pattern of light reflected from the modulating surface.

A DC voltage is applied between the back aluminized surface of the membrane and the aluminized face of the piston (See Figure 30) causing the membrane to deform as described in Section 1. The front surface of the membrane is illuminated with collimated light. The energy reflected from the membrane is collected and brought to a focus by a lens. A pinhole is placed in the focal plane of the lens as established by the undeflected membrane. The pinhole is adjusted to be centered on the Airy disc. (The pinhole diameter is made slightly smaller than the diffraction-limited spot size produced by the lens when illuminated by collimated light.) A photomultiplier is placed behind the pinhole to measure relative intensity in this simulated far-field environment.

Given the D.C. transfer function for the device, the following parameters can be determined (for operation below the first resonance):

(1) Optimum Bias Voltage for Different Modes of Operation

(2) Dynamic Range and Linearity

(3) Achievable Depth of Modulation

(4) Driving Voltage Required to Produce a Given Depth of Modulation

The devices tested were Piston-Type Modulators Nos. 1 and 2. (See Table 7.)

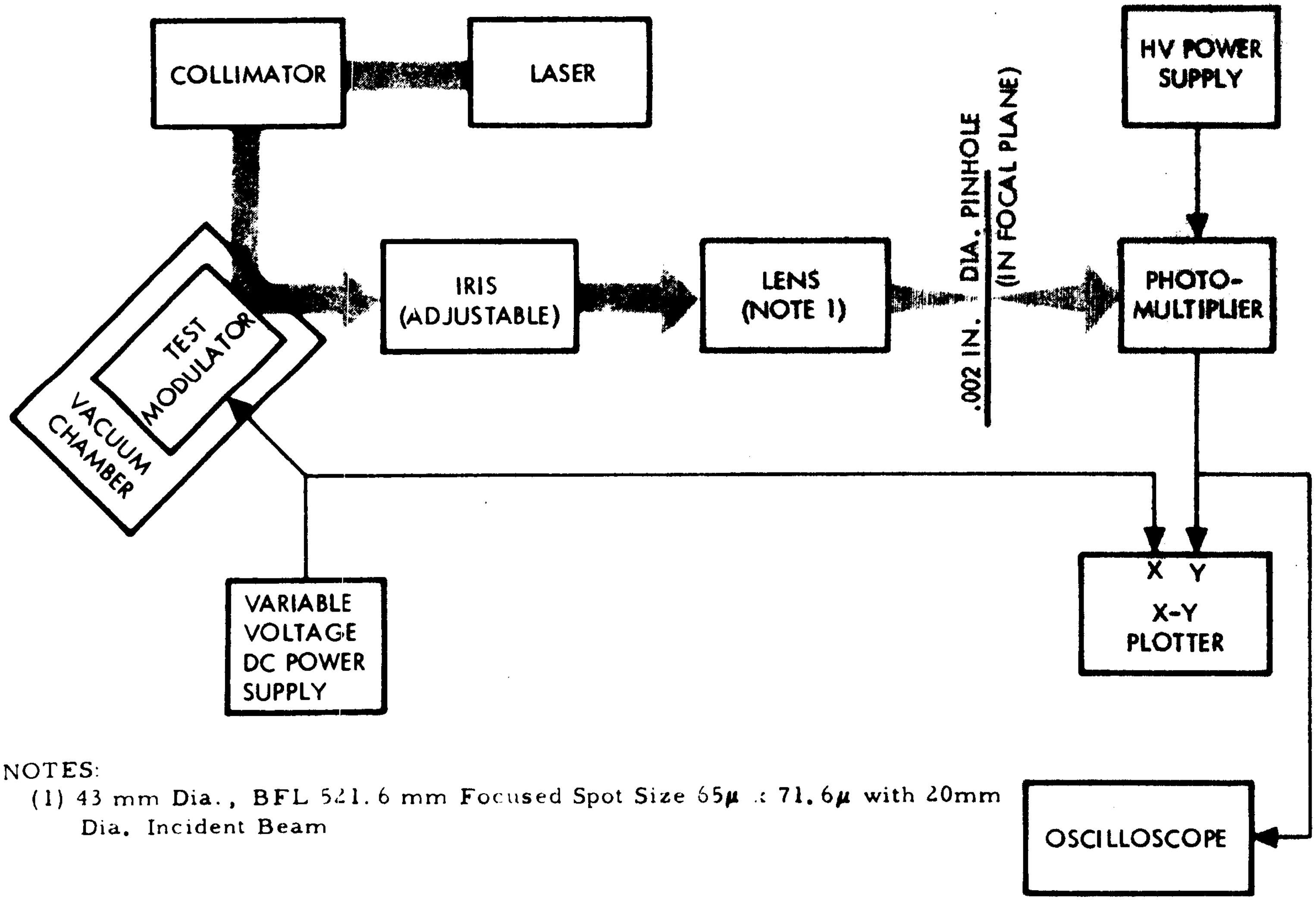

NOTES:
(1) 43 mm Dia., BFL 521.6 mm Focused Spot Size 65μ x 71.6μ with 20mm Dia. Incident Beam

Figure 44. Transfer Function Test Set-up Schematic

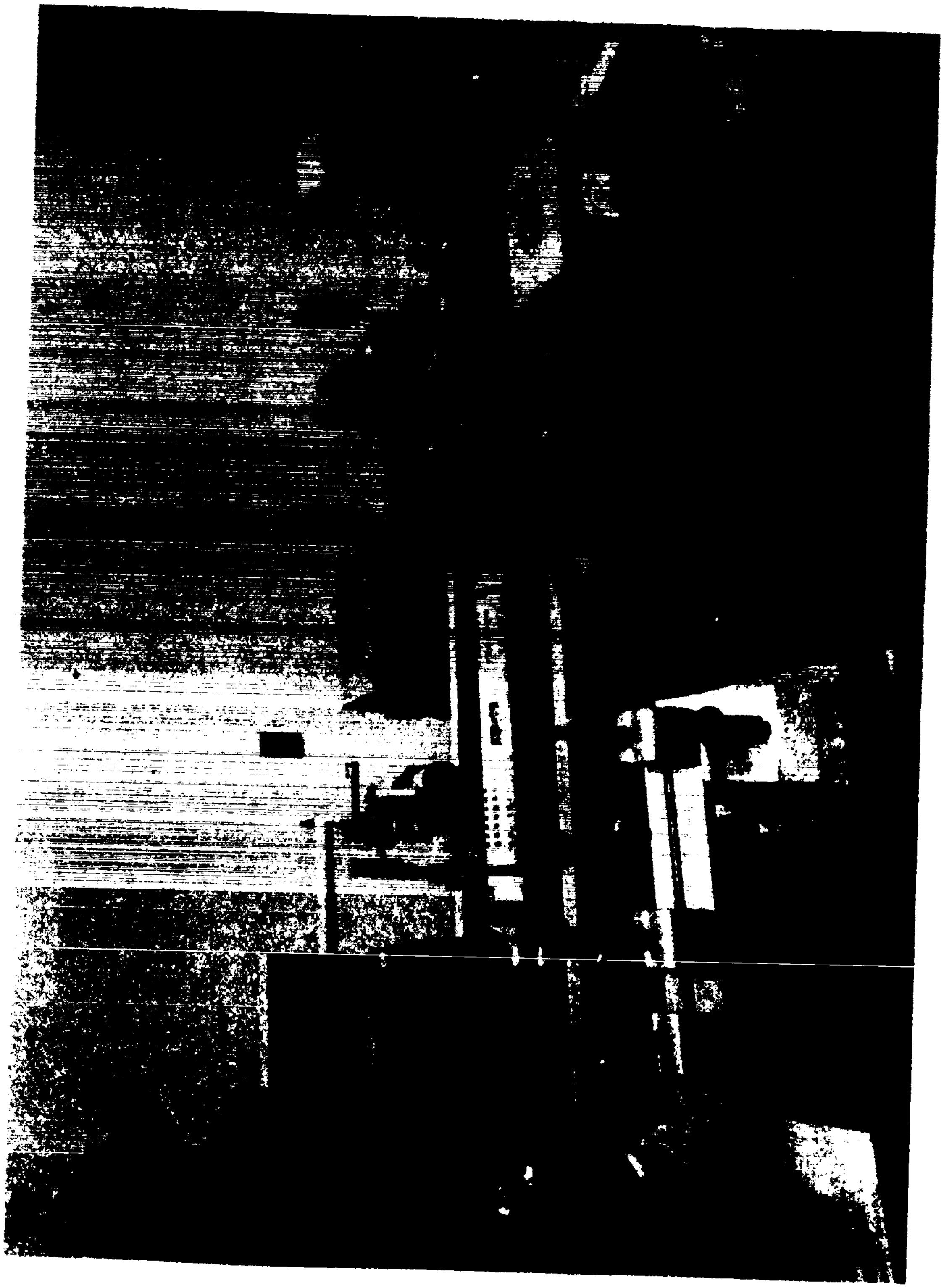

Figure 45. Transfer Function and Frequency Response Test Set-up.

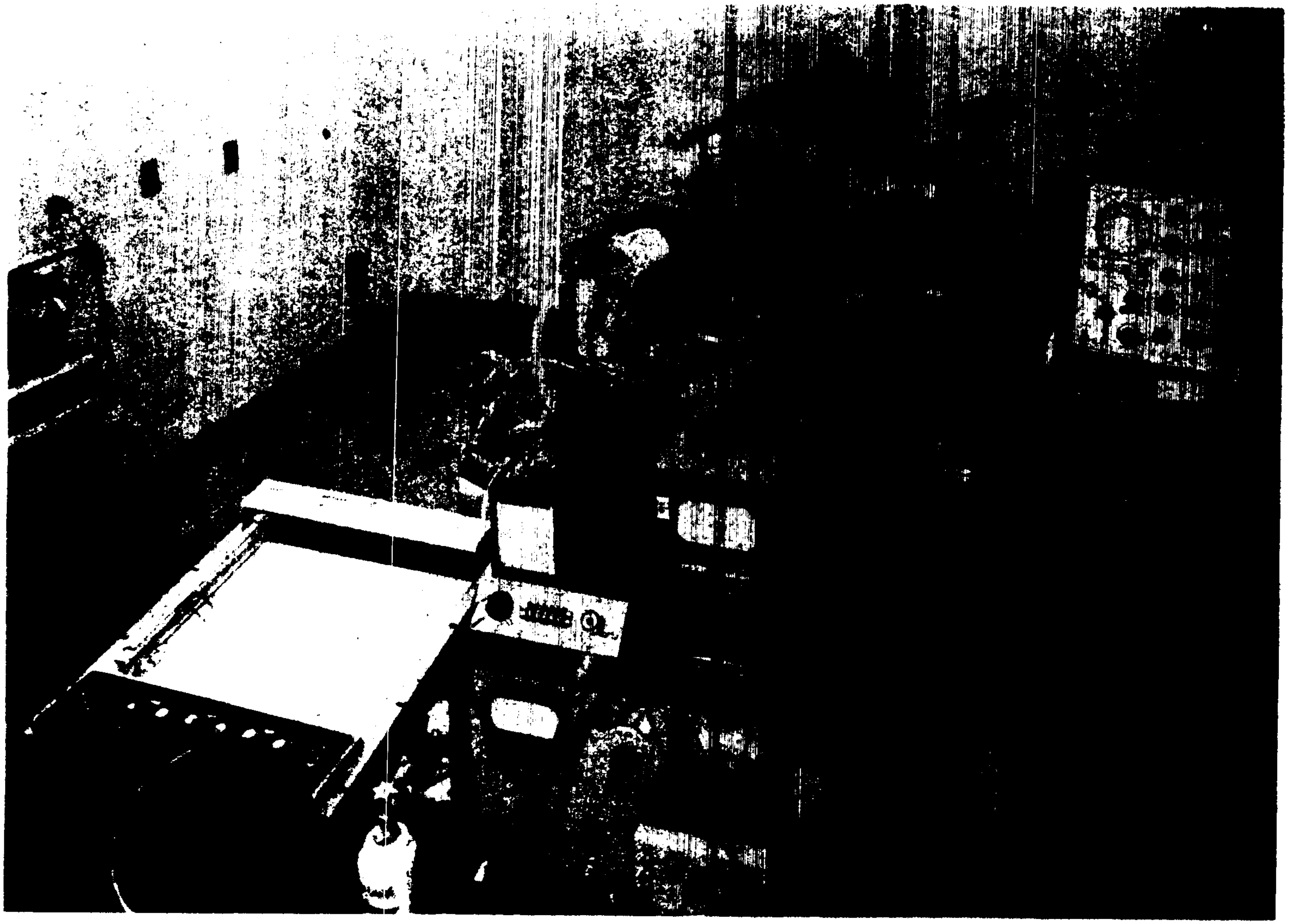

Figure 46. Transfer Function and Frequency Response Test Set-up. X-Y Plotter and Wave Analyzer in Foreground.

The modulator under test is enclosed in a vacuum chamber with an optical quality window in front of the membrane. Figure 44 is a schematic of the test setup used for the D. C. Transfer Function Tests. Figure 45 and Figure 46 are photographs of the test setup used for all transfer function and frequency response testing.

Figures 47 and 48 are the graphs of the test results from Modulators Nos. 1 and 2. The noise on the trace is due primarily to intensity fluctuations in the laser light incident on the membrane.

From Figure 47, Modulator No. 1 is seen to have sufficient linearity for communication purposes over a dynamic range of approximately 10:1. (The proper bias voltage value to use is approximately 40 volts.)

The achievable depth of modulation can be determined using formula (II) from Section I:

$$M = \frac{I_{max} - I_o}{I_o} (100)$$

$$M = \frac{155 - 85}{85} (100) = 82\% \qquad \text{(II)}$$

The driving voltage necessary to produce 82% depth of modulation is 36 volts peak-to-peak.

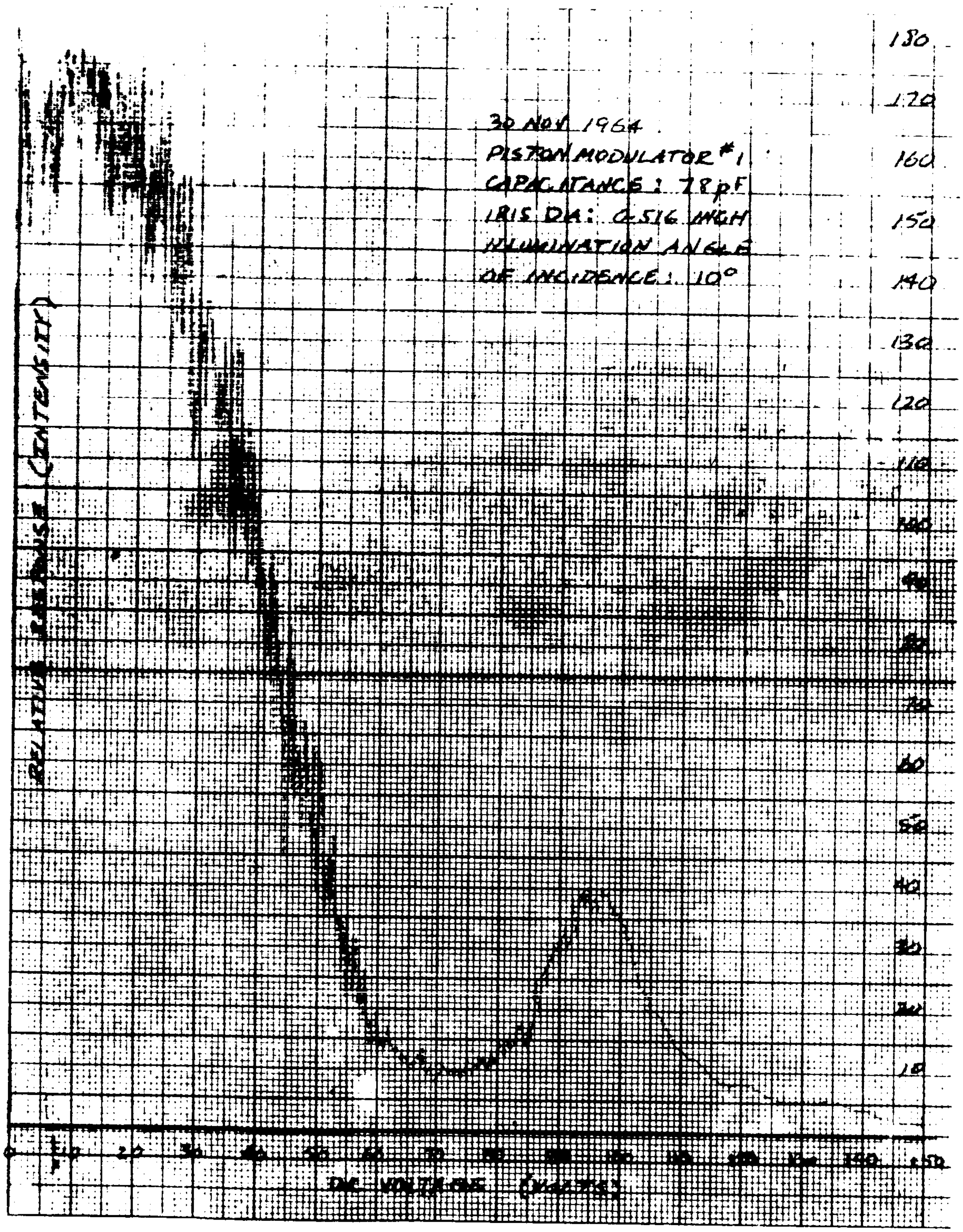

FIGURE 47

D. C. MODULATION TRANSFER CRUVE

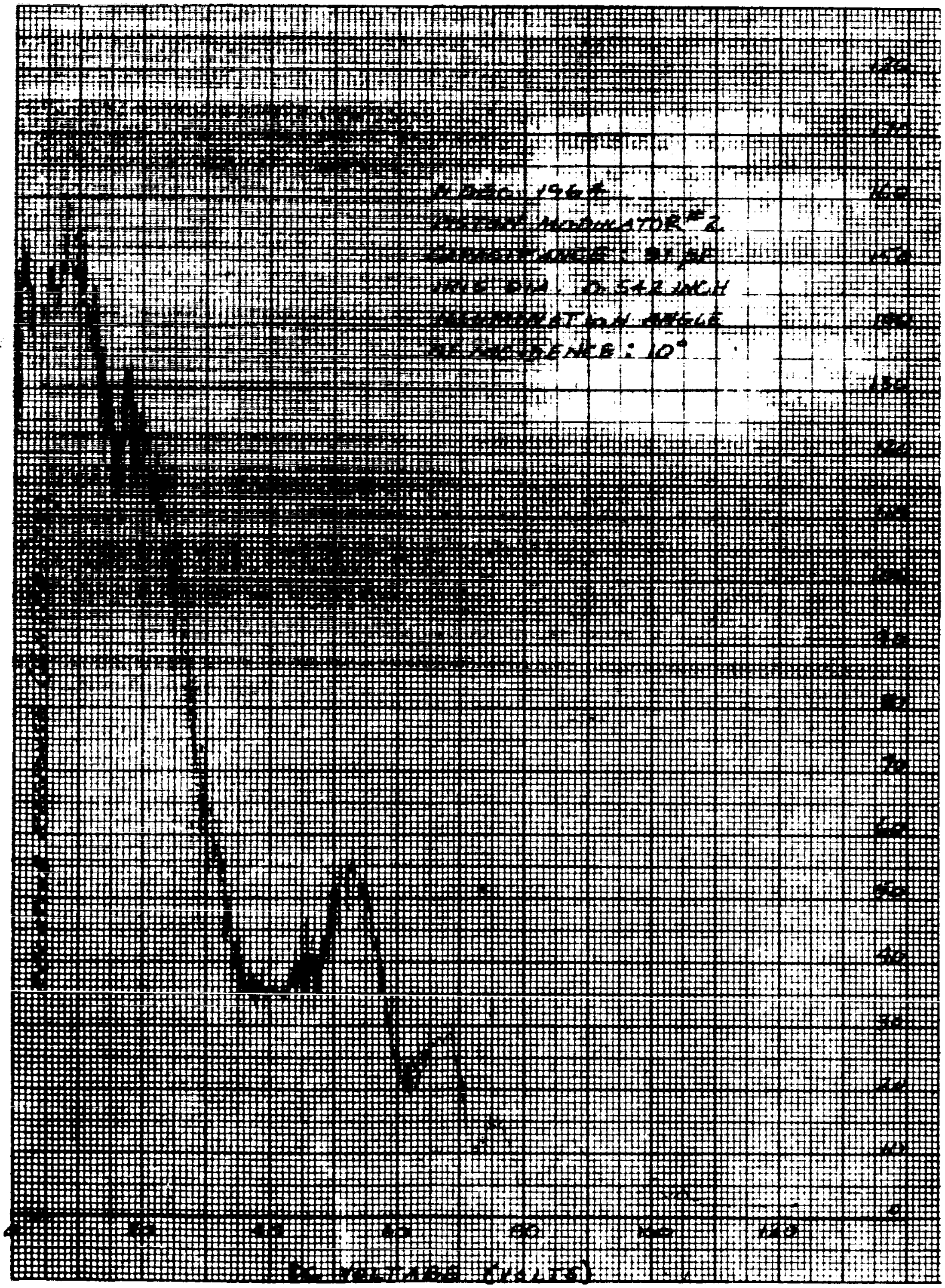

FIGURE 48

D. C. MODULATION TRANSFER CURVE

MEASUREMENTS OF ELECTROSTATIC MODULATOR UNIT MODULATION INDEX AND FREQUENCY RESPONSE

Modulation index is defined as the depth of modulation in the far-field pattern produced by a given modulating voltage. The modulation index for this device is shown to be a function of the gas pressure in the vacuum chamber that encloses the device and of the driving frequency.

The frequency reponse of the piston-type modulator is defined as the variation in the modulation index as a function of the driving frequency. This parameter is also shown to be related to the gas pressure in the vacuum chamber.

The devices tested were Piston-type Modulators Nos. 1 and 2. Construction details are listed in Table 6 and Table 7. Modulator No. 1 was tested to determine the relationship between the fundamental resonant frequency and the pressure in the test vacuum chamber.

The test setup is shown schematically in Figure 49. Referring to Figure 49, the variable voltage DC power supply is used to bias the membrane to the mid-point of the linear portion of the D. C. Transfer characteristic. (This avoids rectification of the AC driving signal which would result in excitation of the membrane at twice the sinewave generator frequency.) The laser energy reflected from the membrane is brought to a focus by the lens. The Airy disc in the focal plane of the lens is observed with the telescope. Relatively large deflection of the membrane occurs at the higher Q fundamental resonance. This appears in the microscope as a marked spreading of the Airy disc. The results of this test are plotted in Figure 50 to show the relationship between fundamental resonant frequency of the device and pressure. A

TABLE 7

PISTON-TYPE MODULATOR PHYSICAL PROPERTIES

Modulator Number	Membrane Diameter (Meter)	Membrane Thickness (Meter)	Measured Capacity (Farad)	Computed Gap Distance (Meter) (Note 3)	Measured Membrane Tension (Note 1) (Newton/meter^2)	Measured Membrane Fundamental Resonant Frequency (Note 2) KCPS
#1	2.00×10^{-2}	6.35×10^{-6}	78×10^{-12}	3.56×10^{-5}	4.81×10^{7} (=6.970 lb/in^2)	4.50 @ 50 micron chamber pressure
#2	2.00×10^{-2}	12.7×10^{-6}	91×10^{-12}	3.05×10^{-5}	Not measured	3.75 @ 50 micron chamber pressure
#3	2.00×10^{-2}	6.35×10^{-6}	95×10^{-12}	2.92×10^{-5}	2.91×10^{7} (=4,220 lb/in^2)	4.86 @ 58 micron chamber pressure

NOTES:

1. - Measured by interferometer method (Section 4).
2. - Membrane bias voltage greater then peak value of sine wave driving voltage (to prevent frequency doubling).
3. - These are the gap settings used for all Transfer Function and Frequency Response Tests.

NOTES:
(1) 43mm Dia., BFL 521.6 mm Focused Spot Size 65μ x 71.6μ with 20 mm Dia. Incident Beam

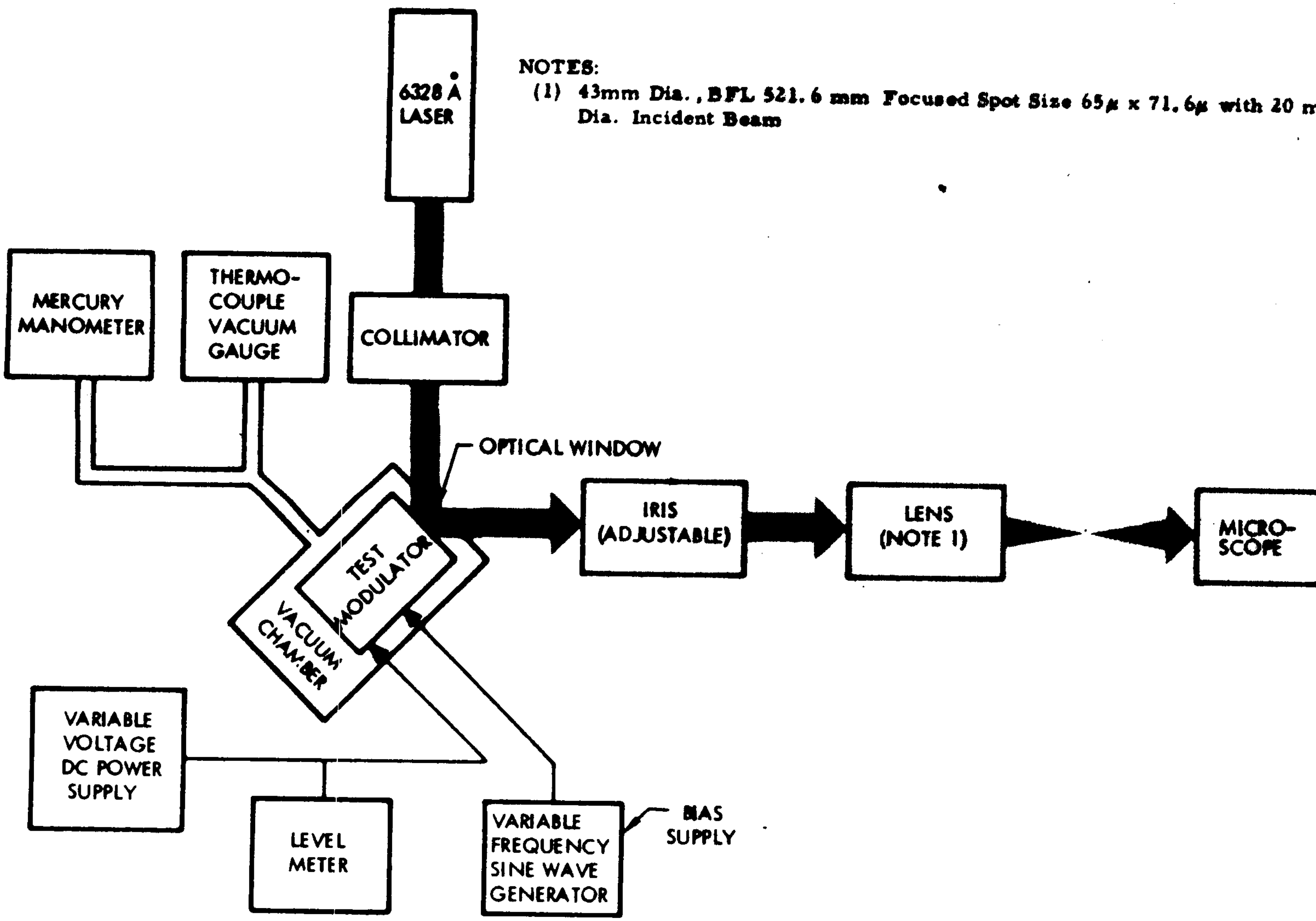

Figure 49. Test Set-up Schematic, Fundamental Resonant Frequency vs. Pressure Test

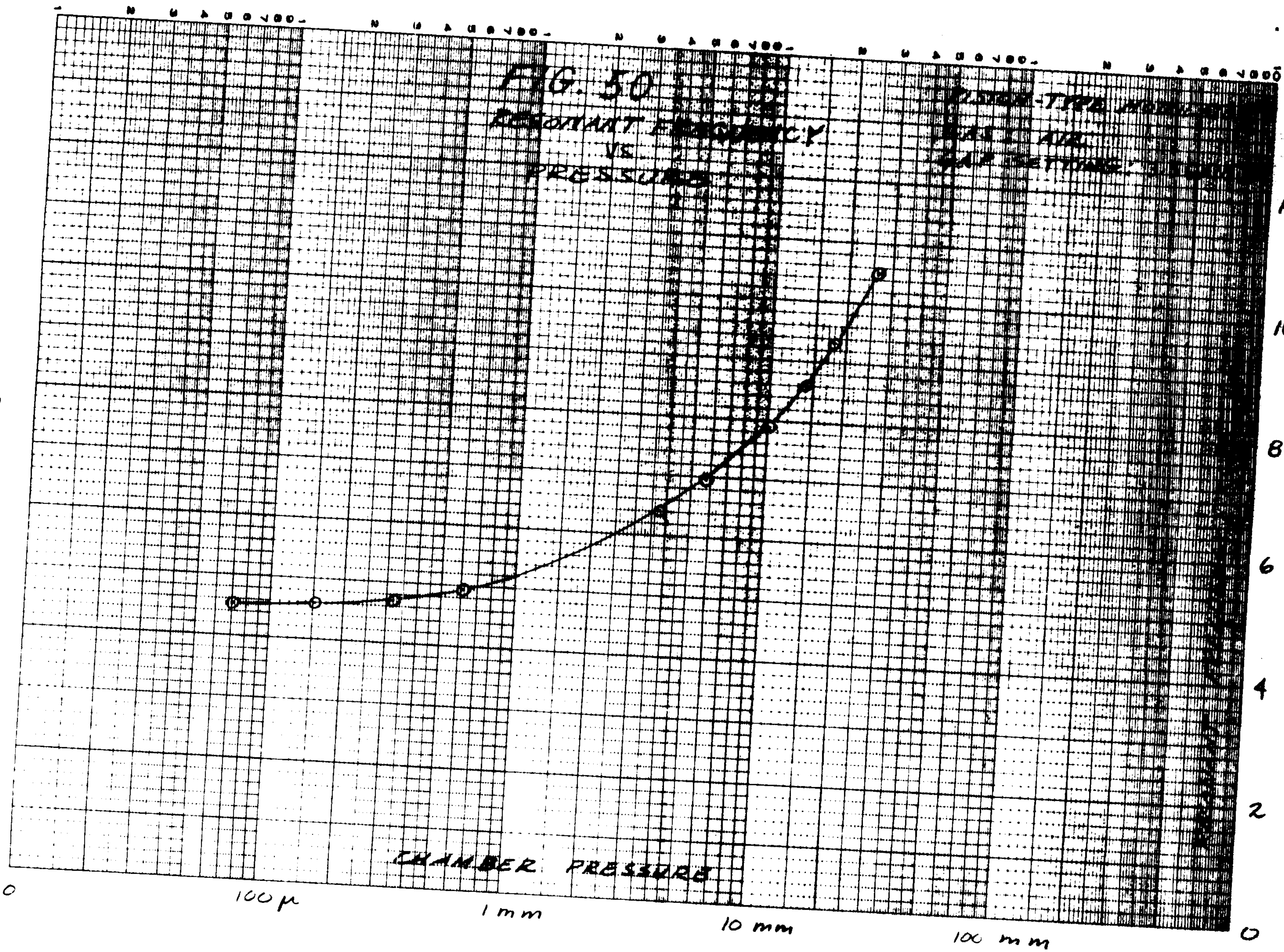
FIG. 50
RESONANT FREQUENCY
VS
PRESSURE
GAS: AIR
12
10
8
6
4
2
0
0
100 μ
1 mm
10 mm
100 mm
CHAMBER PRESSURE

second test setup is used to obtain both modulation index and frequency response data. The test setup is illustrated schematically in Figure 51. Figures 45 and 46 are photographs of the equipment used.

Referring to Figure 51, the lens and pinhole are used to place the photomultiplier in a simulated far-field environment. (This is the same technique used in the D. C. Transfer Function Tests.) The pinhole is adjusted to be in the focal plane of the lens with the modulator membrane undeflected and is centered on the Airy disc.

The wave analyzer that is used is of the type that incorporates a variable frequency oscillator and a tunable receiver tracked to the same dial. The dial is driven by a sweep drive unit which also provides an electrical position signal for the X axis of an X-Y recorder. The tunable receiver has a rectified signal output that is used to provide the Y-axis signal for the recorder. The output of the variable frequency oscillator is amplified and used to drive the electrostatic modulator unit under test.

Actuation of the sweep drive on the wave analyzer will cause the X-Y recorder to plot the photomultiplier signal current amplitude versus frequency. (The photomultiplier signal current is directly proportional to the depth of modulation.)

Prior to an actual test run, the vacuum chamber is pumped down. For the test run at 50 micron chamber air pressure, the vacuum pump is allowed to run continuously. For the higher pressure runs, the chamber is pumped down to 50 microns and then back-filled with either air or Freon 12 to the desired pressure and sealed. (Freon 12 is used to sustain the higher electrostatic field intensities required to modulate the membrane at the higher pressures.

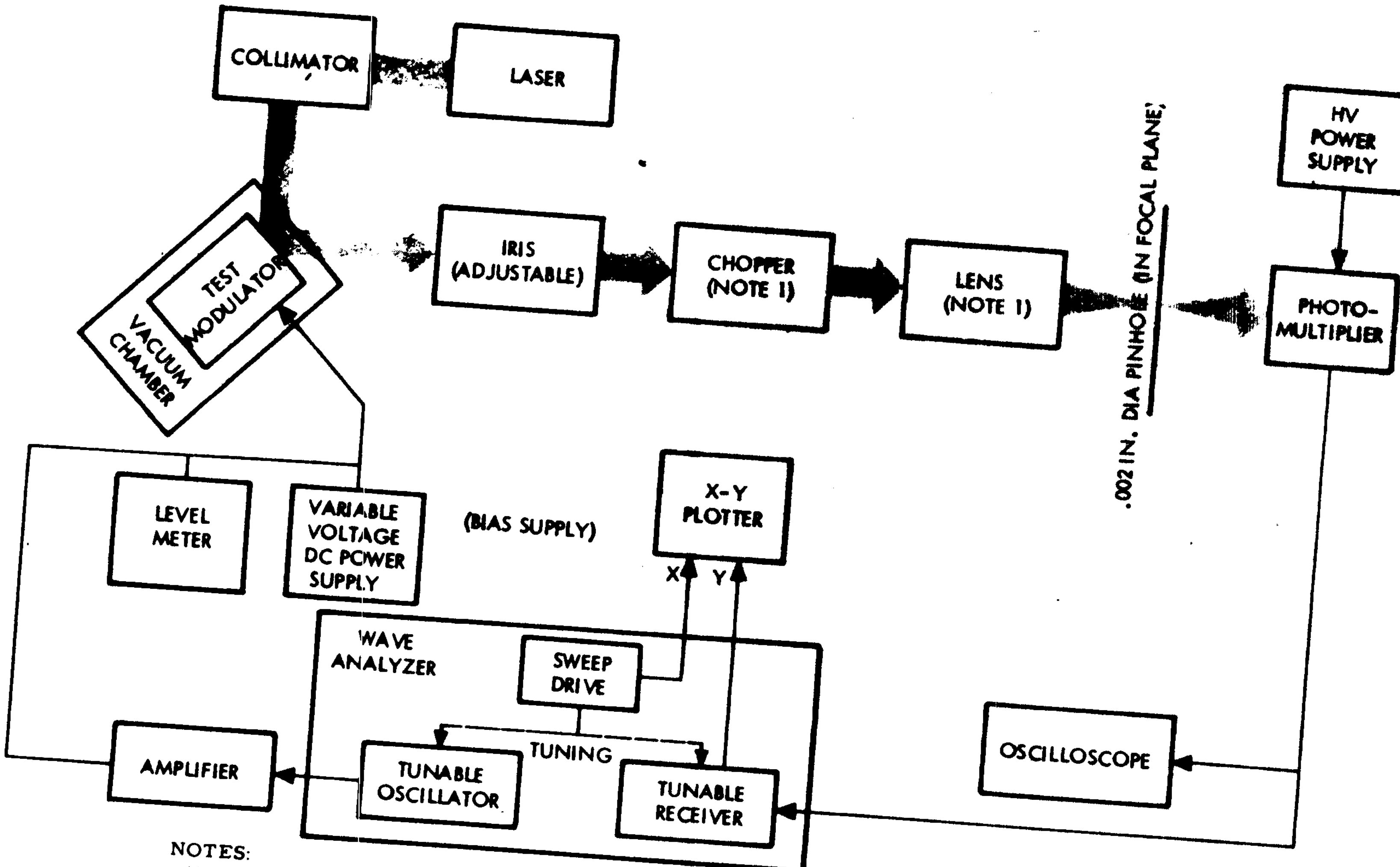

NOTES:

(1) Chopper is used ONLY to check amplitude of unmodulated light

(2) 43 mm diameter, BFL: 521.6 mm. Focused spot size: 65μ by 71.6μ when illuminated on axis with 20mm diameter collimated light beam.

Figure 51. Modulation Index and Frequency Response Test Set-up

Freon 12 is a cheap and readily available refrigerant gas and has a dielectric strength of approximately 2.4 times that of air. Freon C-318 can be used to sustain an electrostatic field intensity four-times that of air. This is the highest dielectric strength gas available at present. Its other properties are quite similar to Freon 12.)

As the next step prior to the test run, the driving signal and the bias are adjusted for maximum depth of linear modulation at the fundamental resonance (f_o). Actuating the sweep drive will then cause the recorder to plot the modulation index versus frequency.

The test results are shown by Figures 52 through 56 and are tabulated in Table 8. Figure 50, resonant frequency versus pressure, shows no significant further change in resonant frequency for pressures below 200 microns. The resonant frequency for the device in a perfect vacuum is thus indicated by the test results. Measured resonant frequencies and resonant frequencies computed using the classical formula, Formula (I), are given below:

Piston-type Modulator	f_o Measured	f_o Computed from Formula (I)
#1	4.50 KC	7.1 KC
#3	4.86 DC	5.5 KC

More data needs to be taken but these are not unreasonable results considering the number of variables that affect the membrane resonant frequency.

Referring to Figure 52 through 56, the device is seen to have a flat response from very low frequencies almost to f_o, a desirable characteristic for a transducer.

TABLE 8

PISTON-TYPE MODULATOR #2 - MODULATION INDEX AND FREQUENCY RESPONSE DATA

TEST RUN NUMBER	CHAMBER PRESSURE	GAS	f_o (KCPS)	DEPTH OF MOD. at f_o	DEPTH OF MOD. BELOW f_o	PEAK TO PEAK SINE WAVE DRIVING VOLTAGE, VOLTS	COMPUTED DRIVING VOLTAGE REQUIRED FOR 50% DEPTH OF MODULATION BELOW f_o
1 -Fig.	50 microns	Air	3.75	80%	0.9%	0.237	13.2
3 -Fig.	4.0 MM	Air	6.40	75%	1.4%	1.45	52.0
5 -Fig.	24.0 MM	Air	12.8	60%	6.4%	28.2	220.0
6 -Fig.	30.0 MM	Freon 12	15.1	75%	2.8%	45.1	805.0 (2)
7 -Fig.	100.0 MM	Freon 12	27.0	33.%	not measured	296.0	-

NOTES: (1) MODULATOR GAP DISTANCE: 3.05×10^{-5} meter.

(2) GAP WILL BREAKDOWN BEFORE THIS VALUE CAN BE ACHIEVED FOR THIS UNIT. (SOME EVIDENCE OF NON-DESTRUCTIVE BREAKDOWN RESULTED WHEN THE DRIVE VOLTAGE WAS INCREASED ABOVE 300 V IN RUN # 7.)

The rising characteristic at the low frequency end of the modulation index plot, (most apparent in Figures 54 and 55), is due to the pressure relief port. At very low frequencies approaching zero frequency or D.C., the only restoring force on the membrane is that due to its tension. At very low frequencies, the modulation index therefore approaches the value determined by the D.C. Transfer Function and is independent of the pressure in the chamber. It is shown by the test results that practical modulator units can be constructed with bandwidths of at least 13 KC up to the first resonance.

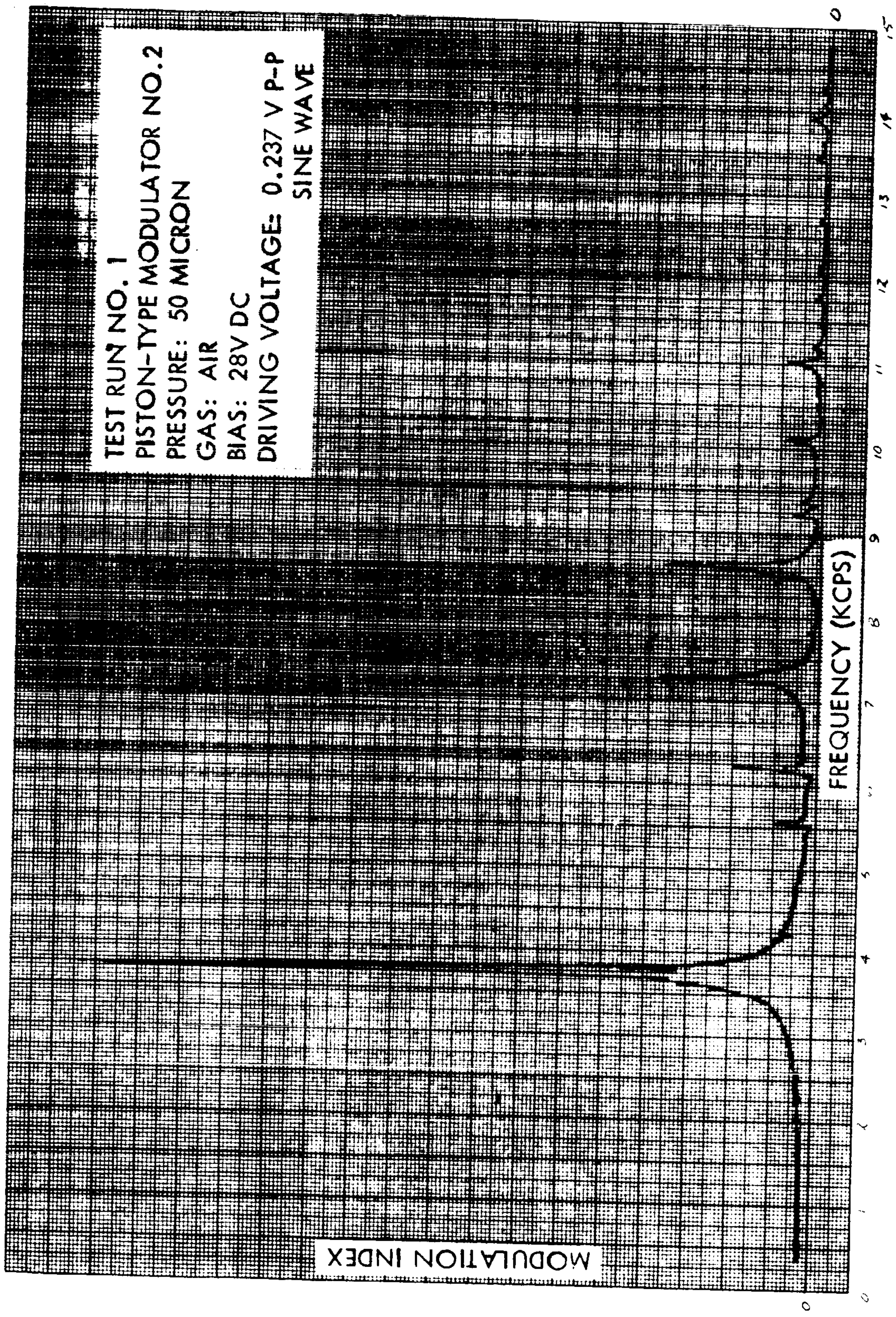
TEST RUN NO. 1
PISTON-TYPE MODULATOR NO. 2
PRESSURE: 50 MICRON
GAS: AIR
BIAS: 28V DC
DRIVING VOLTAGE: 0.237 V P-P
SINE WAVE
FREQUENCY (KCPS)
MODULATION INDEX

Figure 52

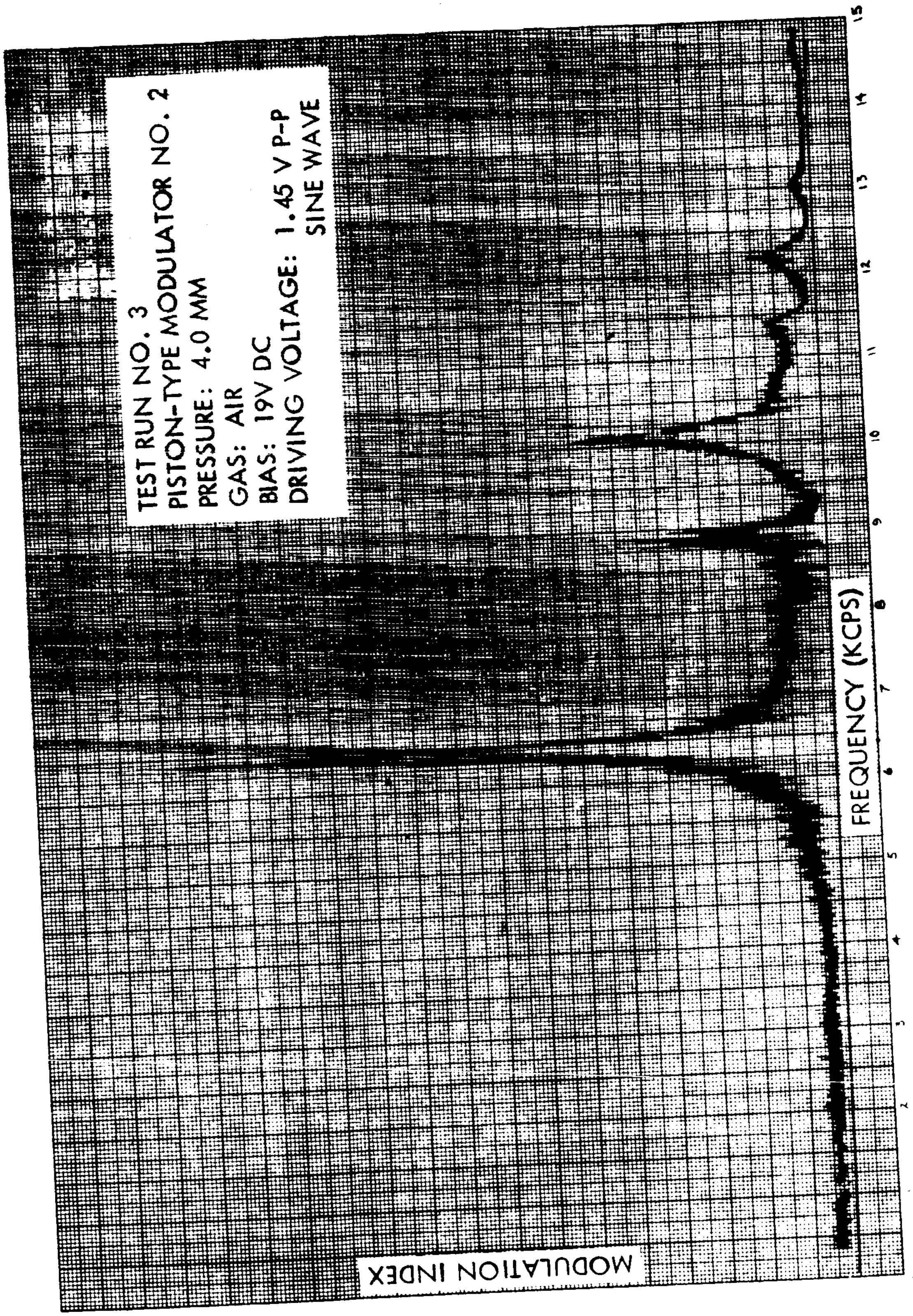
TEST RUN NO. 3
PISTON-TYPE MODULATOR NO. 2
PRESSURE: 4.0 MM
GAS: AIR
BIAS: 19V DC
DRIVING VOLTAGE: 1.45 V P-P
SINE WAVE
FREQUENCY (KCPS)
MODULATION INDEX

Figure 53

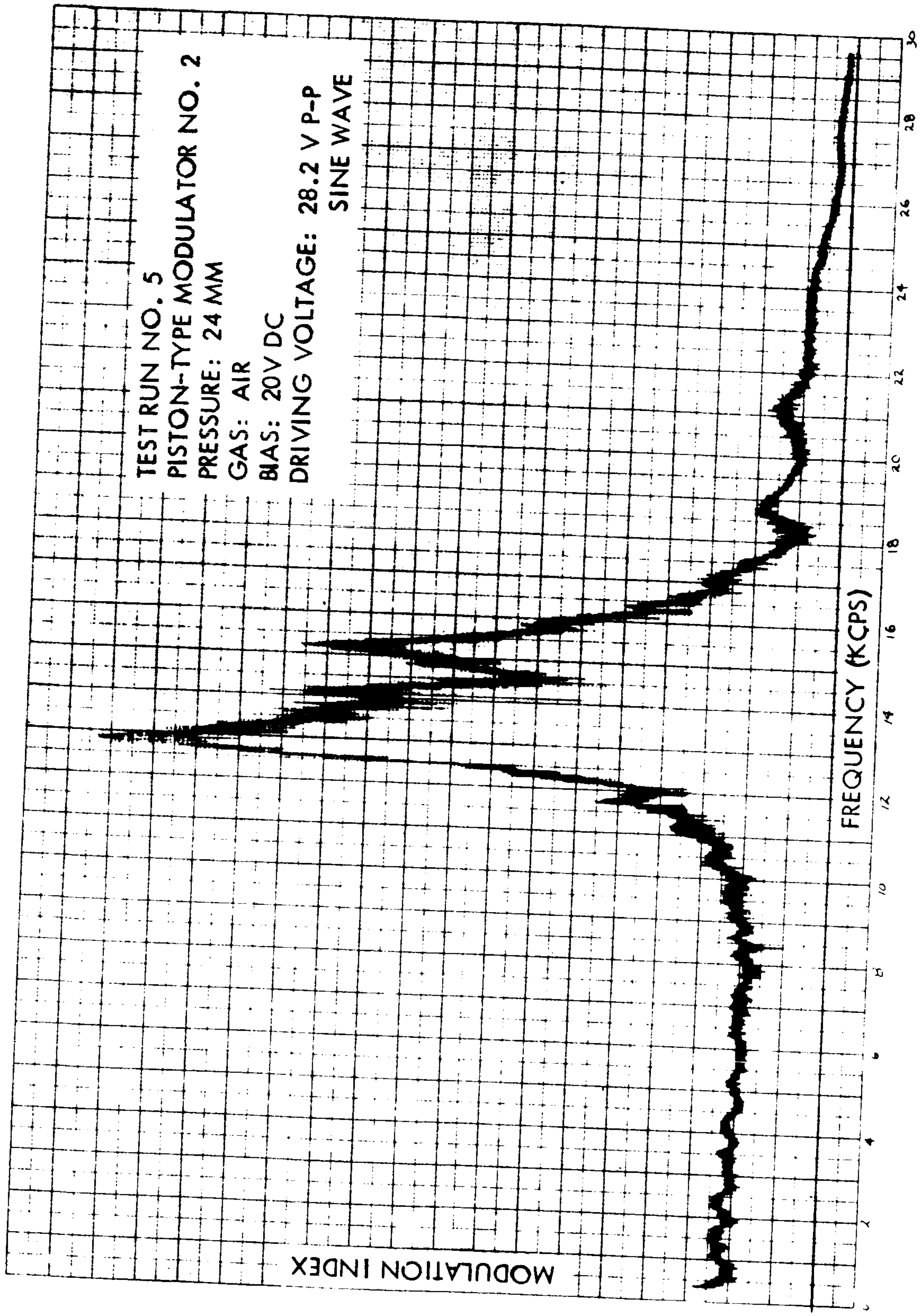
TEST RUN NO. 5
PISTON-TYPE MODULATOR NO. 2
PRESSURE: 24 MM
GAS: AIR
BIAS: 20V DC
DRIVING VOLTAGE: 28.2 V P-P
SINE WAVE
FREQUENCY (KCPS)
MODULATION INDEX
0
2
4
6
8
10
12
14
16
18
20
22
24
26
28
30

Figure 54

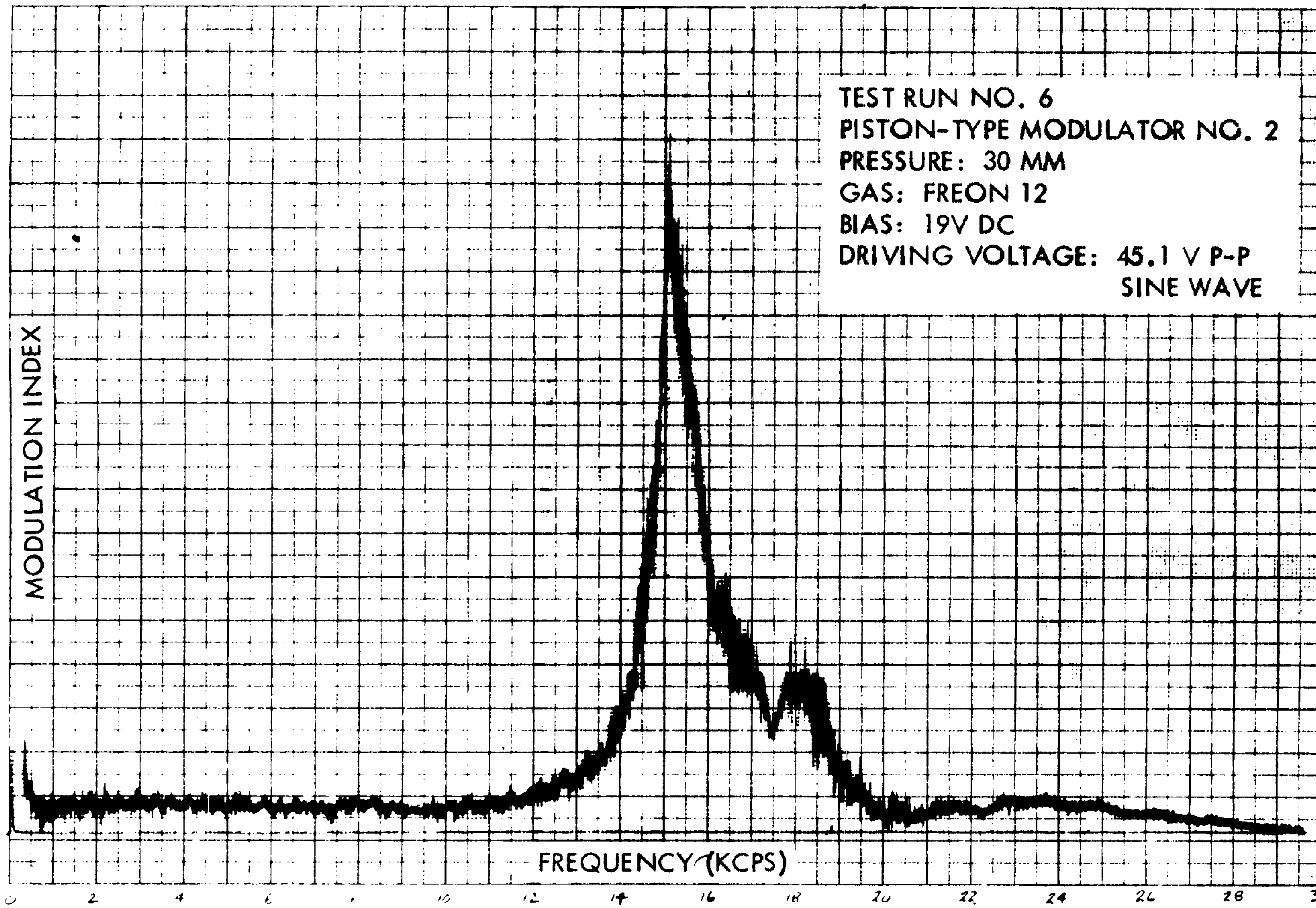
TEST RUN NO. 6
PISTON-TYPE MODULATOR NO. 2
PRESSURE: 30 MM
GAS: FREON 12
BIAS: 19V DC
DRIVING VOLTAGE: 45.1 V P-P
SINE WAVE
MODULATION INDEX
FREQUENCY (KCPS)

Figure 55

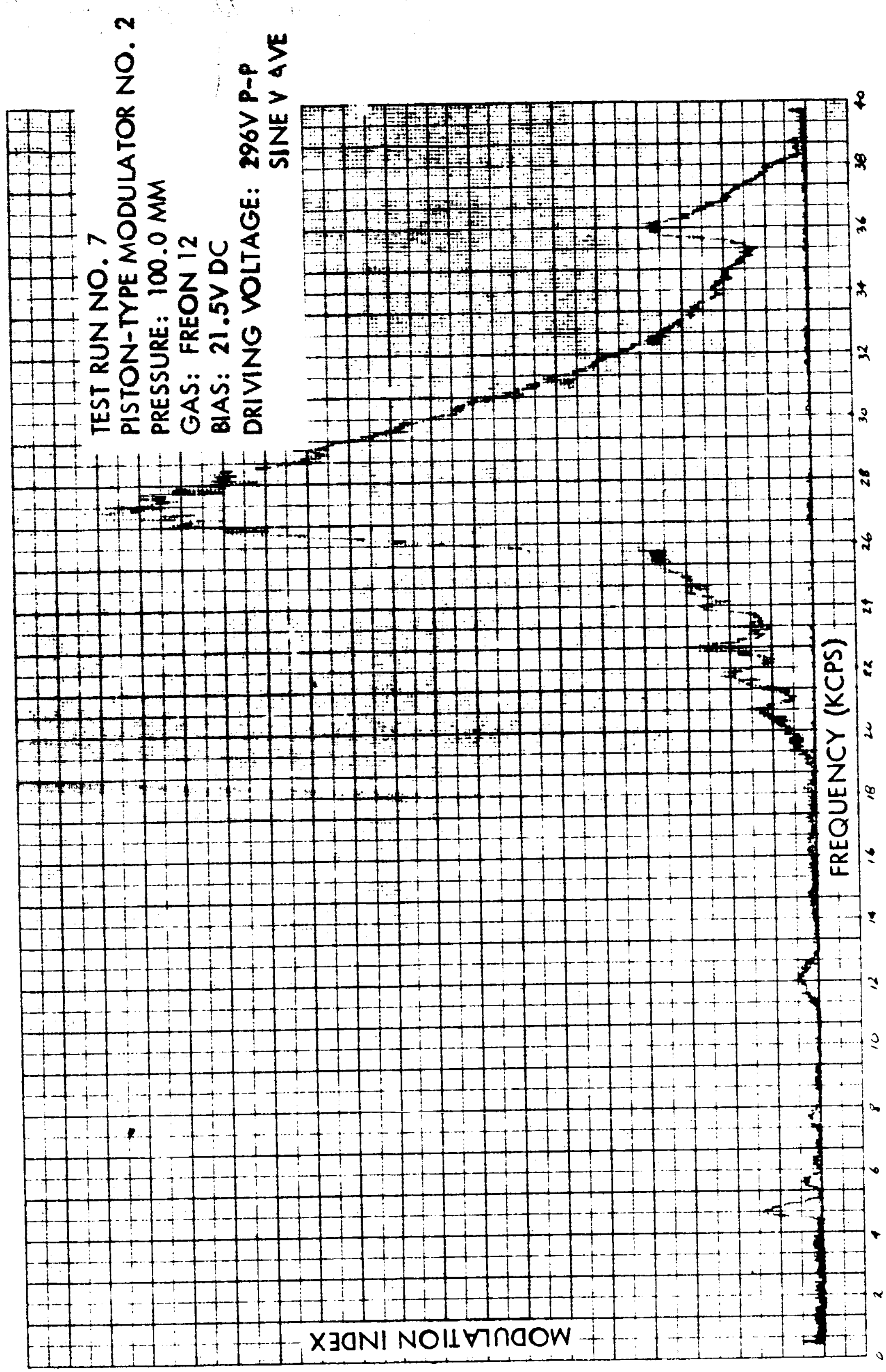
TEST RUN NO. 7
PISTON-TYPE MODULATOR NO. 2
PRESSURE: 100.0 MM
GAS: FREON 12
BIAS: 21.5V DC
DRIVING VOLTAGE: 296V P-P
SINE V AVE
MODULATION INDEX
FREQUENCY (KCPS)
0
2
4
6
8
10
12
14
16
18
20
22
24
26
28
30
32
34
36
38
40

Figure 56

SECTION 5

NEW TECHNOLOGY

NEW TECHNOLOGY

In keeping with the obligation of the Contractor, as indicated in the requirements for Type III reports, and with the obligations contained in paragraph C.23 of the basic agreement, NAS 7-251, dated November 20, 1963, the following novel technical work is reported.

1. The partial pressurization of the electrostatic modulator unit has the effect of increasing the first resonant frequency in the membrane. The chamber size, pressure relief port size, as well as gas pressure determine the amount of increase. An increase of five times the unpressurized resonant frequency in the membrane has been measured in the laboratory.
2. An analysis of the effective off-axis aperture of a corner reflector shows that a regular hexagon aperture is optimum only for the on-axis case. When the aperture is illuminated off-axis, the cosine law does not hold and consequently the optimum geometry is determined by other relationships. The optimum geometric shape of the aperture becomes an irregular polygon.
3. The design of the modulating surface as an array of two centimeter diameter modulating elements to be installed in a precision retro-directive corner reflector has several distinct advantages. The success of fabrication of the corner reflector does not depend upon the intricate fabrication of the modulating surface. The button modulators can be individually fabricated and tested prior to installation in the corner reflector. Finally, any improperly installed modulating element can be replaced in the corner reflector.

The above technology will be reported to our Patent Section in the form of Patent Disclosures. The data therein will be treated as disclosed in our letter 64MA11810, dated November 3, 1964.

SECTION 6

APPENDICES

APPENDIX I

BASIC DESIGN OF THE RETRODIRECTIVE REFLECTOR

The corner cube retrodirective reflector consists of three mutually perpendicular reflecting surfaces. The "optical axis" of the assembly, used as the x-axis of the system, is defined as an axis making equal angles with the normals of the three reflecting surfaces.

Since the normal to a surface is parallel to the line of intersection of the other two surfaces, the three surface intersections can be used temporarily to define a three dimensional system to obtain the direction cosines of the "optical axis". The "optical axis" makes equal angles to the three normals (See Figure I-1) and thus, by definition

$$\cos^2\alpha_1 + \cos^2\alpha_2 + \cos^2\alpha_3 = 1$$

$$3\cos^2\alpha = 1$$

$$\cos\alpha_1 = \cos\alpha_2 = \cos\alpha_3 = \frac{1}{\sqrt{3}} \qquad \text{I(1)}$$

The optical axis is now used as the x-axis of the system, and for convenience the first reflecting surface is taken as perpendicular to the z-axis. For clarity in the following derivations, numerical subscripts, unless otherwise defined, will refer to the reflecting surfaces in sequence as a light ray would traverse the system. Thus, $\cos\alpha_2$ would be the direction cosine of the normal of the second surface to the x-axis, $\cos\beta_2$ would be the direction cosine of the normal of the second surface to the y-axis, and $\cos\gamma_2$ would be the direction cosine of the normal of the second surface to the z-axis.

In subsequent equations, the constant A_{31} would refer to a light ray reflecting first from the 3rd surface, then the 1st surface and finally, the 2nd reflecting surface.

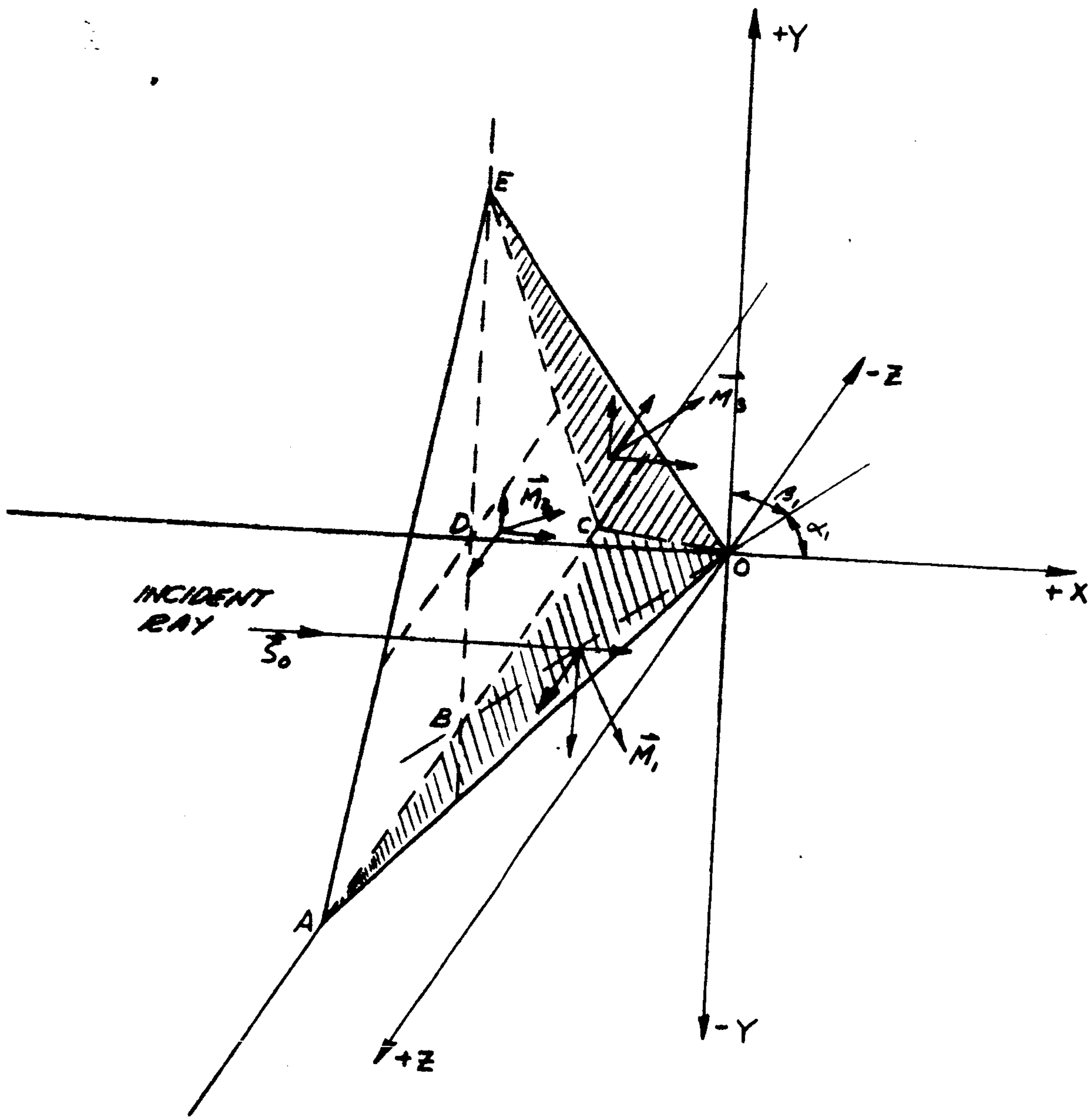

FIGURE I-1

THE CORNER CUBE REFLECTOR

GEOMETRIC REPRESENTATION

As defined, the normal to the first surface was chosen as perpendicular to the z-axis, therefore

$$\cos^2\alpha_1 + \cos^2\beta_1 + \cos^2\gamma_1 = 1$$

From equation I(1)

$$\frac{1}{3} + \cos^2\beta_1 + 0 = 1$$

$$\cos\beta_1 = \pm\sqrt{\frac{2}{3}} = \pm\frac{1}{3}\sqrt{6} \qquad \text{I(2a)}$$

In later derivations, vector notation will be used in the optical ray tracing of the path of a ray through the corner cube reflector. Thus the normal to a surface is represented by a unit vector, perpendicular to the back surface of the reflector, (See FigureI-1), where $\vec{M}_1$ is the first unit vector. The components of this unit vector parallel to the three axes are positive in the x-direction, negative in the y-direction and zero in the z-direction.

Thus the normal to the first reflecting surface can be expressed in terms of the following three direction cosines

$$\left.\begin{aligned}
\cos\alpha_1 &= \frac{1}{\sqrt{3}} = \frac{1}{3}\sqrt{3} \\
\cos\beta_1 &= -\sqrt{\frac{2}{3}} = -\frac{1}{3}\sqrt{6} \\
\cos\gamma_1 &= 0
\end{aligned}\right\} \qquad \text{I(2)}$$

or in terms of the unit vector

$$\vec{M}_1 = \frac{1}{\sqrt{3}}\vec{i} - \sqrt{\frac{2}{3}}\vec{j}$$

Since the orientation of surface 1 was chosen with $\cos \gamma_1 = 0$, the other two reflecting surfaces are symmetrical to the x-y plane and, as will be proved,

$$\left.\begin{aligned} \cos\beta_2 &= \cos\beta_3 \\ -\cos\gamma_2 &= \cos\gamma_3 \end{aligned}\right\} \qquad \text{I(4)}$$

From analytical geometry, the cosine of the angle between two directed lines is equal to the sum of the products of the corresponding direction cosines. Since all three normals are mutually perpendicular, the following equations are obtained.

$$\cos\alpha_1 \cos\alpha_2 + \cos\beta_1 \cos\beta_2 + \cos\gamma_1 \cos\gamma_2 = 0 \qquad \text{I(5a)}$$

$$\cos\alpha_1 \cos\alpha_3 + \cos\beta_1 \cos\beta_3 + \cos\gamma_1 \cos\gamma_3 = 0 \qquad \text{I(5b)}$$

$$\cos\alpha_2 \cos\alpha_3 + \cos\beta_2 \cos\beta_3 + \cos\gamma_2 \cos\gamma_3 = 0 \qquad \text{I(5c)}$$

Substituting I(1,2) into I(5a) and I(5b)

$$\left(\frac{1}{\sqrt{3}}\right)\left(\frac{1}{\sqrt{3}}\right) + \left(-\sqrt{\frac{2}{3}}\right)\cos\beta_2 + (0)\cos\gamma_2 = 0$$

$$\cos\beta_2 = \frac{1}{\sqrt{6}} \qquad \text{I(6a)}$$

$$\left(\frac{1}{\sqrt{3}}\right)\left(\frac{1}{\sqrt{3}}\right) + \left(-\sqrt{\frac{2}{3}}\right)\cos\beta_3 + (0)\cos\gamma_3 = 0 \qquad \text{I(6b)}$$

$$\cos\beta_3 = \frac{1}{\sqrt{6}}$$

Then from the relationship

$$\cos^2\alpha_2 + \cos^2\beta_2 + \cos^2\gamma_2 = 1$$

$$\cos\gamma_2 = \pm\frac{1}{\sqrt{2}}$$

From Figure I-1, it is seen that all three components of the unit vector are positive, thus

$$\cos \gamma_2 = + \frac{1}{\sqrt{2}} \qquad \text{I(6c)}$$

Substituting I(1,6a,6b,6c) in I(5c)

$$\left(\frac{1}{\sqrt{3}}\right)\left(\frac{1}{\sqrt{3}}\right) + \left(\frac{1}{\sqrt{6}}\right)\left(\frac{1}{\sqrt{6}}\right) + \left(\frac{1}{\sqrt{2}}\right)\cos \gamma_3 = 0$$

$$\cos \gamma_3 = - \frac{1}{\sqrt{2}} \qquad \text{I (6d)}$$

The three unit vectors, representing the three normals to the three reflecting surfaces, are expressed as follows

$$\left.\begin{aligned} \vec{M}_1 &= \frac{1}{\sqrt{3}}\vec{i} - \sqrt{\frac{2}{3}}\,\vec{j} \\ \vec{M}_2 &= \frac{1}{\sqrt{3}}\vec{i} + \frac{1}{\sqrt{6}}\vec{j} + \frac{1}{\sqrt{2}}\vec{k} \\ \vec{M}_3 &= \frac{1}{\sqrt{3}}\vec{i} + \frac{1}{\sqrt{6}}\vec{j} - \frac{1}{\sqrt{2}}\vec{k} \end{aligned}\right\} \qquad \text{I(7)}$$

As shown in Figure I-1, the origin of the system is taken as the point of intersection of the three reflecting surfaces, i.e., the point 0 (o,o,o) is considered common to all three planes. From analytical geometry, the three planes are expressed in terms of the direction cosines of the normal to the plane and the perpendicular distance from the plane to the origin, which in this case is always zero. Thus,

$$X_i \cos \alpha_i + Y_i \cos \beta_i + Z_1 \cos \gamma_i = 0 \qquad \text{I (8)}$$

The substitution of the direction cosines from I (7) and I (8) produces the three expressions for the three reflecting planes,

Plane 1 $\quad X_1 - \sqrt{2}Y_1 = 0 \qquad$ I (8a)

Plane 2 $\quad X_2 + \frac{1}{\sqrt{2}}Y_2 + \frac{1}{2}\sqrt{6}\,Z_2 = 0 \qquad$ I (8b)

Plane 3 $\quad X_3 + \frac{1}{\sqrt{2}}Y_3 - \frac{1}{2}\sqrt{6}\,Z_3 = 0 \qquad$ I (8c)

Retrodirective Action of the Corner Cube:

It can be proved by optical ray tracing and analytical geometry that a light ray entering the aperture of the corner cube will be returned exactly in the direction from which it arrived. This method of proof, while rigid, is cumbersome and time-consuming.

A much easier proof is provided by the techniques of vector analysis, very thoroughly described in Military Standardization Handbook, MIL-HDB-141, Oct. 1962, on Optical Design. The procedure given in the handbook is used in the following analysis.

The incident light ray is expressed vectorially by

$$\vec{S}_0 = \vec{i} \qquad \mathrm{I}(9)$$

The ray reflected from a surface is

$$\vec{S}_i = \vec{S}_{i-1} + \Gamma_i \vec{M}_i \qquad \mathrm{I}(10)$$

Where $\vec{M}_i$ is obtained from A(7), and

$$-\Gamma_i = 2\,\vec{S}_{i-1} \cdot \vec{M}_i \qquad \mathrm{I}(11)$$

Thus, the following is obtained

$$\vec{S}_1 = \frac{1}{3}\vec{i} + \frac{2\sqrt{2}}{3}\vec{j} \qquad \mathrm{I}(12)$$

$$\vec{S}_2 = -\frac{1}{3}\vec{i} + \frac{1}{3}\sqrt{2}\,\vec{j} - \frac{1}{3}\sqrt{6}\,\vec{k} \qquad \mathrm{I}(13)$$

$$\vec{S}_3 = -\vec{i} \qquad \mathrm{I}(14)$$

The passage of the light ray into, through and out of the triple-reflecting corner cube reflecter is given by equations I(9, 12, 13 and 14). Equation I(14) states that the ray is progressing from right to left, parallel to the x-axis. In other words, the light ray is returning to its source.

Error Analysis of the Corner Cube Reflector:

All three reflecting surfaces in the preceeding analysis was assumed to be exactly 90°. A small error δ in any one of these 90° angles will produce an error in the direction of the returning beam.

If an error δ in any one of the 90° angles is assumed, new direction consines of the normals can be calculated and then the path of the returning beam can be obtained in precisely the same manner as given above.

For example, assume an error δ in the 90° angle between planes 2 and 3, with no other error. For simplicity, assume the unit vectors M_1 and M_2 are unchanged. Then the direction cosines for the unit vector

$$\vec{M}_3 = \frac{1}{\sqrt{3}}\left[\cos\delta + \sin\delta\right]\vec{i} + \frac{1}{\sqrt{6}}\left[\cos\delta + \sin\delta\right]\vec{j} - \frac{1}{\sqrt{2}}\left[\cos\delta - \sin\delta\right]\vec{k} \qquad \text{I(15)}$$

and the return beam S_3 will be given by

$$\vec{S}_3 = -\left[1 - \frac{4}{3}\sin^2\delta\right]\vec{i} + \frac{2\sqrt{2}}{3}\sin^2\delta\,\vec{j} - \frac{2\sqrt{6}}{3}\sin\delta\cos\delta\,\vec{k} \qquad \text{I(16)}$$

If the ray was traced from surface 1 to surface 3, then to surface 2, the return beam will be given by

$$\vec{S}_3 = -\left[1 - \frac{4}{3}\sin^2\delta\right]\vec{i} + \frac{2\sqrt{2}}{3}\sin^2\delta\,\vec{j} + \frac{2\sqrt{6}}{3}\sin\delta\cos\delta\,\vec{k}. \qquad \text{I(17)}$$

Since there are six possible paths of the light rays through the corner cube reflector, there will be six expressions for the return beam $\vec{S}_3$. Thus, the return image will be represented roughly as a six-pointed aberration pattern.

Additional errors in the other 90° angles will produce similar errors in the return beam.

Optical Ray Trace Through the Corner Cube Reflector:

The path of a light ray through the corner cube reflector can be traced quite easily by use of the three reflecting surfaces, equation I(7), the vectorial expression for the light rays, equations I(9, 12, 13 and 14) and the standard expression for a straight line in three dimensional space, which is

$$\frac{x_{i+1}-x_i}{\cos\alpha_i} = \frac{y_{i+1}-y_i}{\cos\beta_i} = \frac{z_{i+1}-z_i}{\cos\gamma_i} \qquad \text{I(18)}$$

The subscript (i) refers to the plane from which the light ray has just been reflected (i + 1) refers to the next following reflecting surface, and the cosines are the direction cosines of the ray and are obtained directly from the equations I(12 or 13). Thus the equation of the ray reflected from plane 1 to plane 2 is given by

$$\frac{x_2-x_1}{\frac{1}{3}} = \frac{y_2-y_1}{\frac{2\sqrt{2}}{3}} \quad \text{with } z_1 = z_2 \qquad \text{I(19)}$$

or

$$\left.\begin{aligned} x_2 &= x_1 + \frac{1}{2\sqrt{2}}(y_2-y_1) \\ y_2 &= y_1 + 2\sqrt{2}(x_2-x_1) \end{aligned}\right\} \qquad \text{I(20)}$$

Similarly, the ray reflected from plane 2 to plane 3 is given by

$$\frac{x_3-x_2}{-\frac{1}{3}} = \frac{y_3-y_2}{\frac{1}{3}\sqrt{2}} = \frac{z_3-z_2}{-\frac{1}{3}\sqrt{6}} \qquad \text{I(21)}$$

or

$$x_3 = x_2 - \frac{1}{\sqrt{2}}(y_3-y_2) \qquad \text{I(22)}$$

$$x_3 = x_2 + \frac{1}{\sqrt{6}}(z_3-z_2) \qquad \text{I(23)}$$

$$y_3 = y_2 - \frac{1}{\sqrt{3}}(z_3-z_2) \qquad \text{I(24)}$$

From I(8b)

$$x_2 + \frac{1}{\sqrt{2}}y_2 = -\frac{1}{2}\sqrt{6}\,z_2 \qquad \text{I(8b')}$$

and from I(22)

$$x_3 + \frac{1}{\sqrt{2}}y_3 = x_2 + \frac{1}{\sqrt{2}}y_2 \qquad \text{I(23')}$$

or

$$x_3 + \frac{1}{\sqrt{2}}y_3 = -\frac{1}{2}\sqrt{6}\,z_2 \qquad \text{I(25)}$$

and from I(8c)

$$X_3 + \frac{1}{\sqrt{2}} Y_3 = + \frac{1}{2}\sqrt{6}\, Z_3 \qquad \text{I(8c')}$$

Thus from I(8c'), and I(25)

$$Z_1 = Z_2 = Z_3 \qquad \text{I(26)}$$

From I(26) and I(23)

$$X_3 - X_2 = \frac{-2}{\sqrt{6}} Z_2 \qquad \text{I(27}$$

and from I(24) and I(26)

$$Y_3 = Y_2 + \frac{2}{\sqrt{3}} Z_2 \qquad \text{I(28)}$$

Also, from I(8a) and I(20)

$$Y_2 = -3Y_1 + 2 \quad 2\sqrt{2 \quad X_2} \qquad \text{I(29)}$$

FromI(8b), I(29) becomes

$$Y_2 = -Y_1 - \frac{2}{3}\sqrt{3}\, Z_1 \qquad \text{I(30)}$$

Substituting I(30) into I(28) with $Z_1 = Z_2$

$$Y_3 = -Y_1 \qquad \text{I(31)}$$

Thus equations I(26) and I(31) demonstrates that the corner cube is a symmetrically reflecting optical system, i.e., the exit aperture is an image of the entrance produced by inversion and reversion.

Unless this symmetry is observed, some of the incident energy on the entrance aperture will miss the third reflection and will be lost. For example, the aperture of a corner cube reflector represented by an equilateral triangle will suffer a 33% light loss.

A corner cube reflector with an entrance aperture represented by a circle or a hexagon will be 100% efficient with no light loss. This statement is only true for incident rays parallel to the system's "optical axis".

Light Path Through the Corner Cube Reflector:

The length of the light path through the corner cube reflector from any plane parallel to the Y-Z plane and distant X_0, a negative quantity, from the Y-Z plane is given by

$$D = (X_1 - X_0) \pm \left[(x_2-x_1)^2 + (y_2-y_1)^2\right]^{\frac{1}{2}} \pm \left[(x_3-x_2)^2 + (y_3-y_2)^2 + (z_3-z_2)^2\right]^{\frac{1}{2}} + (x_3 - x_0)$$

$$= (x_1 + x_3) \pm (y_2 - y_1)\left[\left(\frac{1}{2\sqrt{2}}\right)^2 + 1\right]^{\frac{1}{2}} \pm (z_3 - z_2)\left[\left(\frac{1}{\sqrt{6}}\right)^2 + \left(\frac{1}{\sqrt{3}}\right)^2 + 1\right]^{\frac{1}{2}} - 2x_0$$

$$= (x_1 + x_3) \pm (y_2 - y_1)\left(\frac{9}{8}\right)^{\frac{1}{2}} \pm (2z_3)\left(\frac{9}{6}\right)^{\frac{1}{2}} - 2x_0$$

$$= (x_1 + x_3) \pm (y_2 - y_1)\frac{3}{2\sqrt{2}} \pm (2z_3)\frac{3}{\sqrt{6}} - 2x_0$$

$$= (x_1 + x_3) \pm (y_2 - y_1)\frac{3}{2\sqrt{2}} \pm z_3\sqrt{6} - 2x_0 \qquad \text{I(32)}$$

with $x_3 = -\frac{1}{\sqrt{2}} y_3 + \frac{1}{2}\sqrt{6}\, z_3 = \frac{1}{\sqrt{2}} y_1 - \frac{1}{2}\sqrt{6}\, z_1$

$(y_2 - y_1) > 0$ and $z_3 < 0$

equation I(32) reduces to

$$D = x_1 - \sqrt{2}\, y_1 - 2x_0 \qquad \text{I(33)}$$

But, $x_1 - \sqrt{2}\, y_1 = 0$ defines plane 1, therefore,

$$D = -2x_0 \quad (x_0 \text{ is negative}) \qquad \text{I(34)}$$

Thus the distance through the corner cube is invariant with X, Y, and Z.

APPENDIX II

OPTICAL PATH OF OFF-AXIS RAYS THROUGH A CORNER CUBE REFLECTOR

It was shown in Appendix I how a ray of light can be traced through a corner cube reflector by use of the equations of the three planes and vector notation.

The same techniques can be used for tracing rays making an angle α_0 with the "optical axis" of the corner cube reflector. The expression for the incoming ray is given by

$$\vec{S}_0 = l_0 \vec{i} + m_0 \vec{j} + n_0 \vec{k} \qquad \text{II(1)}$$

where $l_0, m_0, n_0,$ is the standard notation for the three direction cosines.

Since there are six possible paths for the light rays to traverse in passing through and then out of the corner cube reflector, there will be six sets of equations to describe this passage. For example, $1 \rightarrow 2 \rightarrow 3$ represents the case where the light ray incident on plane 1 is reflected from plane 2 and then to plane 3, where it is reflected back to the source.

The six possible paths the light rays can follow are as follows

$$\left.\begin{array}{ll} 1 \rightarrow 2 \rightarrow 3 & \text{II(2a)} \\ 1 \rightarrow 3 \rightarrow 2 & \text{II(2b)} \\ 2 \rightarrow 3 \rightarrow 1 & \text{II(2c)} \\ 2 \rightarrow 1 \rightarrow 3 & \text{II(2d)} \\ 3 \rightarrow 1 \rightarrow 2 & \text{II(2e)} \\ 3 \rightarrow 2 \rightarrow 1 & \text{II(2f)} \end{array}\right\} \text{II(2)}$$

In all cases, the entrant ray is given by II(1) and the exit ray is given by

$$\vec{S}_3 = -l_0 \vec{i} - m_0 \vec{j} - n_0 \vec{k} \qquad \text{II}(3)$$

which is the negative of II(1).

The vector equations of the first and the second reflections in the various possible paths given by II(2) are summarized as follows:

II (2a) $1 \rightarrow 2 \rightarrow 3$

$$\vec{S}_1 = \left[\tfrac{1}{3} l_0 + \tfrac{2}{3}\sqrt{2}\, m_0\right]\vec{i} + \left[\tfrac{2}{3}\sqrt{2}\, l_0 - \tfrac{1}{3} m_0\right]\vec{j} + n_0 \vec{k} \qquad \text{II (4a)}$$

$$\vec{S}_2 = \left[-\tfrac{1}{3} l_0 + \tfrac{1}{3}\sqrt{2}\, m_0 - \tfrac{2}{\sqrt{6}} n_0\right]\vec{i} + \left[\tfrac{1}{3}\sqrt{2}\, l_0 - \tfrac{2}{3} m_0 - \tfrac{1}{\sqrt{3}} n_0\right]\vec{j} - \left[\tfrac{1}{\sqrt{6}} l_0 + \tfrac{1}{\sqrt{3}} m_0\right]\vec{k} \qquad \text{II(4b)}$$

II (2b) $1 \rightarrow 3 \rightarrow 2$

$\vec{S}_1$ is the same as II(4a)

$$\vec{S}_2 = \left[-\tfrac{1}{3} l_0 + \tfrac{1}{3}\sqrt{2}\, m_0 + \tfrac{1}{3}\sqrt{6}\, n_0\right]\vec{i} + \left[\tfrac{1}{3}\sqrt{2}\, l_0 - \tfrac{2}{3} m_0 + \tfrac{1}{3}\sqrt{3}\, n_0\right]\vec{j} \qquad \text{II(5a)}$$
$$+ \left[\tfrac{1}{3}\sqrt{6}\, l_0 + \tfrac{1}{3}\sqrt{3}\, m_0\right]\vec{k}$$

II(5b)

II(2c) $2 \rightarrow 3 \rightarrow 1$

$$\vec{S}_1 = \left[\tfrac{1}{3} l_0 - \tfrac{1}{3}\sqrt{2}\, m_0 - \tfrac{1}{3}\sqrt{6}\, n_0\right]\vec{i} + \left[-\tfrac{1}{3}\sqrt{2}\, l_0 + \tfrac{2}{3} m_0 - \tfrac{1}{3}\sqrt{3}\, n_0\right]\vec{j} - \left[\tfrac{1}{3}\sqrt{6}\, l_0 + \tfrac{1}{3}\sqrt{3}\, m_0\right]\vec{k} \qquad \text{II(6a)}$$

$$\vec{S}_2 = \left[-\tfrac{1}{3} l_0 - \tfrac{2}{3}\sqrt{2}\, m_0\right]\vec{i} + \left[-\tfrac{2}{3}\sqrt{2}\, l_0 + \tfrac{1}{3} m_0\right]\vec{j} - n_0 \vec{k} \qquad \text{II(6b)}$$

II(2d) $2 \rightarrow 1 \rightarrow 3$

$\vec{S}_1$ is the same as II(6a) II(7a)

$$\vec{S}_2 = \left[-\tfrac{1}{3} l_0 + \tfrac{1}{3}\sqrt{2}\, m_0 - \tfrac{1}{3}\sqrt{6}\, n_0\right]\vec{i} + \left[\tfrac{1}{3}\sqrt{2}\, l_0 - \tfrac{2}{3} m_0 - \tfrac{1}{3}\sqrt{3}\, n_0\right]\vec{j} - \left[\tfrac{1}{3}\sqrt{6}\, l_0 + \tfrac{1}{3}\sqrt{3}\, m_0\right]\vec{k} \qquad \text{II(7b)}$$

II2e) $3 \rightarrow 1 \rightarrow 2$

$$\vec{S}_1 = \left[\tfrac{1}{3} l_0 - \tfrac{1}{3}\sqrt{2}\, m_0 + \tfrac{1}{3}\sqrt{6}\, n_0\right]\vec{i} + \left[-\tfrac{1}{3}\sqrt{2}\, l_0 + \tfrac{2}{3} m_0 + \tfrac{1}{3}\sqrt{3}\, n_0\right]\vec{j} + \left[\tfrac{1}{3}\sqrt{6}\, l_0 + \tfrac{1}{3}\sqrt{3}\, m_0\right]\vec{k} \qquad \text{II(8a)}$$

$$\vec{S}_2 = \left[-\tfrac{1}{3} l_0 + \tfrac{1}{3}\sqrt{2}\, m_0 + \tfrac{1}{3}\sqrt{6}\, n_0\right]\vec{i} + \left[\tfrac{1}{3}\sqrt{2}\, l_0 - \tfrac{2}{3} m_0 + \tfrac{1}{3}\sqrt{3}\, n_0\right]\vec{j} + \left[\tfrac{1}{3}\sqrt{6}\, l_0 + \tfrac{1}{3}\sqrt{3}\, m_0\right]\vec{k} \qquad \text{II(8b)}$$

II(2f) $3 \rightarrow 2 \rightarrow 1$

$\vec{S}_1$ is the same as II(8a) II(9a)

$$\vec{S}_2 = \left[-\tfrac{1}{3} l_0 - \tfrac{2\sqrt{2}}{3} m_0\right]\vec{i} + \left[-\tfrac{2\sqrt{2}}{3} l_0 + \tfrac{1}{3} m_0\right]\vec{j} - n_0 \vec{k} \qquad \text{II(9b)}$$

By the use of equations II(4a) through II(9b) the three expressions for the three planes, and the standard expression for a directed straight line in three dimensional space, it is possible to trace any possible oriented ray through a triple reflecting corner cube.

Expression for the path of a ray through the corner cube were derived and are summarized as follows. The six possible paths given by II (2) are indicated.

II (2a) $1 \rightarrow 2 \rightarrow 3$ (Y_1 and Z_1 chosen)

$$\left.\begin{aligned} z_2 &= a_{12} z_1 + b_{12} y_1 \\ y_2 &= A_{12} z_1 + B_{12} y_1 \\ y_3 &= y_2 + C_{12} z_2 \\ z_3 &= D_{12} z_2 \end{aligned}\right\} \qquad \text{II (10)}$$

II(2b) $1 \rightarrow 3 \rightarrow 2$ (Y_1 and Z_1 chosen)

$$\left.\begin{aligned} z_3 &= a_{13} z_1 + b_{13} y_1 \\ y_3 &= A_{13} z_1 + B_{13} y_1 \\ y_2 &= y_3 + C_{13} z_3 \\ z_2 &= D_{13} z_3 \end{aligned}\right\} \qquad \text{II(11)}$$

II(2c) $2 \rightarrow 3 \rightarrow 1$ (Y_2 and Z_2 chosen)

$$\left.\begin{aligned} z_3 &= a_{23} z_2 \\ y_3 &= y_2 + b_{23} z_2 \\ y_1 &= A_{23} y_3 + B_{23} z_3 \\ z_1 &= C_{23} y_3 + D_{23} z_3 \end{aligned}\right\} \qquad \text{II (12)}$$

II(2d) $2 \rightarrow 1 \rightarrow 3$ (Y_2 and Z_2 chosen)

$$\left.\begin{aligned} z_1 &= a_{21} z_2 + b_{21} y_2 \\ y_1 &= A_{21} z_2 + B_{21} y_2 \\ y_3 &= C_{21} z_1 + D_{21} y_1 \\ z_3 &= E_{21} y_1 + F_{21} z_1 \end{aligned}\right\} \qquad \text{II(13)}$$

II (2e) $3 \rightarrow 1 \rightarrow 2$ (Y_3 and Z_3 chosen)

$$\left.\begin{aligned} y_1 &= a_{31} y_3 + b_{31} z_3 \\ z_1 &= A_{31} y_3 + B_{31} z_3 \\ y_2 &= C_{31} y_1 + D_{31} z_1 \\ z_2 &= E_{31} y_1 + F_{31} z_1 \end{aligned}\right\} \qquad \text{II(14)}$$

II (2f) $3 \rightarrow 2 \rightarrow 1$ (Y_3 and Z_3 chosen)

$$\left.\begin{aligned} z_2 &= a_{32} z_3 \\ y_2 &= y_3 + b_{32} z_3 \\ y_1 &= A_{32} y_2 + B_{32} z_2 \\ z_1 &= C_{32} y_2 + D_{32} z_2 \end{aligned}\right\} \qquad \text{II(15)}$$

The various constants given in equations II(10) through II(15) are given as follows:

$1 \rightarrow 2 \rightarrow 3$

$$a_{12} = \frac{\sqrt{2}\,l_0 + m_0}{\sqrt{2}\,l_0 + m_0 + \sqrt{3}\,m_0}$$

$$b_{12} = \sqrt{3}\,(a_{12} - 1)$$

$$A_{12} = -\frac{1}{\sqrt{3}}\,\frac{2\sqrt{2}\,l_0 - m_0}{\sqrt{2}\,l_0 + m_0 + \sqrt{3}\,m_0}$$

$$B_{12} = \frac{-\sqrt{2}\,l_0 + 2m_0 + \sqrt{3}\,m_0}{\sqrt{2}\,l_0 + m_0 + \sqrt{3}\,m_0}$$

$$C_{12} = \frac{2}{\sqrt{3}}\,\frac{\sqrt{2}\,l_0 - 2m_0 - \sqrt{3}\,m_0}{\sqrt{2}\,l_0 + m_0 - \sqrt{3}\,m_0}$$

$$D_{12} = -\frac{\sqrt{2}\,l_0 + m_0 + \sqrt{3}\,m_0}{\sqrt{2}\,l_0 + m_0 - \sqrt{3}\,m_0}$$

$1 \rightarrow 3 \rightarrow 2$

$$a_{13} = \frac{\sqrt{2}\,l_0 + m_0}{\sqrt{2}\,l_0 + m_0 - \sqrt{3}\,m_0}$$

$$b_{13} = \sqrt{3}\,(1 - a_{13})$$

$$A_{13} = \frac{1}{\sqrt{3}}\,\frac{2\sqrt{2}\,l_0 - m_0}{\sqrt{2}\,l_0 + m_0 - \sqrt{3}\,m_0}$$

$$B_{13} = \frac{-\sqrt{2}\,l_0 + 2m_0 - \sqrt{3}\,m_0}{\sqrt{2}\,l_0 + m_0 - \sqrt{3}\,m_0}$$

$$C_{13} = -\frac{2}{\sqrt{3}}\,\frac{\sqrt{2}\,l_0 - 2m_0 + \sqrt{3}\,m_0}{\sqrt{2}\,l_0 + m_0 + \sqrt{3}\,m_0}$$

$$D_{13} = 1/D_{12}$$

$2 \rightarrow 3 \rightarrow 1$

$$a_{23} = D_{12}$$

$$b_{23} = \frac{2}{\sqrt{3}}\,C_{13}$$

$$A_{23} = \frac{\sqrt{2}\,l_0 + m_0}{\sqrt{2}\,l_0 - 2m_0}$$

$$B_{23} = \frac{1}{\sqrt{3}}\,\frac{2\sqrt{2}\,l_0 - m_0}{\sqrt{2}\,l_0 - 2m_0}$$

$$C_{23} = \frac{-3m_0}{\sqrt{2}\,l_0 - 2m_0}$$

$$D_{23} = 1 - \frac{1}{\sqrt{3}}\,C_{23}$$

$2 \rightarrow 1 \rightarrow 3$

$$a_{21} = 1 + A_{23}$$

$$b_{21} = \sqrt{3}\,A_{23}$$

$$A_{21} = \frac{1}{3}C_{23} - \frac{1}{\sqrt{3}}$$

$$B_{21} = \frac{1}{\sqrt{3}}\,C_{23}$$

$$C_{21} = \frac{1}{\sqrt{3}}\left(1 - \frac{m_0}{\sqrt{2}\,l_0 - m_0 - \sqrt{3}\,m_0}\right)$$

$$D_{21} = 1 - \sqrt{3}\,C_{21}$$

$$E_{21} = \sqrt{3}\,\frac{\sqrt{2}\,l_0 - m_0}{\sqrt{2}\,l_0 - m_0 - \sqrt{3}\,m_0}$$

$$F_{21} = 1 - \frac{1}{\sqrt{3}}\,E_{21}$$

$3 \rightarrow 1 \rightarrow 2$

$$a_{31} = -B_{21}$$

$$b_{31} = \frac{1}{\sqrt{3}}(1 - a_{31})$$

$$A_{31} = -\sqrt{3}\,A_{23}$$

$$B_{31} = a_{21}$$

$$C_{31} = 1 + \frac{1}{2}\sqrt{3}\,C_{13}$$

$$D_{31} = \frac{1}{2}C_{13}$$

$$E_{21} = -\sqrt{3}\,a_{12}$$

$$F_{21} = 1 - a_{12}$$

$3 \rightarrow 2 \rightarrow 1$

$$a_{32} = D_{13}$$

$$b_{32} = -\frac{2}{\sqrt{3}}\,B_{12}$$

$$A_{32} = A_{23}$$

$$B_{32} = -B_{23}$$

$$C_{32} = C_{23}$$

$$D_{32} = 1 + \frac{1}{\sqrt{3}}\,C_{32}$$

A program for the Autonetics (NAA) Recomp II computer was written which would compute all the constants used in equation II(10) through II(15). The values of α_o was varied from $\alpha_o = 5^\circ$ to $\alpha_o = 25^\circ$ in 5° steps. The plane containing the x-axis and the light ray passing through the origin was rotated in 5 degree steps from 0° to 180°, this rotation being designated Δ.

Because of the magnitude of the computation and printout time, the program was run only for the case $\alpha_o = 20^\circ$. These constants were used in a few cases to compute the utility area of the corner cube reflector used off-axis.

From the predetermined values of α_o and Δ, the direction cosines cos β_o and cos α_o were computed from the following

$$\left.\begin{aligned} m_o &= \sin \alpha_o \cos \Delta \\ n_o &= -\sin \alpha_o \sin \Delta \end{aligned}\right\} \qquad \text{II(16)}$$

The negative sign in II(16) is required because of the choice of rotating counter clockwise and m_o positive for $\Delta = 0$, see Figure II-1.

The choice of $\alpha_o = 20^\circ$ was suggested by the request in the contract that the effective modulating area be 100 square centimeters at 20° off-axis. A few values of Δ were chosen and the useable aperture area was calculated. In a few cases the modulating area was completely used. However, as increased beyond 20° the percentage of the modulating area decreased. At $\Delta = 0^\circ$ and 15°, see Figures II-2 and II-3, the modulating area was used 100%. At $\Delta = 60^\circ$ and 180, see Figures II-4 and II-5, the modulating area used decreased to 76.3% and 24.4%.

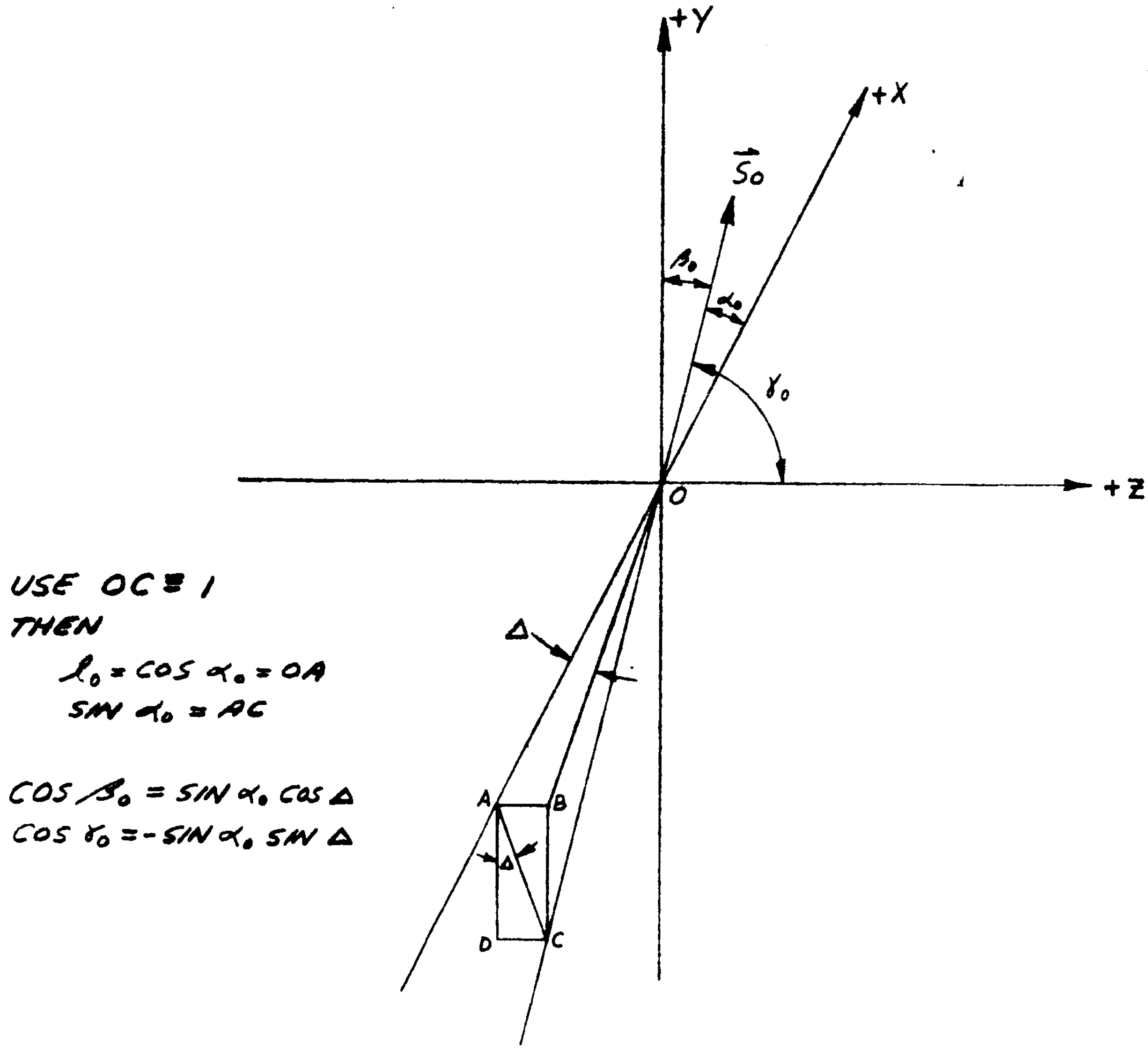

RELATIONSHIP FOR DERIVING DIRECTION COSINES

FOR

OFF-AXIS RADIATION

FIGURE II-1

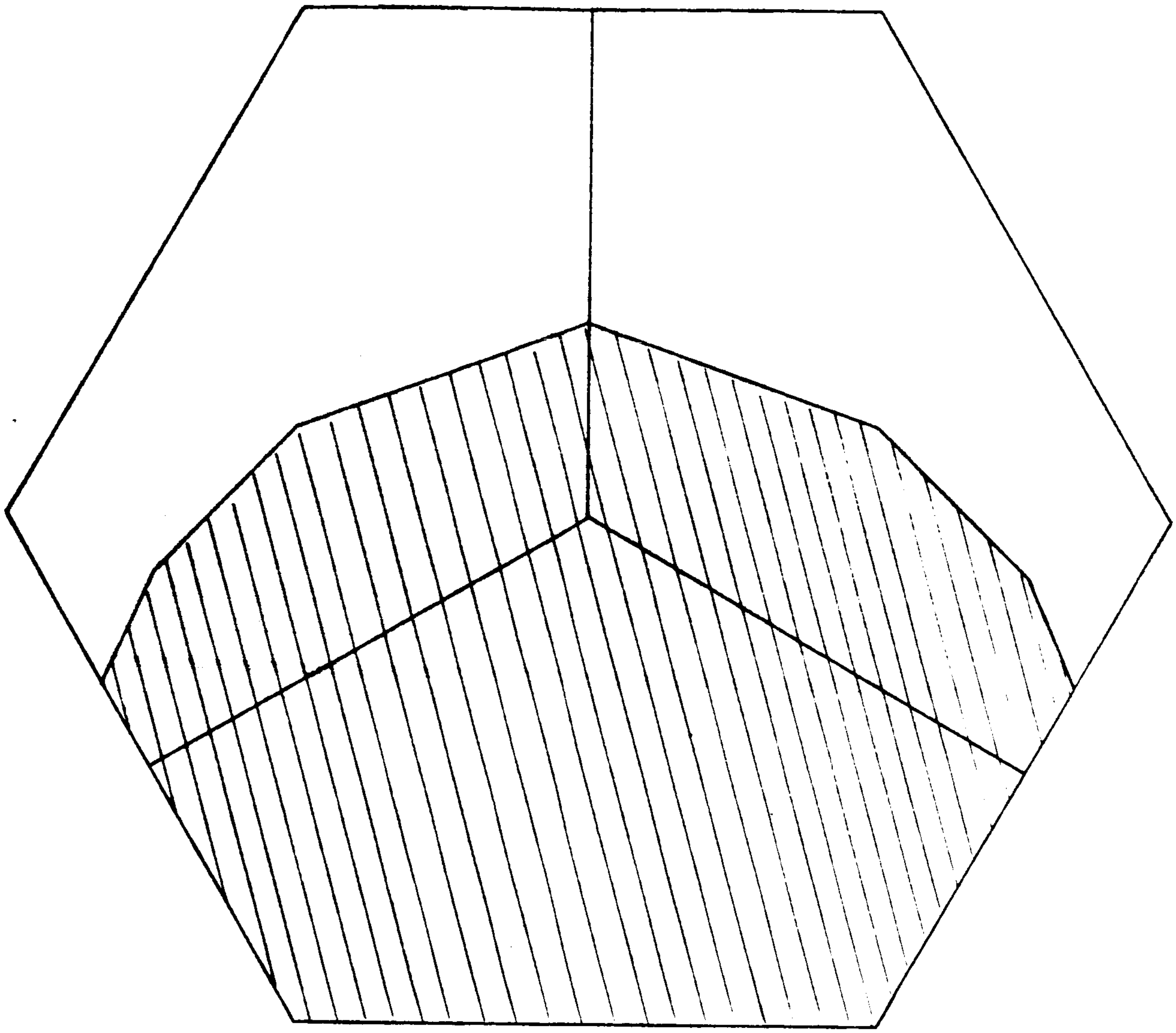

AREA UTILIZED FOR $\alpha_o = 20°, \beta_1 = +70°, \gamma_o = 90°$ ($\Delta = 0$)
EFFICIENCY = 58.0%
MODULATING AREA USED = 100%

FIGURE II-2

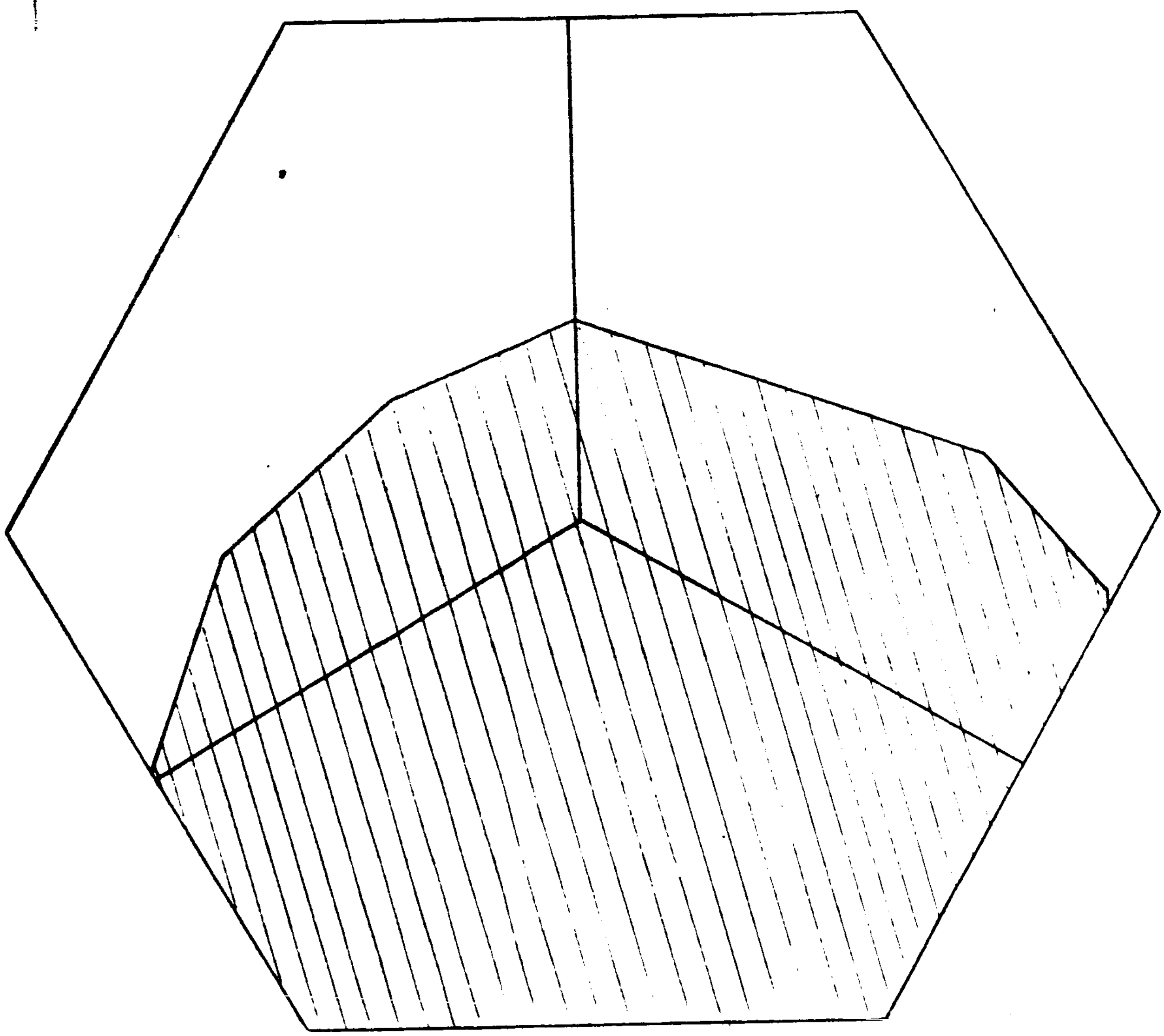

AREA UTILIZED FOR $\alpha_0 = 20°$, $\beta_0 = 70.7°$, $\gamma_0 = 95.1°$ ($\Delta = 15°$)

EFFICIENCY = 57.2%

MODULATING AREA USED = 100%

FIGURE II-3

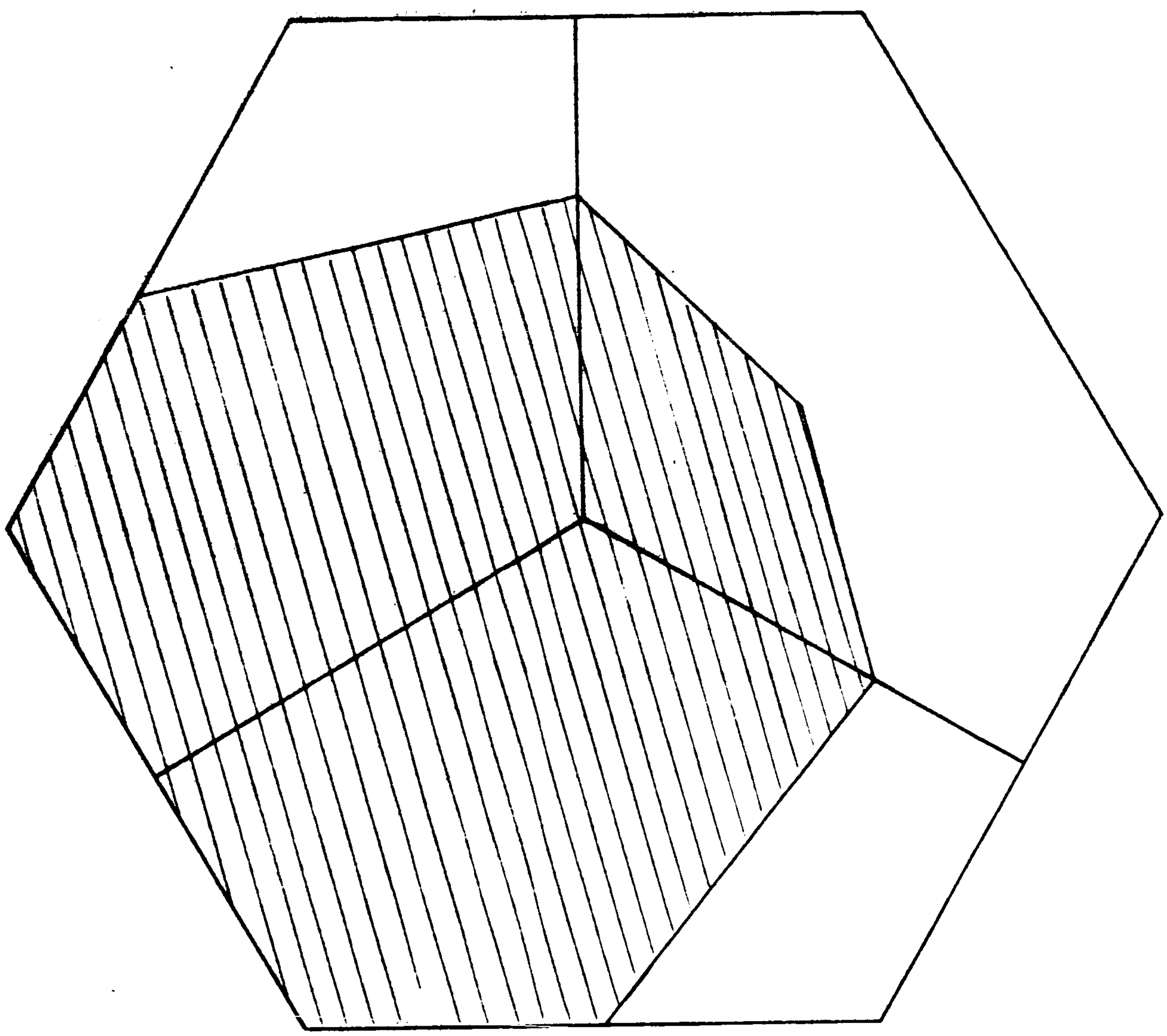

AREA UTILIZED FOR $\alpha_0 = 20°$, $\beta_0 = 99.8°$, $\gamma_0 = 107.2°$ ($\Delta = -60°$)

EFFICIENCY = 57.5%

MODULATING AREA USED = 76.3%

FIGURE II-4

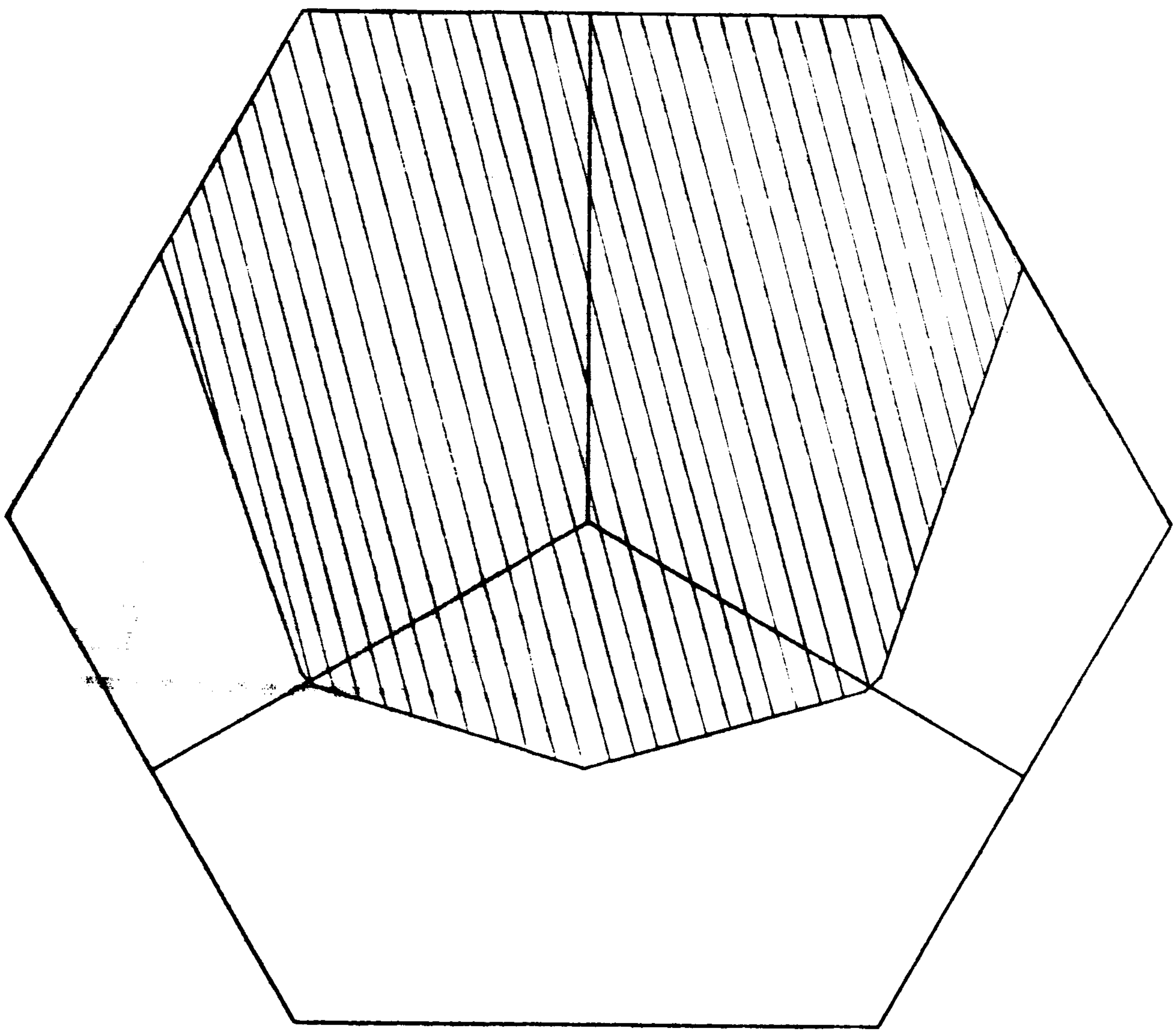

AREA UTILIZED FOR $_{o} = 20°$, $_{o} = 70°$, $_{o} = 90°$ ($= 180°$)

EFFICIENCY = 56.0%

MODULATING AREA USED = 24.4%

FIGURE II-5

APPENDIX III*

ENERGY DISTRIBUTION IN THE DIFFRACTION PATTERN FROM A CIRCULAR APERTURE

A quantity of prime importance in discussions concerning laser light uses and capabilities is the peak light intensity for a beam collimated by a uniformly illuminated circular aperture. Mathematically this quantity is expressed as the total laser power divided by π times the square of the beam spread angle, i.e.,

$$\text{Peak Intensity} = \frac{\text{Power}}{\pi\,(\text{beam spread angle})^2}$$

Much confusion has resulted in the use of this quantity due to the various definitions of "beam spread angle." We will call this beam spread angle the "power half angle" to distinguish it from other measures of the beam spread, and denote it by θ_{PHA}. In Appendix B of Technical Memorandum #76, it is shown that

$$\theta_{PHA} = \frac{2}{\pi}\left(\frac{\lambda}{D}\right) = .636\,\frac{\lambda}{D}$$

where D is the diameter of the collimating aperture.

Two other quantities which are often used to describe the beam spread angle are the half angle of the Airy dark ring's angular diameter, i.e., the peak to zero power angle denoted by θ_o, and the half-power half angle, i.e., the angle between peak and half-peak intensity denoted by $\theta_{\frac{1}{2}}$. Figure III-1 illustrates the physical significance of these two angles. It is easy to show that

$$\theta_{\frac{1}{2}} \simeq .51\,\frac{\lambda}{D}$$

$$\theta_o = 1.22\,\frac{\lambda}{D}$$

*Extracted from N.A.A. Electro-Optical Laboratory Technical Memorandum #149

The dependence of θ_{PHA}, $\theta_{\frac{1}{2}}$, and θ_o on diameter D is shown in Figure III-2.

The intensity of a collimated beam at various angles is given by the dependence

$$\frac{I(\theta)}{I_o} = \left\{ \frac{2J_1\left(\frac{\pi D}{\lambda}\theta\right)}{\frac{\pi D}{\lambda}\theta} \right\}^2$$

This dependence is plotted in Figure III-3 for D = ½, 1, and 2 cm, with λ = 6328 Å.

A coherent light beam brought to focus by a diffraction limited lens always exhibits an interference pattern.

The central portion or Airy disc contains approximately 84% of the incident light.

Figure III-4, represents a plot of the distribution of the power in the diffraction pattern expressed as the percentage of the power in a cone whose half angle is θ. The angular dimension is normalized to be unity at the first Airy dark ring, i.e., at 1.22 λ/D. At this point, the percentage power is 84%.

Figure III-1

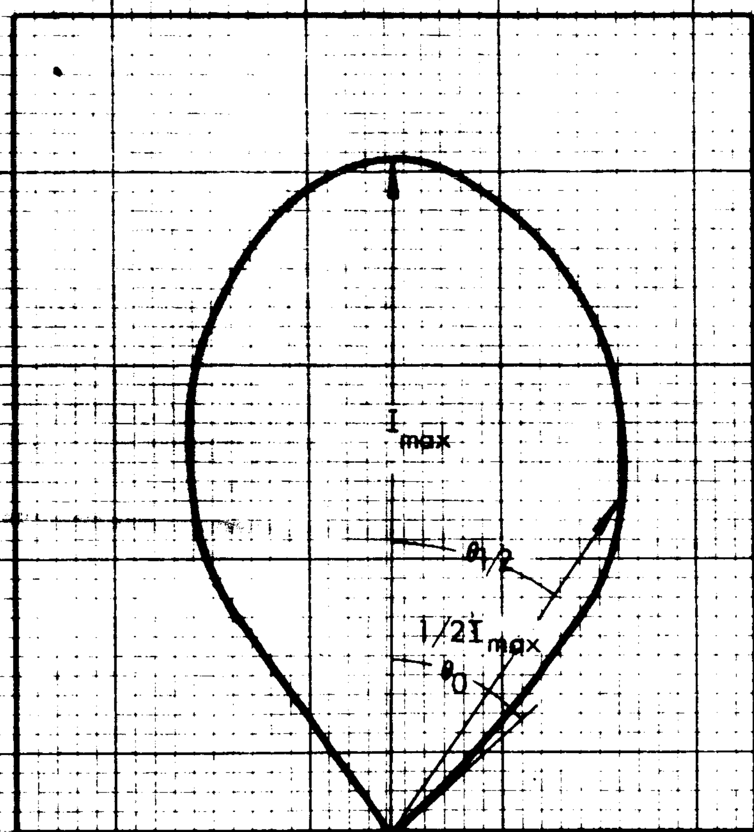

Figure III-2

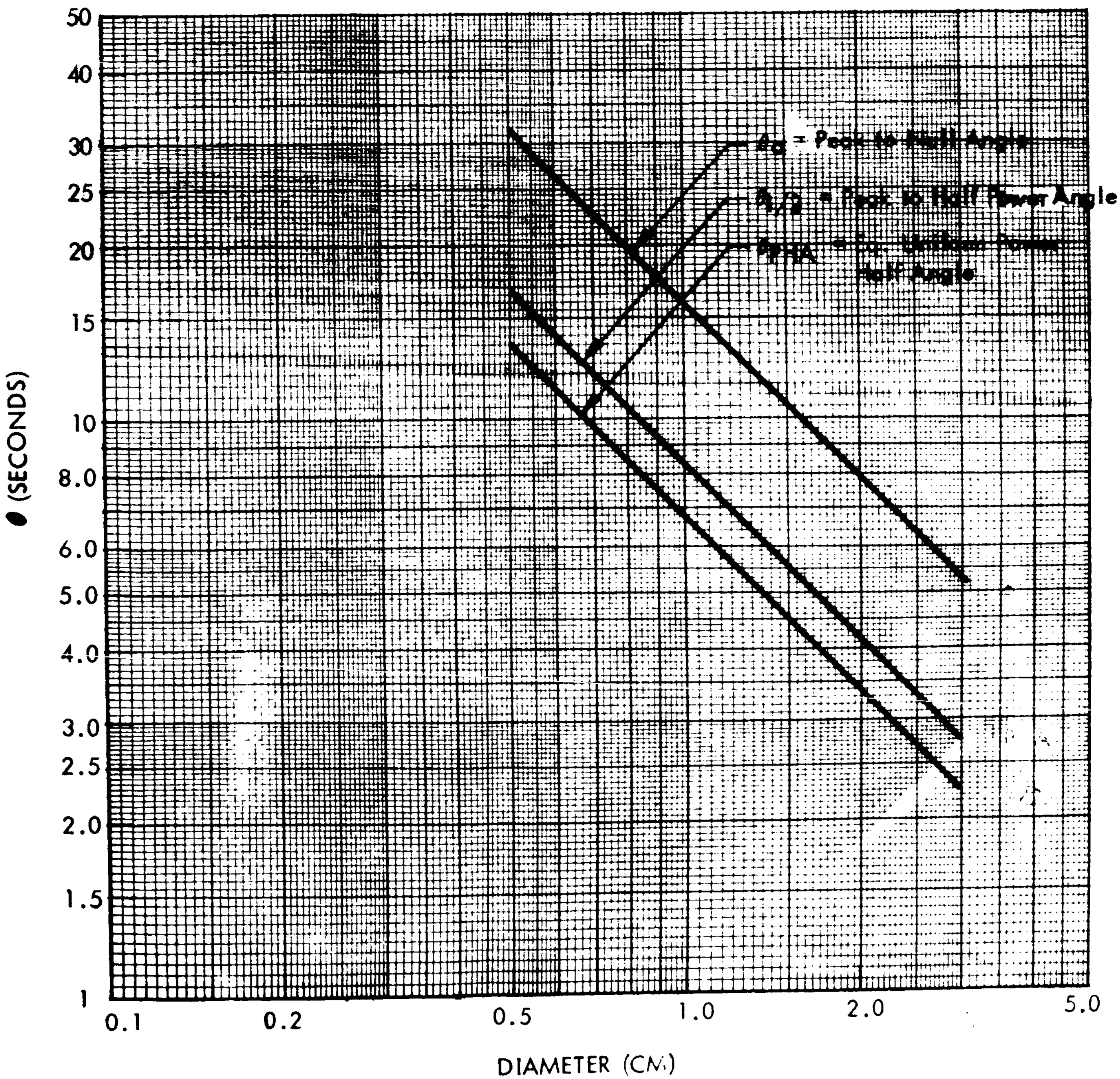
50
40
30
25
20
15
10
8.0
6.0
5.0
4.0
3.0
2.5
2.0
1.5
1
(SECONDS)
0.1
0.2
0.5
1.0
2.0
5.0
DIAMETER (CM)

Figure III-3

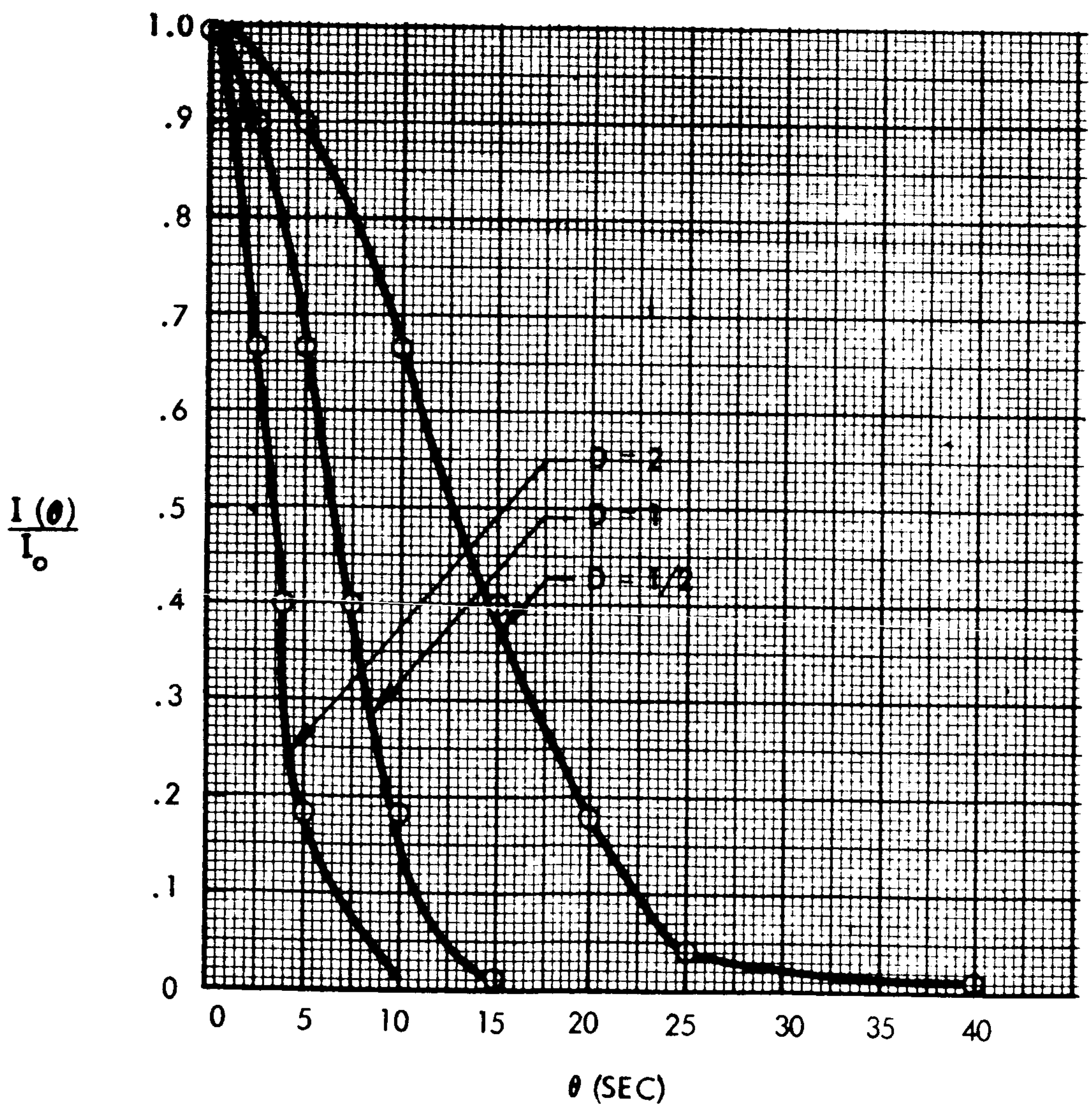
1.0
.9
.8
.7
.6
.5
.4
.3
.2
.1
0
$\frac{I(\theta)}{I_o}$
D = 2
D = 1
D = 1/2
0
5
10
15
20
25
30
35
40
θ (SEC)

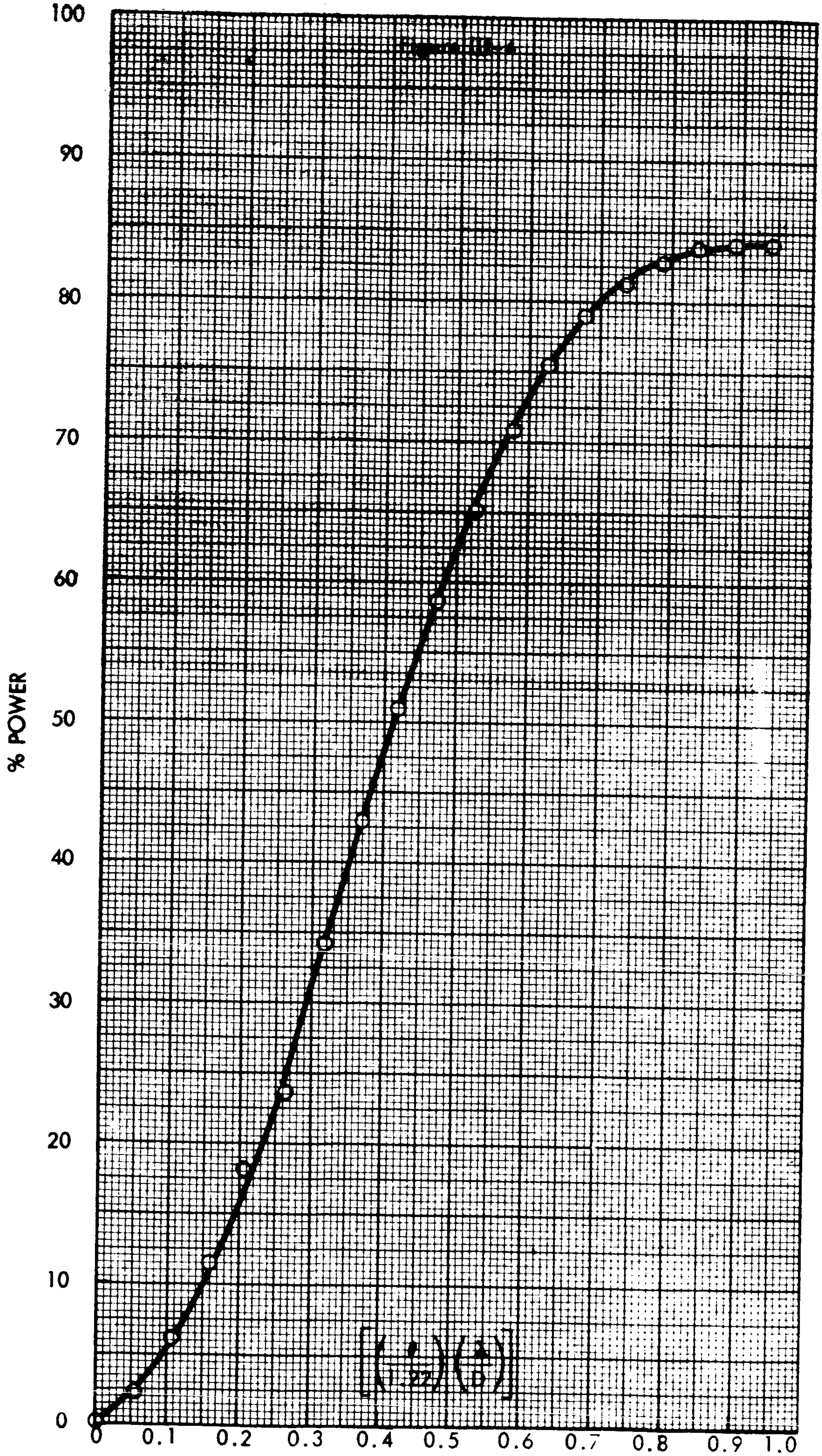
% POWER
100
90
80
70
60
50
40
30
20
10
0
0
0.1
0.2
0.3
0.4
0.5
0.6
0.7
0.8
0.9
1.0

APPENDIX IV

MIROS SYSTEM PERFORMANCE ANALYSIS

SPACEBORNE RETROMODULATOR

The assumed system comprises a ground-based CW laser of 100 milliwatts output, and a spaceborne retromodulator having an effective modulating reflective area of 100 cm^2 (within 20 degrees of its axis of symmetry), transmitting to a ground-based receiver at the laser location. The receiver is considered to be the NASA 24-inch telescope and/or the NASA 12-inch autotracking theodolite. See Figure IV-1.

The symbols and definitions used in the NASA Statement of Work (Exhibit A, Pages 5 and 6, para. 1.3.2) are used in the analysis which follows. Additional symbols are defined where used. Several parameters were assumed for the NASA telescope; the results of the analysis may be adjusted if these assumptions are at variance with the actual case.

The power collected by the ground-based receiver after reflection from the MIROS retroreflector is

$$W_r = \frac{P_r A_c A_r \tau^2 \rho_m}{\pi^2 \theta_r^2 \theta_c^2 R^4}$$

The signal power at the receiver also can be written

$$W_r = \frac{m W_c A_r \tau \rho}{\pi \theta_c^2 R^2}$$

and the noise power at the receiver is

$$W_s = \left[2\eta \left(\frac{W_r}{m} + W_b \right) e \Delta f \right]^{1/2}$$

where

$$W_b = B_a A_r (\Delta\lambda_r) \pi (\phi_r)^2$$

and

m = depth of modulation of the reflecting membrane

η = quantum efficiency of receiver detector

MIROS SYSTEM BLOCK DIAGRAM

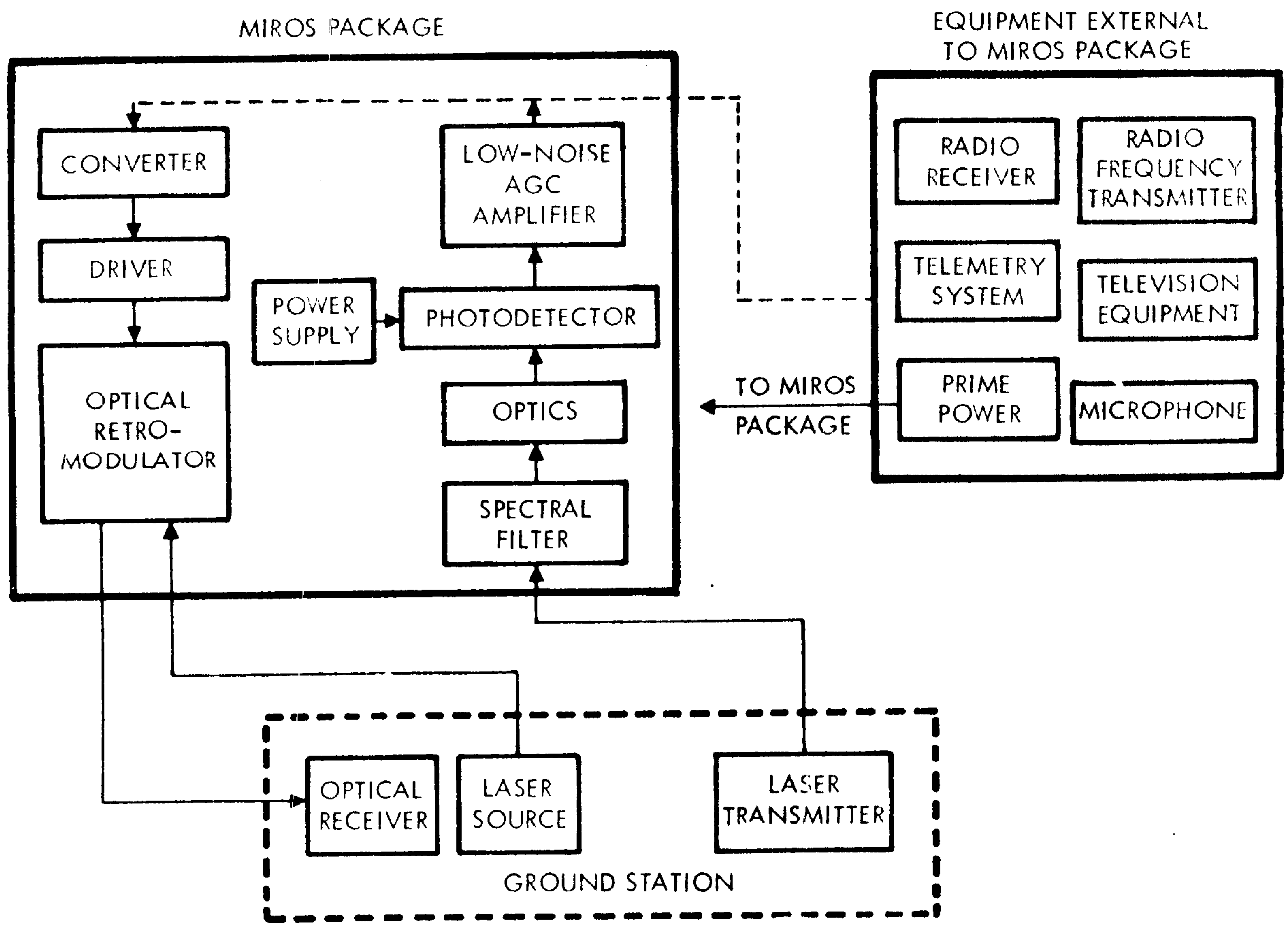

FIGURE IV-1

Δf = electrical bandwidth

B_a = brightness of sky background

The following values are assumed:

$\tau = 0.72$ (including 0.9 for receiving telescope optics) for a path 30 degrees from zenith

$\rho = 0.73$ (0.9 per surface)

$m = 0.50$

$\Delta f = 20$ Kc

$\eta = 2.6 \times 10^{-2}$ amp/watt (S-20 at 0.63 micron)

$A_c = 100 \text{ cm}^2$

$P_r = 100$ milliwatts

$\theta_c = \theta_r = 10$ sec (4.88×10^{-5} radians)

$\Phi_r = 2 \times 10^{-4}$ radians (NASA telescope assumed f/8, 1-mm stop)

$A_r = 0.292 \text{ m}^2$ (24-inch diameter)

$B_a = 19$ watts/m^2 ster-micron (daylight sky)

$\Delta\lambda_r = 500\text{Å}, 100\text{Å}$

$e = 1.6 \times 10^{-19}$ coulombs.

Using these assumed values, operating range versus signal-to-noise ratio was calculated for both night and day background conditions. (The calculations for daytime background conditions also were made for two different spectral filters to determine the effect of filter bandwidth.) The results are presented in Figure IV-2. For S/N = 0 db, it is seen that a 1250-km range can be obtained at night and 390 km in the daytime, using a filter with a spectral bandwidth of 100Å.

NOTE: Values for B_a and B_d have been taken from D. S. Bayley, "Technical Note on Optical Communication," ASTIA Document No. AD 261 553.

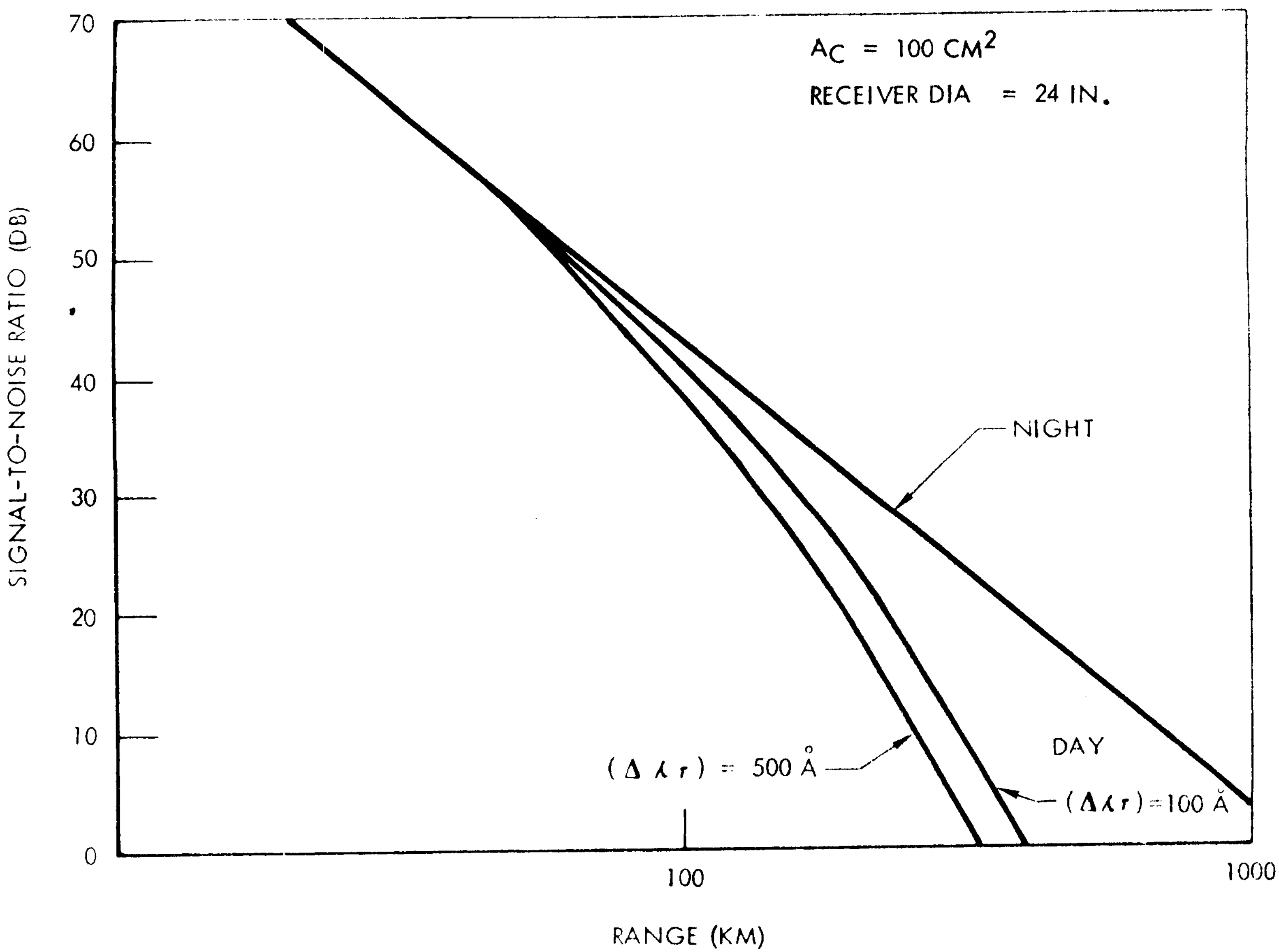

A_C = 100 CM^2
RECEIVER DIA = 24 IN.
NIGHT
DAY
$(\Delta\lambda r) = 500$ Å
$(\Delta\lambda r) = 100$ Å
SIGNAL-TO-NOISE RATIO (DB)
70
60
50
40
30
20
10
0
100
1000
RANGE (KM)

Figure IV-2

Since range is proportional to the fourth root of retromodulator area, if A_c were increased to one square meter (a factor of 100), range would be increased by a factor of about 3.2. The range would then be 1240 km and 4000 km for day and night operation, respectively.

GROUND-BASED RETROMODULATOR

If the retromodulator is ground-based, the range is calculated using atmospheric transmission over a horizontal or ground path. (This case is included because it is pertinent to probable field testing of the MIROS package.) The atmospheric transmission τ is 0.03 ($\Delta\lambda_r$ = 100Å). At night the range is 75 km, and during the daytime range is 40 km, using the 24-inch telescope as the receiver.

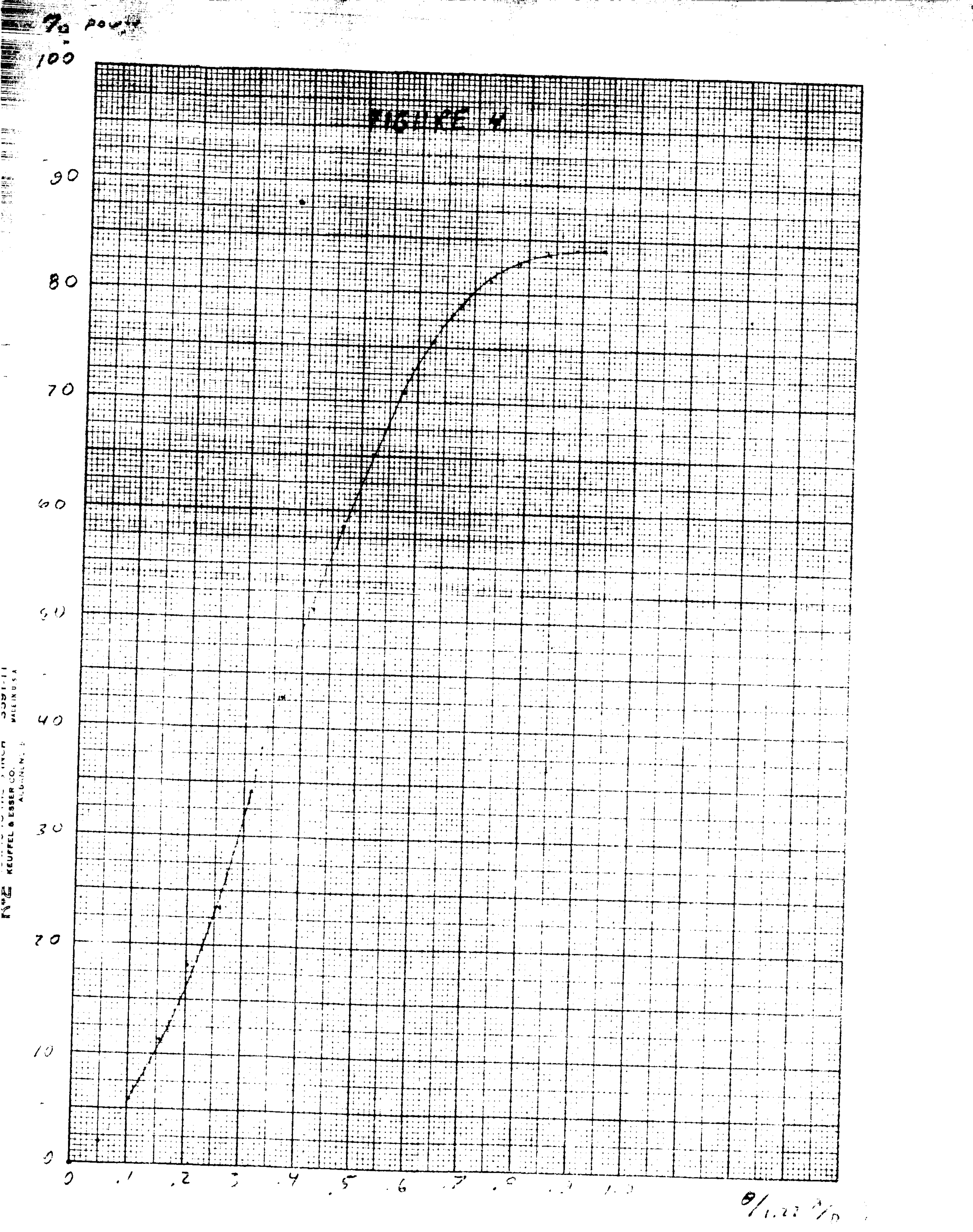
FIGURE 4
% power
100
90
80
70
60
40
30
20
10
0
0
.1
.2
.4
.5
.6
.7
KEUFFEL & ESSER CO.

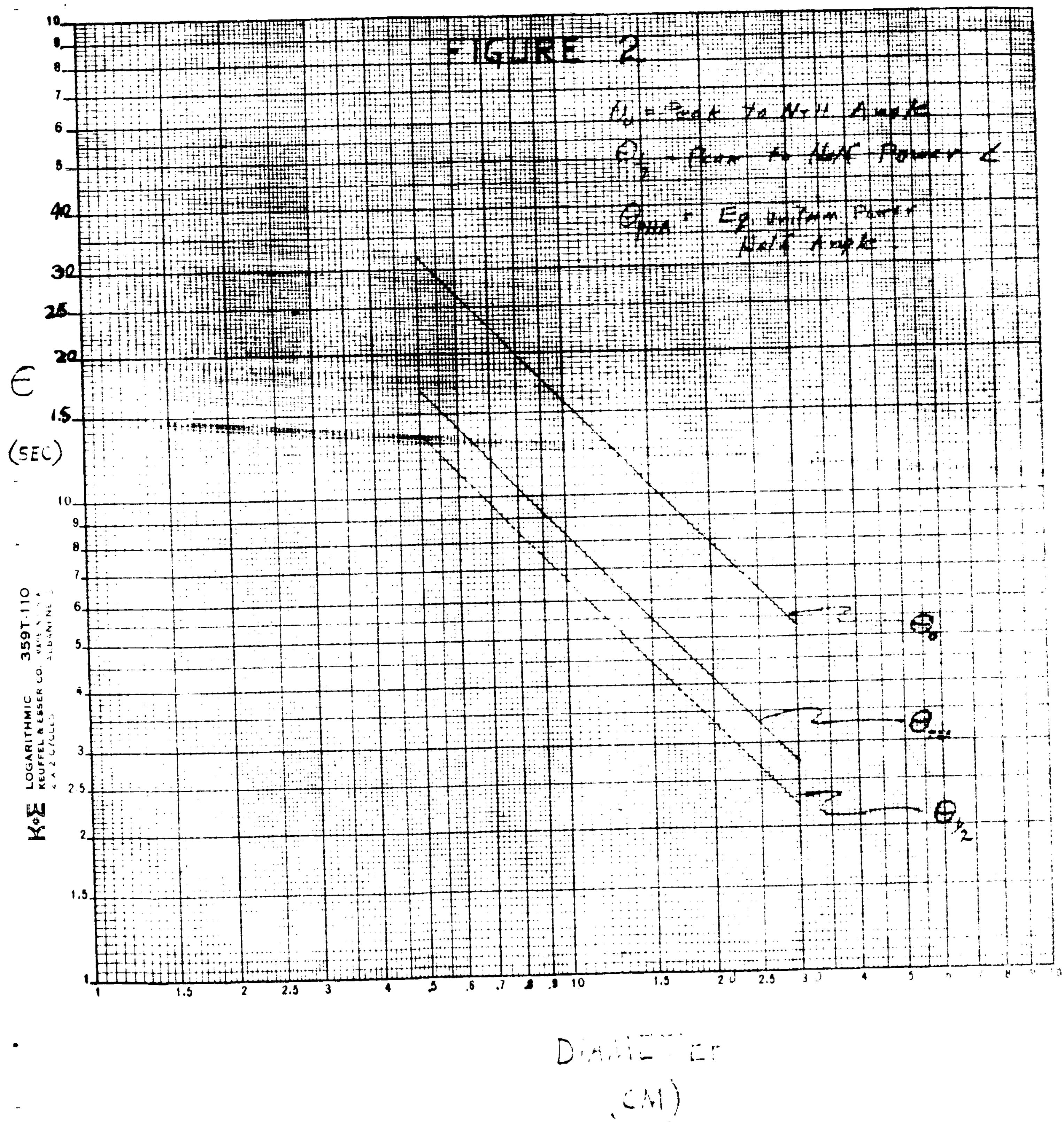
FIGURE 2
Θ
(SEC)
DIAMETER
(CM)
K+E LOGARITHMIC 359T-110
KEUFFEL & ESSER CO.

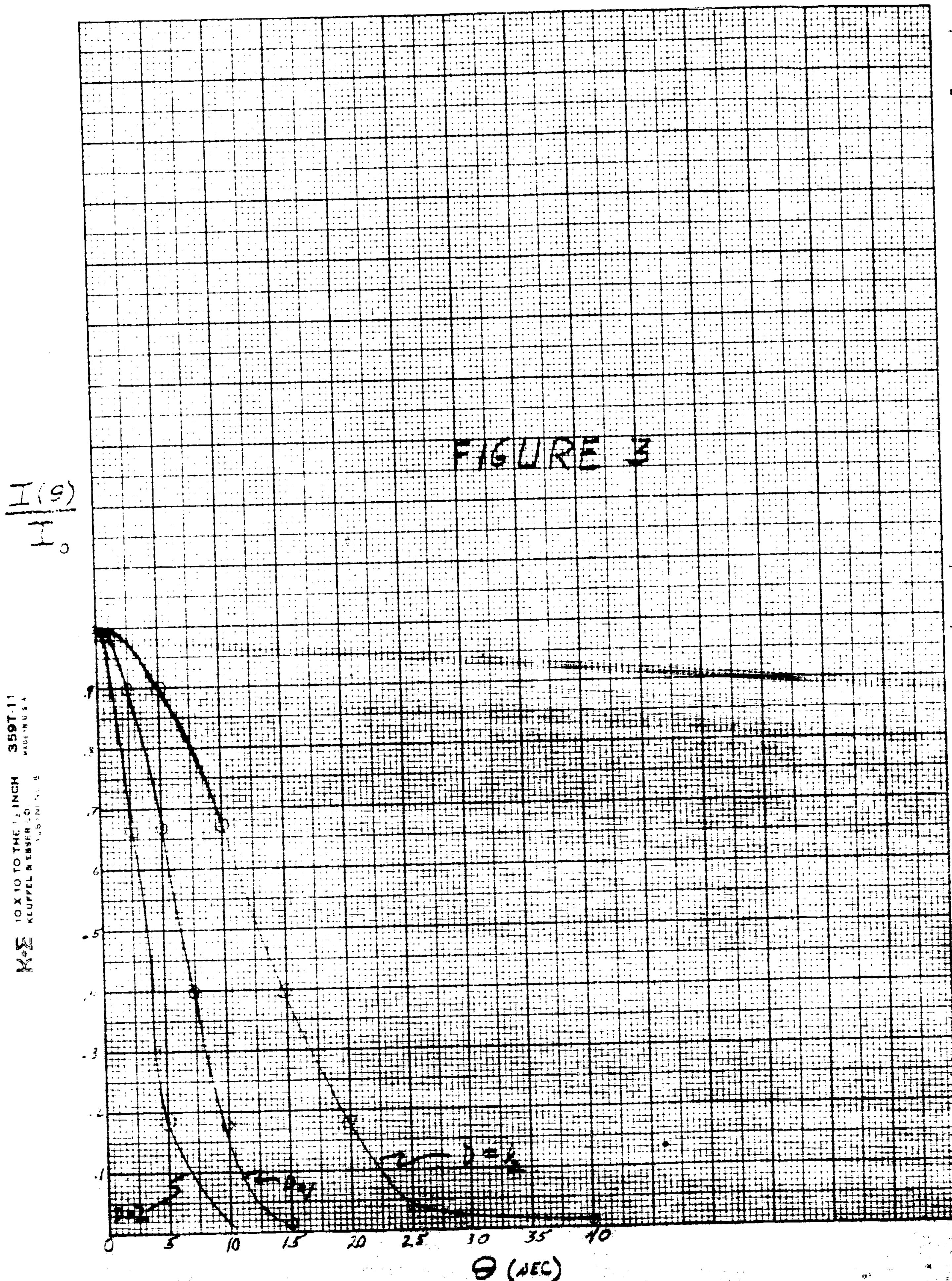
FIGURE 3
I(9) / I₀
θ (μsec)
0
5
10
15
20
25
30
35
40
.1
.2
.3
.4
.5
.6
.7
.8
.9
10 X 10 TO THE 1/2 INCH 359T-11
KEUFFEL & ESSER CO.

The dependence of θ_{PHA} , $\theta_{\frac{1}{2}}$, and θ_o on diameter D is shown in Figure 2.

The intensity of a collimated beam at various angles is given by the dependence

$$\frac{I(\theta)}{I_o} = \left\{ \frac{2 J_1\left(\frac{\pi D}{\lambda}\theta\right)}{\frac{\pi D}{\lambda}\theta} \right\}^2$$

This dependence is plotted in Figure 3 for D = $\frac{1}{2}$, 1, and 2 cm, with λ = 6328 Å.

A coherent light beam brought to focus by a diffraction limited lens always exhibits an interference pattern.

The central portion or airy disc contains approximately 84% of the incident light.

Figure 4 represents a plot of the distribution of the power in the diffraction pattern expressed as the percentage of the power in a cone whose half angle is θ . The angular dimension is normalized to unity at the first Airy dark ring, i.e. at 1.22 λ/D. At this point the percentage power is 84%.

BEAM SPREAD

A quantity of prime importance in discussions concerning laser light uses and capabilities is the peak light intensity for a beam collimated by a uniformly illuminated circular aperture. Mathematically this quantity is expressed as the total laser power divided by π times the square of the beam spread angle.

i.e.,

$$\text{Peak Intensity} = \frac{\text{Power}}{\pi\,(\text{beam spread angle})^2}$$

Much confusion has resulted in the use of this quantity due to the various definitions of "beam spread angle." We will call this beam spread angle the "power half angle" to distinguish it from other measures of the beam spread, and denote it by θ_{PHA}. In Appendix B of Technical Memorandum # 76 it is shown that

$$\theta_{PHA} = \frac{2}{\pi}\left(\frac{\lambda}{D}\right) = .636\ \frac{\lambda}{D}$$

where D is the diameter of the collimating aperture.

Two other quantities which are often used to describe the beam spread angle are the half angle of the Airy dark ring's angular diameter, i.e., the peak to zero power angle denoted by θ_0, and the half-power half angle, i.e. the angle between peak and half peak intensity denoted by $\theta_{1/2}$. Figure 1 illustrates the physical significance of these two angles. It is easy to show that

$$\theta_{1/2} \simeq .51\ \frac{\lambda}{D}$$

$$\theta_0 = 1.22\ \frac{\lambda}{D}$$

FIGURE I